An Experimental and Numerical Study of Friction Stir Processing using Novel Tool Designs and its Application to Damage Repair

by

Sibasish Mukherjee

A dissertation submitted in partial fulfillment
of the requirements for the degree of
Doctor of Philosophy
(Materials Science and Engineering)
in The University of Michigan
2010

Doctoral Committee:

Professor Amit K. Ghosh, Co-Chair
Professor William F. Hosford, Co-Chair
Professor Jyotirmoy Mazumder
Professor Jwo Pan

The greatest resource that humankind has is to be found within human life itself. This treasure can be endlessly mined and developed. To believe in and encourage youth, bringing out their wisdom and strength, this is the challenge and purpose of education.

- Daisaku Ikeda

2010

To all my teachers and mentors

Acknowledgements

I would like to express my deep sense of gratitude to my thesis supervisor Prof. Amit Ghosh for his constant guidance during this research work. I am also indebted to Prof. William Hosford, Prof. Jyotirmoy Mazumder and Prof. Jwo Pan for their detailed and insightful critique of my thesis.

I would also like to thank Dr. Guru Dinda and Dr. Ashish Dasgupta for the numerous technical discussions I had with them. Their comments and suggestions have deepened my understanding. I would also like to thank Dr. Sudip Bhattacharya for his assistance in TEM work.

I also sincerely thank my sponsors Focus:Hope, ONR, Boeing and NSF for their financial assistance during my Ph.D. Thanks are also due to Mr. Robert Hewitt of Positive Tool & Engineering for the numerous fabrication jobs that he did for me. I am thankful to Mr. Steve Erskine for teaching me the use of a milling machine. My colleagues Bilal Mansoor, Rick Li, Xiang Li, Jared Tracy and William Lai have been extremely helpful and their help is duly acknowledged.

I owe an enormous debt of gratitude to my family members, to the members of the Soka family and especially to my wife Mrs. Radhika Shenoy. Their constant encouragement has guided me through very difficult times.

Last but not the least, the staff of the department of Materials Science and Engineering especially Mr. Justin Scanlon and Mrs. Renee Hilgendorf have been extremely helpful.

Sibasish Mukherjee

Table of Contents

List of Figures

Figure

List of Tables

Table

Abstract

Friction Stir Welding (FSW) is a solid-state joining technique developed by The Welding Institute, UK. The tool employed in FSW consists of a spinning pin with a stepped shoulder. The pin is inserted into the seam line between two sheets or plates to be welded. As the pin rotates and traverses along the joint line, it heats the surrounding material, plasticizes it severely, and stirs it, thus creating a weld. Friction Stir Processing (FSP), which is a derivative of FSW, uses the stirring action of the pin to produce fine-grained material.

Traditional estimates of the strain-rate during FSP have relied on the relationship between the measured grain-size and Zener-Hollomon parameter of the process. In this thesis some novel experiments were employed wherein a soft and ductile aluminum foil was embedded within a work-piece undergoing FSP to observe the deformation zone. The logarithmic thickness strain was experimentally measured by observing the change in thickness of the foil. Additionally the strain-rate was numerically evaluated from the FSP process parameters and the deformed foil geometry using finite-element analysis. In the same vein research was carried out to enhance shear-rate in FSP by devising a novel joining technique using multiple pins. Using a patented concept (U.S. Patent No.

7597237) a multi-pin Friction Driven Stitch Welding (FDSW) apparatus was designed and tested. In addition the joining efficacy of the FDSW apparatus was numerically estimated via finite element analysis.

FSW has traditionally been employed in joining low melting-temperature metals e.g. aluminum and magnesium. However the process also holds promise in joining high melting-temperature metals, e.g. steel, titanium etc. It can also be employed in applications other than joining or welding. One of the main objectives of this thesis is to employ FSP to repair and restore marine components which suffer degradation due to corrosion. Traditionally the repair and restoration of these components is performed by laser-assisted Direct Metal Deposition (DMD). However DMD process is often limited by porosity and residual stress which can adversely affect mechanical integrity and corrosion resistance of repair. The focus of the later half of this thesis is to explore the role of FSP as a stand-alone or a post-DMD repair technique. Towards that end FSP of copper-nickel 70-30 and 4340 steel is explored. Emphasis is given on understanding the effect of FSP on grain-structure, porosity, second-phase particles etc. These in turn affect mechanical integrity and corrosion resistance of repair. Repair was attempted on a marine component consisting of a thin cylindrical shell. This particular part which is made out of 7475 aluminum doesn't lend itself to deposition by DMD. Direct plug-based repair of this part by FSP was attempted. The challenges encountered and the means of circumventing them are described in this thesis.

Chapter 1

General Introduction

1.1 Friction Stir Welding and Processing

Friction Stir Welding (FSW) is a solid state joining technique developed by The Welding Institute, UK in 1991 [1]. The concept behind FSW is remarkably simple. A spinning non-consumable tool consisting of a stepped shoulder and a profiled pin is inserted into the seam line between two sheets or plates to be welded (Fig. 1.1). As the pin rotates and traverses along the joint line, it heats the surrounding material, plasticizes it severely, and stirs it, thus creating a weld [2]. Fig. 1.1 illustrates some common terminologies and definitions associated with FSW. The side of the welding tool, where the motion of the surface of the welding tool is in the same direction as the feed direction, is referred to as the advancing side. The opposite side, where the motion of the surface of the welding tool opposes the feed direction, is referred to as the retreating side. The difference in tool motion between advancing and retreating sides can lead to asymmetry in heat transfer, material flow and the properties of the two sides of the weld.

The solid-state nature of FSW leads to several advantages over conventional fusion welding methods since problems such as loss of alloying elements, porosity, solidification cracking and liquation cracking are avoided [3]. A fine recrystallized microstructure in the weld zone leads to sound mechanical property of joint. Absence of

consumables and shielding gas make FSW environmentally friendly. However the large force requirement in FSW necessitates heavy-duty clamping fixtures and powerful numerically-controlled machines. The exit hole left behind as the tool is withdrawn from the work-piece is also a drawback. Despite these limitations, FSW is considered to be the most significant development in metal joining in decades [4]. Friction Stir Processing (FSP) is a processing technique derived from FSW [5]. In FSP the stirring action of the pin is used to modify microstructure and alter composition in the work-piece. FSP is characterized by extensive plastic flow of material [6], refined grains with random misorientation of grain boundaries in the stirred region [7, 8] and mechanical mixing of surface and subsurface layers [9]. FSP can also be used to eliminate porosity and locally introduce wrought microstructure in cast components [10].

1.2 Microstructure

The contribution of intense plastic deformation and high-temperature exposure within the stirred zone during FSW/FSP results in recrystallization and development of texture [11-13], precipitate dissolution and coarsening within and around the stirred zone [14-15]. Based on microstructural characterization of grains and precipitates, four distinct zones have been identified as shown in Fig. 1.2 [16].

- *Base Metal (BM)*: This is the metal far away from the weld such that it experiences no mechanical deformation and although it may experience heat from the weld, is unaffected by it in terms of microstructure and mechanical property.
- *Heat Affected Zone (HAZ)*: This is common to all welding processes. As indicated by the name, this region is subjected to thermal cycle that modifies its microstructure

and/or mechanical property [17]. However material in HAZ does not undergo plastic deformation.

- *Thermo-Mechanically Affected Zone (TMAZ)*: This is the region that undergoes both plastic deformation and thermal cycle from the weld. However recrystallization does not occur in this region due to insufficient deformation strain [18].
- *Nugget Zone* (also *Stir Zone*): This is the region that lies on the traverse path of the pin. Material in this zone undergoes recrystallization [19, 20] due to intense plastic deformation and frictional heating. Under certain conditions, an onion ring structure is observed in the nugget zone. It has been suggested that the spacing of the onion rings is equal to the tool advance per rotation [21]. The precise origin of these rings has not been firmly established, although variations in particle number density [22], grain size [23] and texture [23] have all been conjectured.

1.3 Material Flow, Strain and Strain-Rate

The material flow during friction stir welding is quite complex depending on the tool geometry, process parameters, and material to be welded. However numerous investigations have taken place on aluminum alloys using conventional threaded pin geometry. Siedel et al. [9] suggested that the friction stir welding process can be roughly described as an in situ extrusion process wherein the tool shoulder, the pin, the weld backing plate, and cold base metal outside the weld zone form an ‘‘extrusion chamber’’ which moves relative to the work-piece. They concluded that the extrusion around the pin combined with the stirring action at the top of the weld created within the pin diameter a secondary, vertical, circular motion around the longitudinal axis of the weld.

Material flow of this kind gives rise to very high strain and strain-rate within the nugget zone. However, the maximum strain and strain rate experienced during FSW/FSPP has remained quite unclear, despite various efforts. Recently reported values of strain rate during FSP range from 1/sec to 17/sec [24, 25] and that for friction stir spot welding range from 20/sec to 650/sec [26]. These values are largely based on determination of grain size and then relating this to the Zener-Hollomon parameter. However grain-growth within the nugget zone and uncertainties in measurement of temperature complicates the procedure. In this thesis a simple and reliable method of measuring strain and estimating strain-rate is presented by observing the deformation of a ductile foil undergoing FSP [27]. This method also illustrates the complex flow patterns within the nugget zone which is the subject of discussion in Chapter 2.

1.4 Tool Design

Tool design is one of the most critical aspects of FSP in that it influences heat generation, plastic flow, the power required, and the uniformity of the welded joint. This realization has led to a wide array of creative designs of FSP tool particularly by The Welding Institute, UK. Pin geometries of the shape of pyramid, triagonal prism and skew pin which consist of threads, scrolls and flutes have been reportedly used [28]. The guiding philosophy behind various tool designs is to enhance shear, reduce load on the tool and minimize tool wear.

In this thesis a fundamentally different approach towards FSP tool design and indeed a fundamentally different approach towards FSP itself are presented. Ghosh [29] conceived the idea of using closely spaced multiple pins rotating and processing the same material

simultaneously. The use of multiple pins in close proximity to each other has the effect of multiplying the shear strain-rate. The assembly of pins can also be translated around a joint simulating a stitching action thus creating a sound weld. The concept and numerically simulation of the multi-pin solid state welding process [2] will be described in Chapter 3. The equipment design and implementation of multi-pin solid state welding process will be the subject of Chapter 4.

1.5 FSP of High Melting Temperature Alloys

FSW has traditionally been employed in joining low melting-temperature metals e.g. aluminum and magnesium. However the process also holds promise in joining high melting-temperature metals, e.g. steel, titanium etc [3]. It can also be employed in applications other than joining or welding. One of the main objectives of this thesis is to employ FSP to repair and restore marine components which suffer degradation due to corrosion. Traditionally the repair and restoration of these components is performed by laser-assisted Direct Metal Deposition (DMD). However DMD process is limited by porosity [30] and residual stress [31] which can adversely affect mechanical integrity and corrosion resistance of repair [32]. The focus of the latter part of this thesis is to explore the role of FSP as a standalone or a post-DMD repair technique.

Chapter 5 deals with the repair of a 4340 steel part which experiences load and is exposed to seawater. The DMD repair performed on the part created hard martensite layer on a soft substrate. A combination of flame heating and FSP was used to soften the DMD deposit. FSP of 4340 steel poses considerable challenges in terms of selection of tool

material, tool design, minimization of tool wear etc. Microstructure of the FSP 4340 steel is discussed and is related to the mechanical property.

The subject of Chapter 6 is the repair of a part made of copper-nickel 70/30 using FSP. Copper-nickel alloys find widespread use in marine environment due to their excellent corrosion resistance [33]. The copper-nickel part repaired by DMD showed porosity which is a common occurrence is cast alloys. FSP was used to convert the cast microstructure into a wrought microstructure and minimize porosity. However the high solidus temperature (1170°C) and low thermal diffusivity (8.5×10^{-6} m^2/s) of copper-nickel 70/30 in comparison to 7475 aluminum (diffusivity 6.4×10^{-5} m^2/s) pose a unique challenge during FSP. These aspects along with the microstructure and mechanical property of FSP copper-nickel 70/30 will be discussed in detail in Chapter 6.

Chapter 7 describes the repair of a part made of 7475 aluminum. FSP of 7XXX series aluminum has been studied widely. However DMD deposition of 7475 aluminum leads to evaporative loss of low-melting magnesium and zinc from the deposit [34]. It also often creates solidification and liquation cracking in the DMD. Thus direct repair of the part was attempted via FSP without resorting to DMD. The difficulties encountered in the process were the thin-shell and curvature of the part as well as the exit hole that FSP leaves as the tool withdraws from the work-piece. Detailed discussions on the ways and means to circumvent these problems will be presented. The subject of Chapter 8 is the FSP repair of 4047 aluminum which is a common filler material in welds. Mechanical property and microstructure of FSP 4047 aluminum will be discussed. Overall summary of this research will be provided in Chapter 9.

1.6 References

[1] W.M Thomas, E.D. Nicholas, J.C. Needham, M.G. Murch, P.T. Smitha and C.J. Dawes, GB Patent No. 9125978.8, International Patent Application No. PCT/GB92/02203, (1991)

[2] S. Mukherjee and A.K. Ghosh, *J. Manuf. Sci. Eng.* 130 (2008) 041015-1

[3] R.S. Mishra and Z.Y. Ma, *Mat. Sci. Engg.* R 50 (2005) 1

[4] R.S. Mishra and M.W. Mahoney, *Friction Stir Welding and Processing*, ASM International, Materials Park, OH (2007) 2

[5] R.S. Mishra, M.W. Mahoney, S. X. McFadden, N. A. Mara and A. K. Mukherjee, *Scripta Mater.* 42 (2000) 163

[6] R. Nandan, T. DebRoy and H.K.D.H. Bhadeshia, *Progress in Materials Sci.* 53 (2008) 980

[7] Y.S. Sato, H. Kokawa, K. Ikeda, M. Enomoto, S. Jogan and T. Hashimoto, *Metall. Mater. Trans.* A 32 (2001) 941

[8] D.V. Field, T.W. Nelson, Y. Hovanski and K.V. Jata, *Metall. Mater. Trans.* 32A (2001) 2869

[9] T.U. Seidel and A.P. Reynolds, *Metall. Mater. Trans.* 32A (2001) 2879

[10] Z.Y. Ma, S.R. Sharma, R.S. Mishra and M.W. Manohey, *Mater. Sci. Forum 426–432* (2003) 2891

[11] S. Benavides, Y. Li, L.E. Murr, D. Brown and J.C. McClure, *Scripta Mater.* 41 (1999) 809

[12] Y. Li, L.E. Murr and J.C. McClure, *Mater. Sci. Eng.* A 271 (1999) 213

[13] Z.Y. Ma, R.S. Mishra and M.W. Mahoney, *Acta Mater.* 50 (2002) 4419

[14] M.W. Mahoney, C.G. Rhodes, J.G. Flintoff, R.A. Spurling and W.H. Bingel, *Metall. Mater. Trans.* A 29 (1998) 1955

[15] Y.J. Kwon, N. Saito and I. Shigematsu, *J. Mater. Sci. Lett.* 21 (2002) 1473

[16] P. Threadgill, *TWI Bull.* 38 (1997) 30.

[17] K.V. Jata, K.K. Sankaran and J.J. Ruschau, *Metall. Mater. Trans.* 31A (2000) 2181.

[18] M.W. Mahoney, C.G. Rhodes, J.G. Flintoff, R.A. Spurling and W.H. Bingel, *Metall. Mater. Trans.* 29A (1998) 1955

[19] J. Hirsch and K. Lücke, *Acta Metall.* 36 (1988) 2863.

[20] R.D. Doherty, D.A. Hughes, F.J. Humphreys, J.J. Jonas, D.J. Jensen, M.E. Kassner, W.E. King, T.R. McNelley, H.J. McQueen and A.D. Rollett, *Mater. Sci. Eng.* A 238 (1997) 219

[21] G.R. Cui, Z.Y. Mab and S.X. Lia, *Scripta Mater.* 58 (2008) 1082

[22] M. A. Sutton, B. Yang, A. P. Reynolds and J. Yan, *Mater. Sci. Eng.* A364 (2004) 66

[23] S. H. C. Park, Y. S. Sato and H. Kokawa, *Metall. Mater. Trans.* A 34A (2003) 987

[24] C. I. Chang, C.J. Lee and J.C. Huang, *Scripta Mater.* 51 (2004) 509

[25] Ø. Frigaard, Ø. Grong and O.T. Midling, *Metall. Mater. Trans.* 32A (2001) 1189

[26] A. Gerlich, G.A. Cingara and T.H. North, *Metall. Mater. Trans.* 37A (2006) 2773

[27] S. Mukherjee and A.K. Ghosh, *Mater. Sci. Eng.* A 527 (2010) 5130

[28] W.M. Thomas, K.I. Johnson and C.S. Wiesner, *Adv. Eng. Mater.* 5(7) (2003) 485

[29] A.K. Ghosh, US Patent No. 7597237, (2009)

[30] J. Choi and Y. Chang, *Int. J. Machine Tools Manuf.* 45 (2005) 597

[31] A.H. Nickel, D.M. Barnett and F.B. Prinz, *Mater. Sci. Eng.* A317 (2001) 59

[32] K. P. Cooper, P. L. Slebodnick, K. E. Lucas and E. A. Hogan, *J. Mater. Sci.* 33 (1998) 3805

[33] *ASM Handbook*, The American Society of Metals, Metals Park, OH, 13(B), (1995) 125

[34] M.J. Cieslak and P. W. Fuerschbach, *Metall. Trans.* 19B, (1988) 319

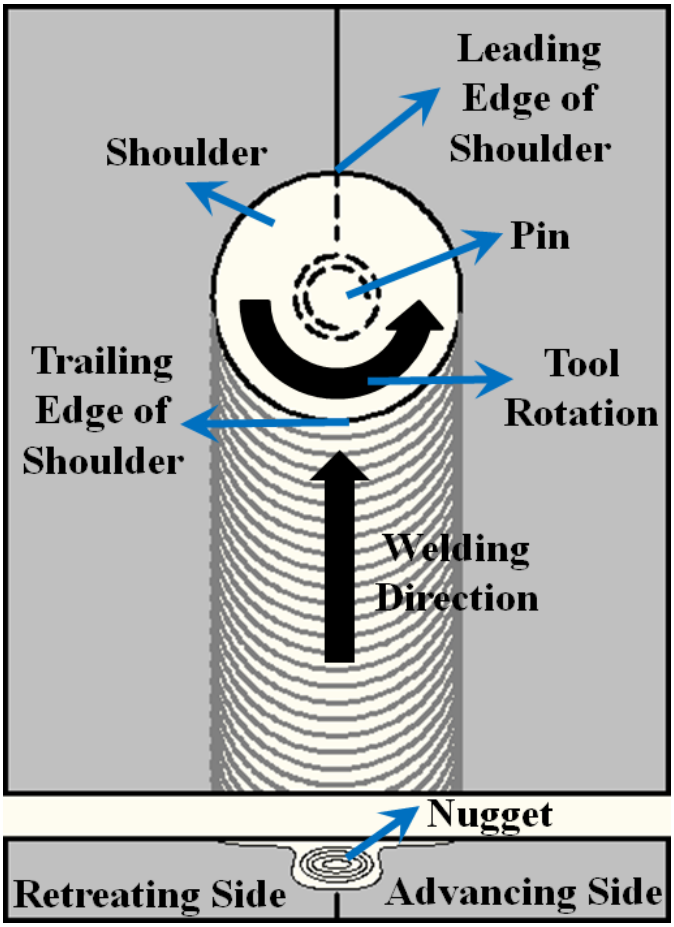

Fig. 1.1 Schematic drawing of Friction Stir Welding.

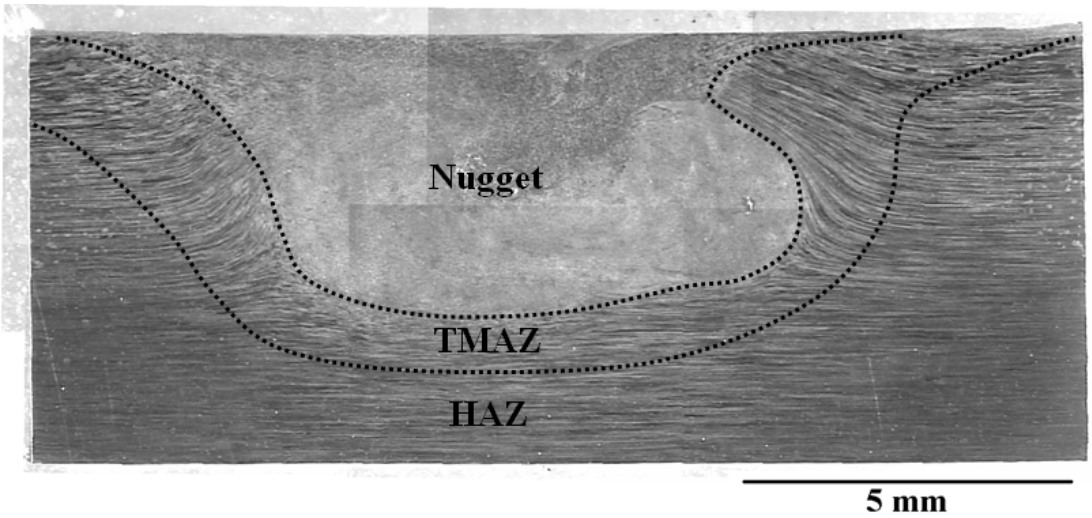

Fig. 1.2 A typical macro-image showing various microstructural zones in FSP 7475 Al.

Chapter 2

Flow Visualization and Estimation of Strain and Strain-Rate During Friction Stir Process

Abstract

A soft and ductile aluminum foil was embedded within a work-piece undergoing Friction Stir Processing (FSP) to observe the deformation zone. A whirlpool of material was detected in the stir zone which consumed the foil over time. The thickness strain was experimentally measured by observing the gradual change in thickness of ductile aluminum foil. Additionally a strain-rate was numerically evaluated from the FSP process parameters and the deformed foil geometry using finite element analysis. It is believed that this method provides reliable strain-rates in the friction stir process.

2.1 Introduction

Friction stir processing involves severe plastic deformation at high strain rate and an elevated temperature [1]. The material flow around the pin tool is complex and depends upon pin geometry, material properties and other process parameters such as the rate of rotation and feed, tool tilt, contact load. Several authors have performed experiments in

an attempt to understand material flow around the pin tool. Colligan [2] analyzed the flow of material around the pin tool by inserting small steel balls embedded in the work-piece and tracking their displaced position by radiography. He observed a chaotic movement of steel balls located close to the shoulder. He also observed an irregular deposition of steel balls in certain locations of the pin, which can be attributed to the finite size of steel balls and the turbulent nature of flow-field where there is a stochastic variation in momentum and energy transfer from the FSP tool to the steel balls. Siedel et al [3] observed material flow by press-fitting 2195 aluminum markers within a 5454 aluminum matrix in different locations along the tool path. The marker positions and dimensions were such that they allowed a piecewise reconstruction of material flow of the entire welded zone. Schmidt et al [4] used thin copper foil as a marker to observe metal deformation and measure material flow velocity in the weld zone. The copper foil fragmented as it entered the weld zone. Nevertheless by measuring the area occupied by the copper foil fragments in the shear layer in the immediate vicinity of the pin, Schmidt was able to estimate the average velocity of copper marker to be 10%-30% of the pin surface velocity. This high material velocity localized within a thin shear layer gives rise to high shear strain rate. There have been several attempts to estimate strain-rate during FSP. Gerlich et al [5,6] calculated the Zener-Hollomon parameter during friction-stir spot welding of several aluminum alloys using the subgrain diameter within the nugget. They used a threaded pin of 4mm diameter and employed a rotation rate between 1000rpm and 3000rpm. Using the measured temperature on the pin surface they further estimated the strain-rate which was between 20/sec and 650/sec for Al 7075-T6, between 180/sec and 497/sec for Al 5754-O and between 55/sec and 395/sec for Al 6061-T6. Frigaard et al [7]

estimated the strain-rate by using measured subgrain size, numerically calculated temperature values and an existing relation between subgrain size and Zener-Hollomon parameter. Using a rotation rate of 1500rpm and a feed rate between 5mm/sec – 12mm/sec they estimated a strain-rate between 1.7/sec-17.3/sec for Al 7108-T79 alloy.

The purpose of this investigation was to achieve some understanding of material flow around FSP pin tool and thereby gain an idea of strain rate. A thin and ductile aluminum foil was used as the marker material. Within the nugget zone the foil was indistinguishably mixed with the base material, but outside the nugget zone the foil aligned itself with local velocity field without getting fragmented. Thus the use of ductile foil permitted the visualization of complex material flow around the pin which might not be possible using a fragmented foil. Using the thickness of the continuous foil, the strain and strain-rate in the vicinity of the pin were estimated.

2.2 Experimental

The work-piece consisted of two 101.6mm×101.6mm×8mm 5083 aluminum plates and a 101.6mm×8mm×0.29mm 5457 aluminum foil which was sandwiched between them. The foil was prepared from a 5457 aluminum plate whose thickness was reduced by rolling in multiple steps. Finally a flat foil of approximately uniform thickness (~0.29mm) was produced by sandwiching it between two flat steel dies and keeping the assembly in a furnace at 400°C for 2 hours. The heat treatment made the foil much softer (29 Vickers) compared to the wrought plates (68 Vickers). The FSP passes were made in two different configurations – parallel and orthogonal – as shown in Fig. 2.1 and Fig. 2.5 respectively. In the parallel configuration the FSP pass was parallel to the foil plane whereas in the

orthogonal configuration the FSP pass was perpendicular to the foil plane. The work-pieces were securely held within a vise from the sides, constrained by a steel backup plate at the bottom and clamped from the top so that the work-pieces and the foil remained stationary during FSP. The FSP tool had a cylindrical flat shoulder and a conical pin with a spiral groove. The shoulder diameter was 22.2mm. The conical pin had a base diameter of 6mm and a tip diameter of 5mm. The pin height was 4mm from the surface of the shoulder. There was a concave recess at the base of the pin which allowed the material to flow upward during FSP. Also the tool rotation during FSP was clockwise such that the spiral groove on the pin transported material downward from the base to the tip. A tool rotation of 1500 rpm and a feed rate of 50.8 mm/min were employed in all experiments. The tool was tilted 2° towards the backside with respect to the plate surface normal during FSP.

A single FSP pass was run through the plates, parallel to the foil (parallel configuration, Fig. 2.1) and in close proximity to it. The distance from the mid-plane of the foil to the tool axis was 3.18mm – small enough that foil experienced the deformation field around the pin tool. After the FSP pass, the sample was sectioned perpendicular to the FSP pass. Similarly another FSP pass was run through the plates, perpendicular to the foil (perpendicular configuration, Fig. 2.5). Afterwards the sample was mounted parallel to the top surface and a layer of material 1mm thick was machined off from the top surface. The resulting microstructures are described in the following section. To achieve proper contrast between foil and plate, the sample was electro-etched with Barker's reagent (2% volume HBF_4 in water).

2.3 Results and Discussion

Fig. 2.2 shows the deformation of the foil in the parallel configuration. The tool traverse is towards the observer. Various zones within the work-piece, e.g., the stir zone, thermo-mechanically affected zone and heat affected zone are also outlined. The original distance between the axis of the tool and mid-plane of the foil was 3.18mm - which was small enough that the foil experienced the deformation field of the pin-tool. The foil retained its thickness at the bottom of the plate which was far away from the process zone but gradually thinned down as it came closer to the process zone. A possible reason of thinning is the heavy shear, but material removal of the foil in a whirlpool of rotating metal induced by the pin is also possible. The upper portion of the foil bifurcated into two branches. At the very top the foil was severely thinned and indistinguishably mixed with the base metal. Bifurcation of the foil indicated that complex metal flow occurred within the nugget zone and the soft and ductile foil aligned itself to the local velocity field. Fig. 2.3 shows a magnified image of the top portion of the foil and the complex flow patterns around it. The resulting shape of the foil after the tool had passed can be qualitatively explained in the following way (Fig. 2.4). The primary components of material motion in the weld zone are in-plane rotation and translation - which were imparted by the tool. A small component of the material velocity was imparted by the spiral groove on the pin surface which transported the material downwards while rotating in the clockwise fashion. This created a vertical current of material within the stir zone. Outside the stir-zone there was an upward motion of material towards the crown of the shoulder. The foil was thinned by heavy shear imparted by these two opposite currents of material. At the very top and close to the shoulder the temperature and velocity were high and there was a

whirlpool of rotating material in which the foil got absorbed and indistinguishably mixed. Additional thinning took place before the foil merged into the whirlpool. The deformation of the foil was also observed in the orthogonal configuration where the pin cut through the foil plane perpendicularly. Fig. 2.5 shows a schematic of the configuration.

The top portion of Fig. 2.6 shows the deformation of the foil which is outlined in the top cross sectional view. The pin path is outlined by broken lines. The positions of these lines are determined in the following fashion and also illustrated at the bottom of Fig. 2.6. The midpoints of the foil outside the shoulder region in advancing and retreating sides are joined using a straight line (AB). The straight line AB represents the midplane of the foil in the undeformed configuration. The straight line CD is obtained by joining the tips of the foil at the advancing and retreating sides. The center of the pin passes through the midpoint of CD. A perpendicular EF on AB is drawn passing through the midpoint of CD. EF is the traverse path of the center of the pin. EF is offset on both sides by the pin radius to obtain the outline of pin path. The width of the nugget zone between the foil tips at the advancing and retreating side is slightly more than the pin diameter. Also the foil tip at the retreating side is approximately tangent to the nugget zone. So the foil was consumed within the whirlpool of rotating material immediately outside the pin. In the retreating side the foil thins down gradually as it is sheared by the pin. In the advancing side, however, the foil thickens before it is thinned down. Similar thickness variation of the foil is observed at a depth of 2mm from the shoulder. One possible explanation of foil thickening is found by analyzing a typical velocity streamline pattern around the pin [8], where there is a “flow reversal” at the advancing side, i.e. a portion of the material flows

along with the pin whereas the adjacent material flows in the opposite direction. No flow reversal takes place at the retreating side.

The gradual thinning of the soft and ductile foil provides an opportunity to measure thickness strain of the foil. Fig. 2.7 shows a magnified image of the foil tip at the retreating side. Fig. 2.8 shows a plot of thickness of the foil in the retreating side as a function of distance from the centerline of the tool. The deformed thickness of the foil was determined by finding its mid-plane and drawing a normal on the mid-plane which intersects the outer surfaces. The length of the normal is defined as thickness of the foil at the intersection point between that normal and mid-plane. The minimum observable thickness of the foil is ≈ 3 μm before it indistinguishably mixes with the plate material. In this case the thickness strain is $\ln(D_0/D)$ where D_0 is the undeformed foil thickness and D is the deformed foil thickness. It is assumed that no material is removed from the foil and the thinning is solely due to shear. Fig. 2.9 shows a plot of thickness strain versus distance from the tool centerline for the retreating side. The maximum observable thickness strain at 1mm depth from the shoulder is ≈ 4.6.

2.4 Numerical Simulation

To gain more detailed understanding of the strain and strain-rate in work-piece during FSP a two-dimensional finite-element simulation was made using ABAQUS. The foil didn't constitute a part of the model and the entire work-piece was treated as a continuum of 5083 aluminum. This simplification was necessary because the goal was to study the strain and strain-rate imparted on the work-piece and not on the foil. However the deformed shape of the foil was incorporated in the simulation. It was shown that the

deformed shape of the foil can be obtained simply by tracking the displaced position of material points which originally lie along a straightline.

The pin was treated as a rigid circular wire body of diameter 5.4 mm. The rectangular work-piece was meshed with four-node quadrilateral elements. The smallest element was along pin-workpiece interface and its dimension is 0.27mm × 0.3mm. Severe plastic deformation and material flow were handled with adaptive meshing and arbitrary Lagrangian-Eulerian formulation. A material velocity, which was same in magnitude of the tool translational velocity but opposite in direction, was assigned at the inlet edge of the work-piece. In order to complete the simulation within reasonable time, mass scaling option was used by imposing a minimum element-by-element stable time increment. The work-piece material was 5083 aluminum which was assumed to follow a Johnson-Cook type plasticity model as per the following equation

$$\sigma = [A + B(\varepsilon)^n]\left[1 - \left(\frac{T}{T_m}\right)^m\right] \quad \ldots\ldots\ldots\ldots (2.1)$$

where A = 275MPa, B = 545MPa, n = 0.475, T_m = 933K, m = 1.7 [9].

Contact between the pin and the work-piece was modeled by prescribing a uniform tangential material velocity along the pin-workpiece interface. The imposed velocity ratio (δ) is defined as:

$$\delta = \frac{V_{MATRIX}}{\omega R} \quad \ldots\ldots\ldots\ldots (2.2)$$

where V_{MATRIX} is the tangential material velocity at the interface, ω is the pin rotation rate (157 rad/sec) and R is the pin radius. The value of δ was adjusted to obtain agreement between model and experiment. Temperature variation in the model was

considered explicitly via a prescribed temperature field at every node in the work-piece. The imposed temperature field was purely radial (Fig. 2.10) and was obtained from another numerical simulation with identical geometry and a fully sticking (δ =1) contact condition. It was recognized that the distribution of temperature is dependent upon velocity ratio (δ) which is an adjustable parameter. However, imposing the temperature field explicitly offers considerable simplification, e.g., it reduces a coupled non-linear thermo-mechanical problem into a non-linear problem involving purely mechanical variables.

2.5 Results and Discussion

At the beginning of simulation, a series of tracer particles were released at the inlet edge of the work-piece. Tracer particles follow material motion at every point. Originally these tracer particles lay along a line (Fig. 2.11), but after the pin passed through them, the tracer particles lay along a curve (Fig. 2.11) which closely resembled the shape of the deformed foil. Deng et al [10] has observed similar distribution of tracer particles. Since the material velocity distribution around the pin-workpiece interface dictates the deformed configuration of tracer particles, by varying the velocity ratio at the pin-workpiece interface, various deformed configurations of tracer particles were obtained and compared with the experimental shape of the foil. Such a comparison was carried out in Fig. 2.12 where three different velocity ratios were used, namely, 0.05, 0.1 and 0.5. The experimental shape of the foil at the retreating side was also superimposed. In plotting the deformed configuration of tracer particles, the particle at the far end of retreating side was plotted first and the remaining particles were plotted in the same order

in which they had appeared in the undeformed configuration. Plotting was terminated as soon as the curve joining the tracer particles entered the zone traveled by the pin, thereby obtaining the deformed shape of the foil. It was observed that a higher velocity ratio at the interface causes a larger displacement of the foil parallel to the weld direction. Based on the displacement of the foil material parallel to the weld direction, it was concluded that a velocity ratio (δ) = 0.1 best approximated the experimental shape of the foil. Closer examination of Fig. 2.12 revealed that the numerical simulation consistently overestimated the size of the deformation zone around the pin. This is because material failure option was not included in the model. Real materials will invariably fail under heavy shear at the pin-workpiece interface thus limiting the spread of deformation zone.

Fig. 2.13 shows a distribution of shear strain rate around a pin with a velocity ratio of 0.1. As expected, the magnitude of shear strain rate along the interface is very high, with the highest strain rate being ~ 87 sec^{-1}. The angular distribution of shear strain rate along pin-workpiece interface was plotted in Fig. 2.14. The angle was measured clockwise from point A which was at 9 o'clock position along pin surface. A sinusoidal variation in shear strain rate was observed with the maximum occurring at 47° counterclockwise from advancing side and the minimum occurring at 47° counterclockwise from retreating side. Also in general, strain rate at the advancing side was higher than retreating side because a larger velocity gradient existed at the advancing side compared to the retreating side. In the reference frame of the pin, at the retreating side, material velocity induced by the pin rotation and the bulk velocity induced by pin traverse were in the same direction. But at the advancing side material velocity induced by the pin rotation and the bulk velocity induced by pin traverse were in the opposite direction thus resulting in abrupt change in

velocity profile. Fig. 2.15 shows a comparison of numerically estimated equivalent plastic strain and experimentally determined thickness strain as a function of distance from pin center. In comparing the experimental and numerical data it was observed that the experimental strain was measured on 5457 aluminum foil whereas the simulated strain was estimated on 5083 aluminum work-piece. It was also noted that thickness strain is always expected to be smaller that equivalent plastic strain (PEEQ) which is defined as

$$PEEQ = \underline{\varepsilon}^{PL}\Big|_0 + \int_0^t \underline{\dot{\varepsilon}}^{PL} dt \quad \ldots\ldots\ldots\ldots (2.3)$$

Nevertheless numerically estimated PEEQ spread around a wider zone around the pin and also reached a very high value (~200) at the pin-workpiece interface because, as previously mentioned, no material failure option is included in the model. Real materials will fail long before PEEQ reaches such high values.

2.6 Summary

In this study the deformation field around the pin of an FSP tool was observed by inserting a ductile foil in between two plates. A whirlpool of rotating material around the FSP pin tool was observed. On close proximity to the whirlpool, the foil was consumed but immediately outside the whirlpool zone the ductile foil underwent extensive thinning. The thickness strain was experimentally measured by observing the change in thickness of the foil. The maximum thickness strain measured was ≈ 4.6. A numerical simulation was carried out under the assumption of a uniform tangential material velocity along the contact interface between the pin and work-piece. Various values of velocity ratio –

which is the ratio of material velocity at the interface and pin surface velocity – were assigned to numerically study the deformed foil geometry. A velocity ratio of 0.1 best characterized the experimentally obtained deformed foil geometry. Under this contact condition, the maximum shear strain rate observed was ~ 87 sec^{-1}. However a sinusoidal variation of shear strain rate was observed along the pin-workpiece interface with the maximum occurring close to the advancing side and the minimum occurring close to the retreating side.

2.7 References

[1] R.S. Mishra and Z.Y. Ma, *Mat. Sci. Engg.* R 50 (2005) 1.

[2] K. Colligan, *Weld J.* 78 (1999) 229.

[3] T.U. Seidel and A.P. Reynolds, *Metall. Mater. Trans.* 32A (2001) 2879.

[4] H.N.B. Schmidt, T.L. Dickerson and J.H. Hattel, *Acta Mater.* 54 (2006) 1199.

[5] A. Gerlich, G. Avramovic-Cingara and T.H. North, *Metall. Mater. Trans.* 37A (2006) 2773.

[6] A. Gerlich, M. Yamamoto and T.H. North, *Metall. Mater. Trans.* 38A (2007) 1291.

[7] Ø. Frigaard, Ø. Grong and O.T. Midling, *Metall. Mater. Trans.* 32A (2001) 1189.

[8] R. Nandan, G.G. Roy, T.J. Lienert and T. DebRoy, *Sci. Tech. Weld. Joining* 11(5) (2006) 526.

[9] G.T. Gray, S.R. Chen, W. Wright, M.F. Lopez, LA-12669-MS, *http://library.lanl.gov/cgi-bin/getfile?00208837.pdf* (1994)

[10] X. Deng, S. Shu, *J. Manuf. Proc.* 6(2) (2004) 125

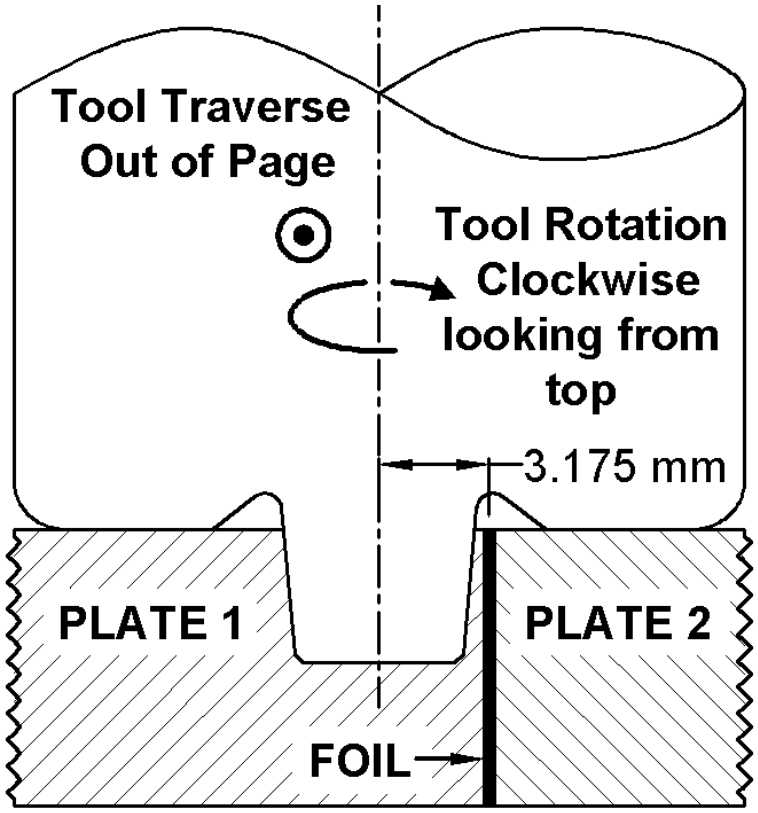

Fig. 2.1 Parallel configuration where FSP pass is parallel to the foil plane.

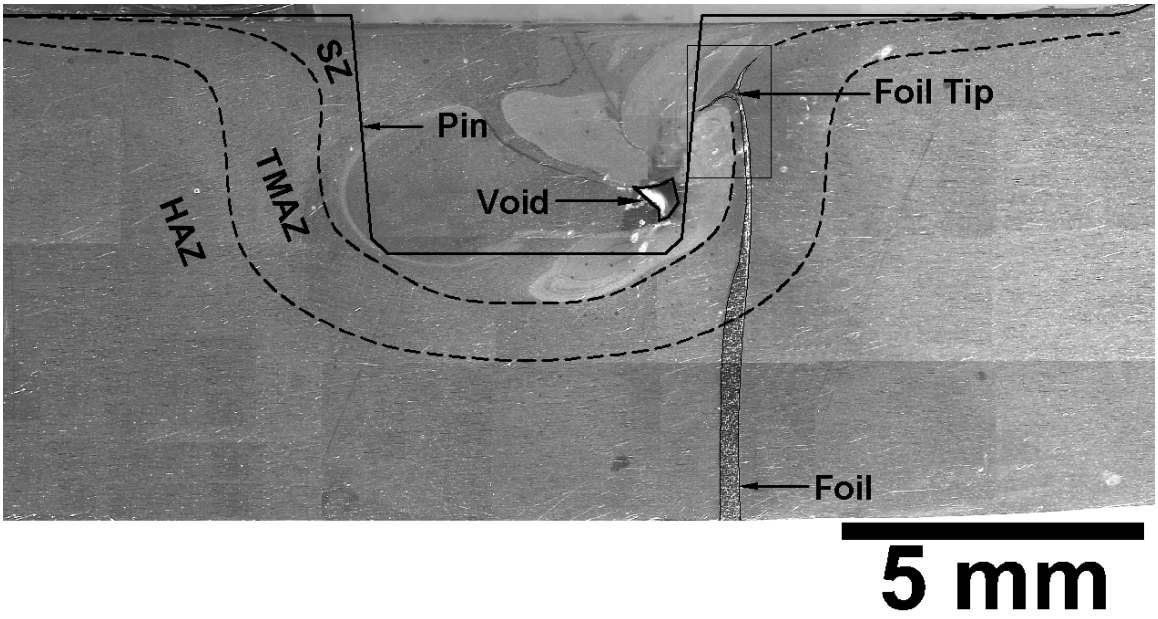

Fig. 2.2 Deformation of the foil in parallel configuration. The stir zone (SZ), thermo-mechanically affected zone (TMAZ) and heat affected zone (HAZ) are outlined. The boxed portion of the foil is magnified in Fig. 2.3.

Fig. 2.3 A magnified portion of the foil in Fig. 2.2 where it is bifurcated due to complex flow within the weld zone.

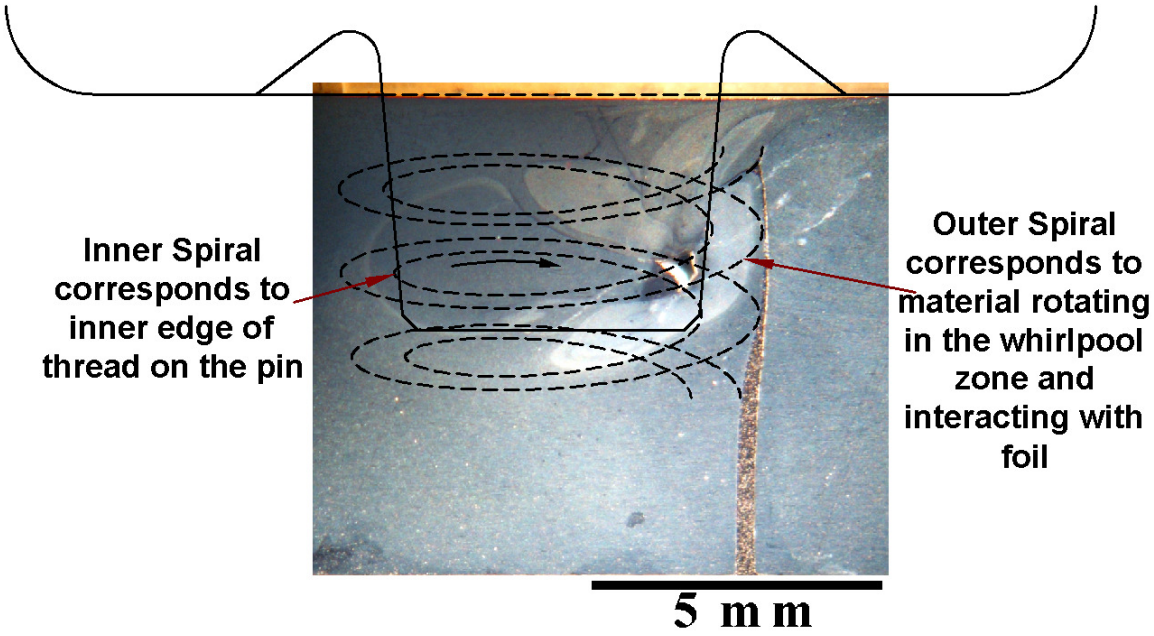

Fig. 2.4 Schematic illustration of the whirlpool of metal flow observed to cause bifurcation of embedded foil.

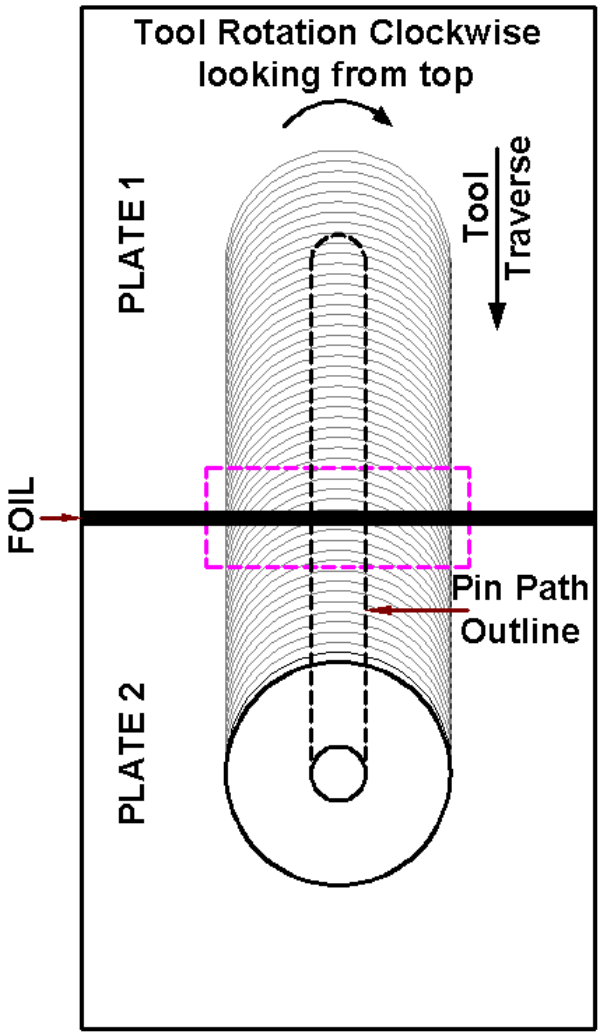

Fig. 2.5 Orthogonal configuration where FSP pass is perpendicular to foil plane. The boxed portion of the foil at the retreating side is magnified in Fig. 2.6.

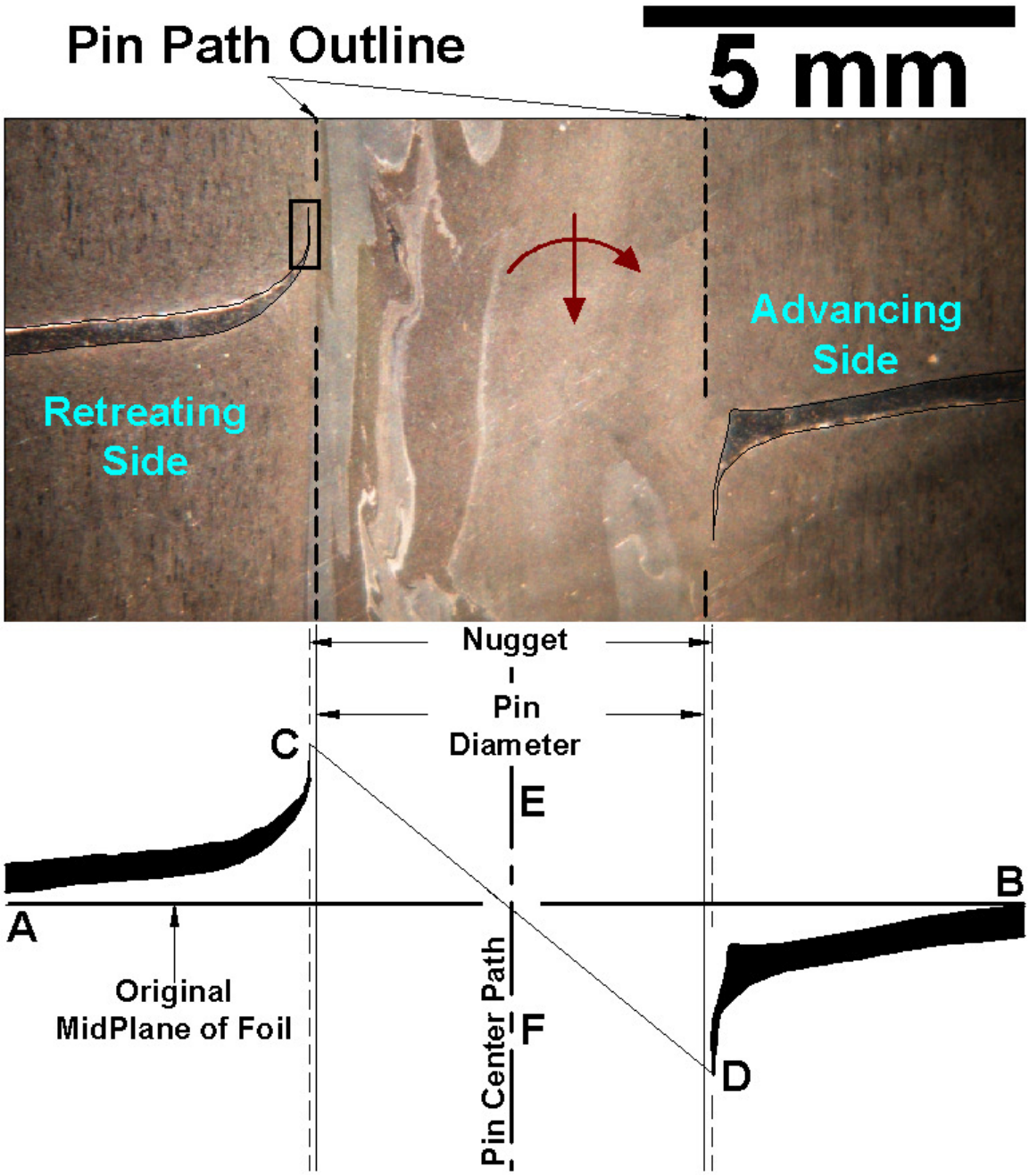

Fig. 2.6 The top portion shows the deformation of the foil in orthogonal configuration. The bottom portion illustrates the method of determining the pin path outline. Note that nugget zone is slightly bigger than pin diameter. The foil tip in the rectangular box at the retreating side is magnified in Fig. 2.7.

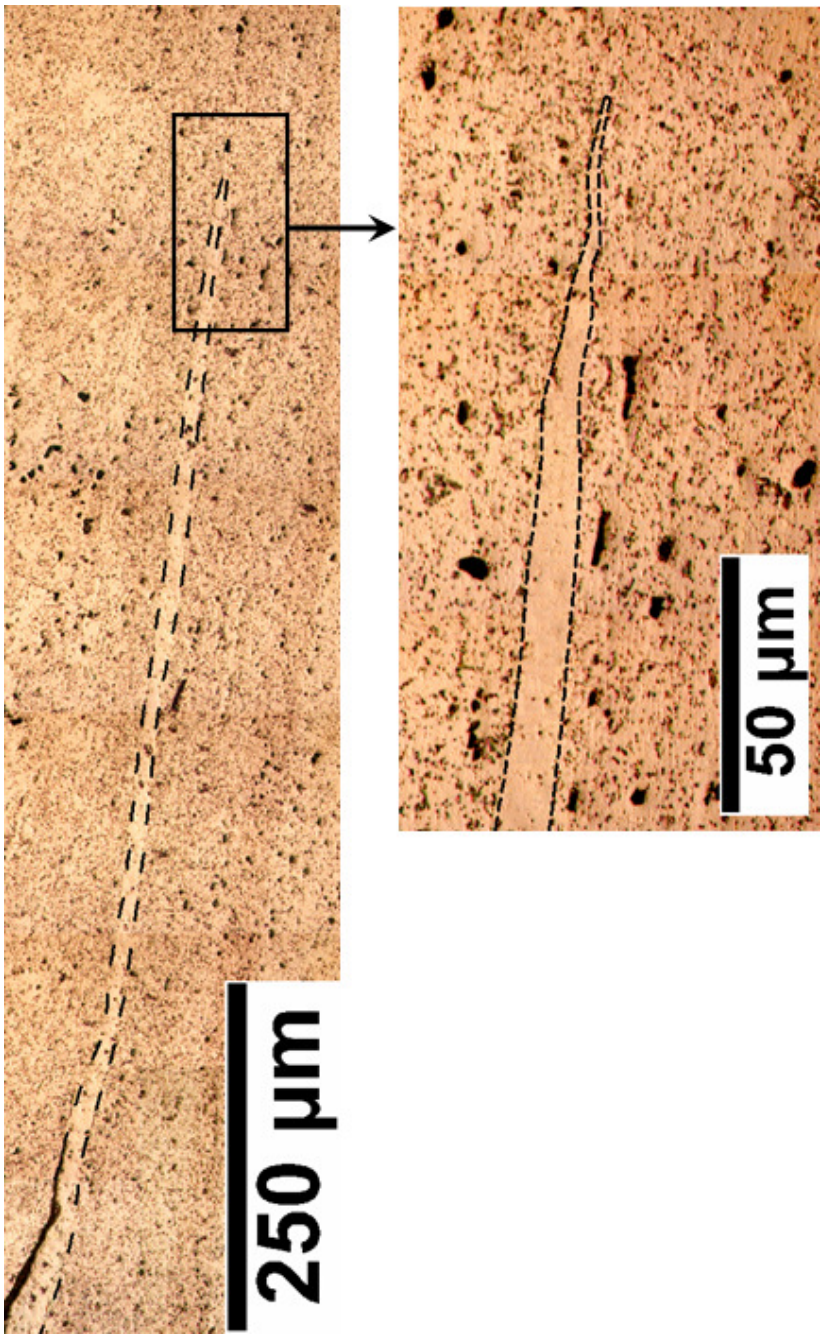

Fig. 2.7 The tip of the foil at the retreating side (Fig. 2.6) is magnified and outlined by broken lines.

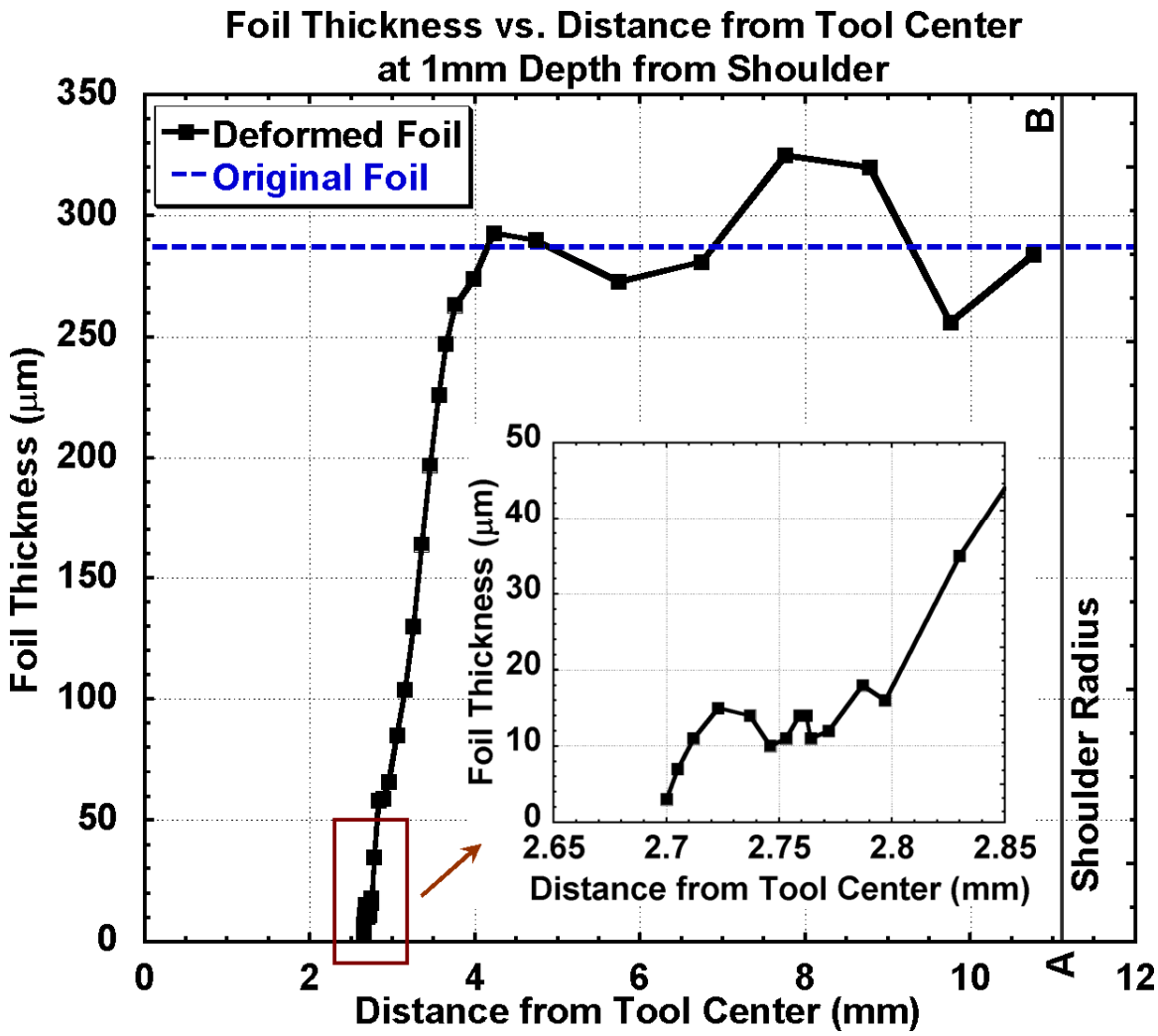

Fig. 2.8 Foil Thickness as a function of distance from the centerline of the tool. Shoulder radius is indicated by the vertical line AB.

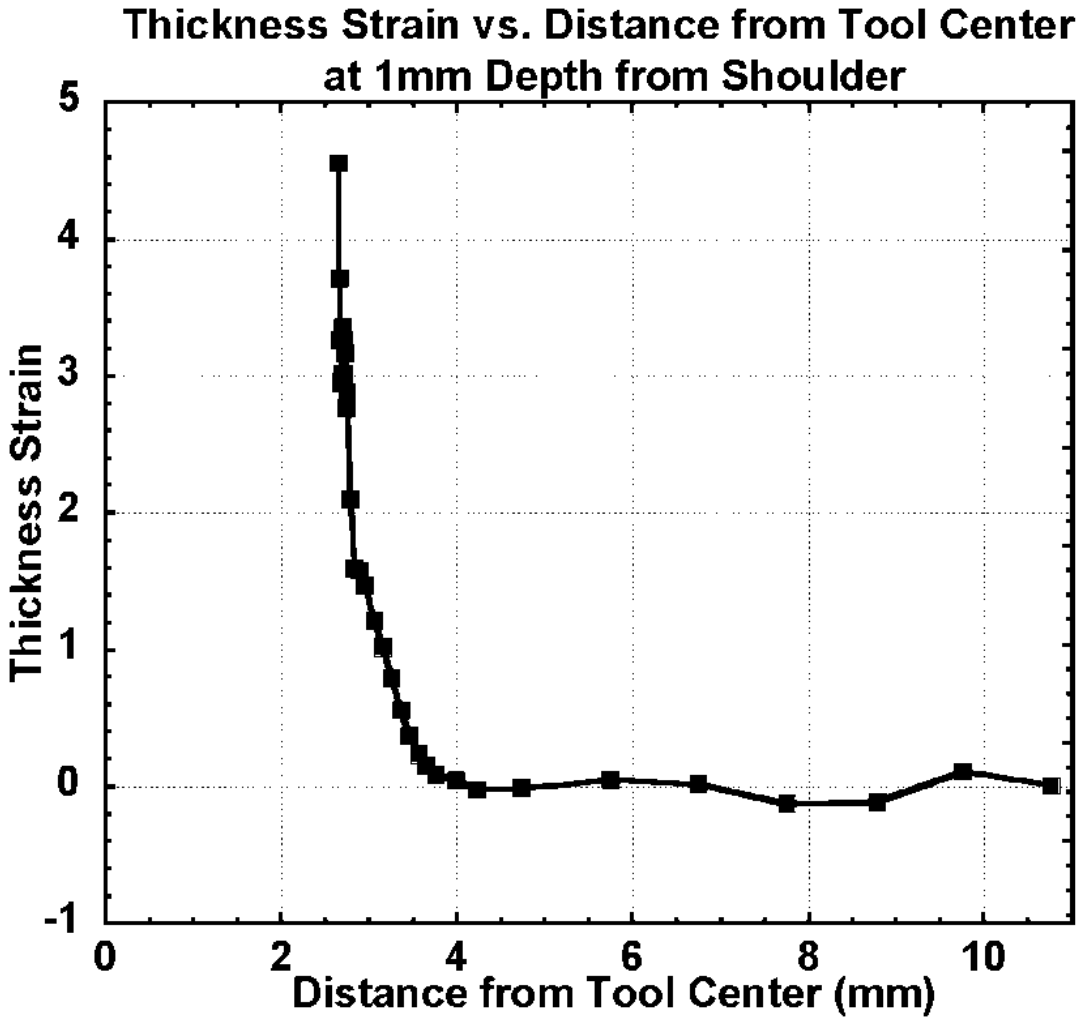

Fig. 2.9 Thickness strain at the retreating side as a function of distance from the centerline of the tool.

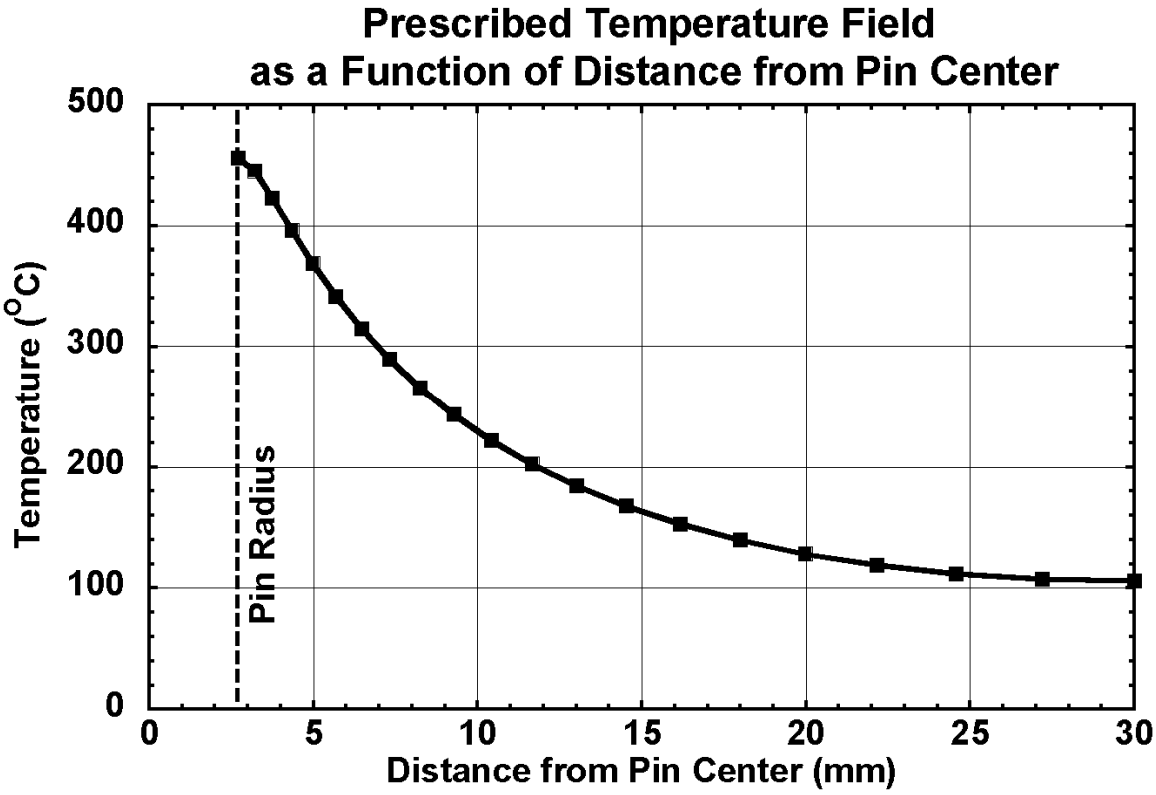

Fig. 2.10 Prescribed temperature field as a function of distance from the center of the pin. The temperature field is purely radial.

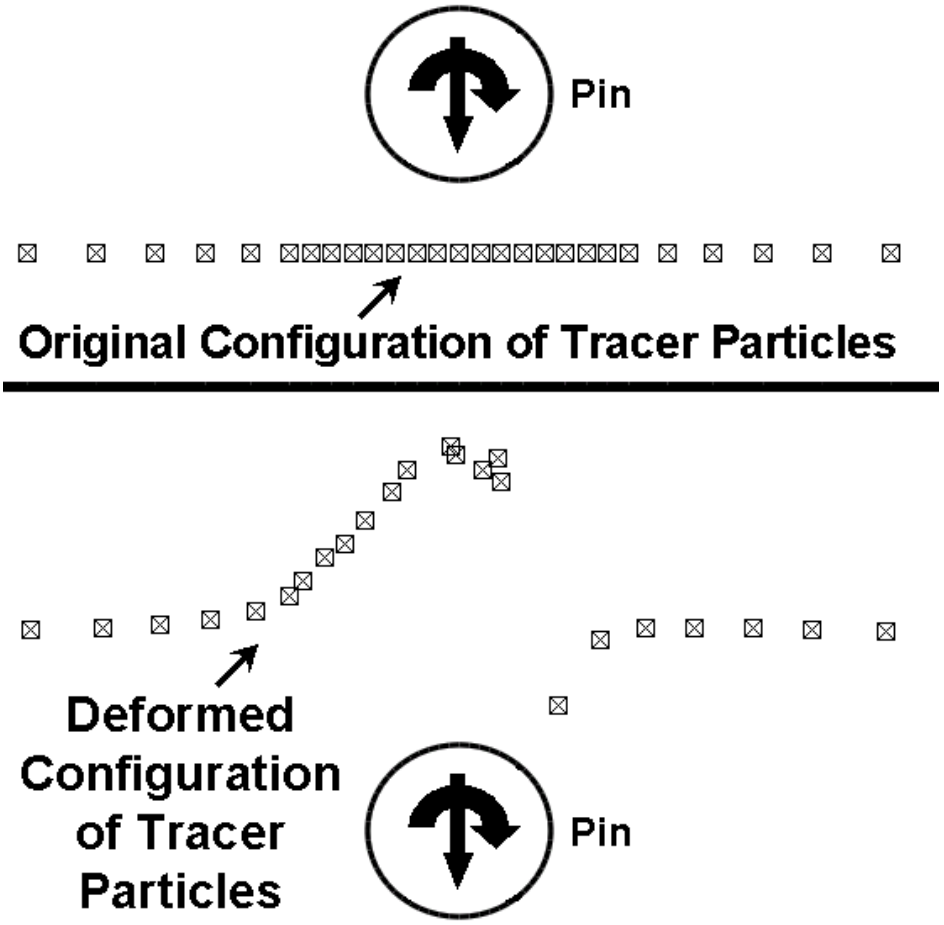

Fig. 2.11 Distribution of tracer particles which move along with the material. (Top) Original configuration of tracer particles is a straight line and is released upstream. (Bottom) Deformed configuration of tracer particles after the pin has passed through. The pin rotation and translation directions are indicated by arrows. The curve joining the tracer particles can be thought of as the midplane of the foil in Fig. 2.6.

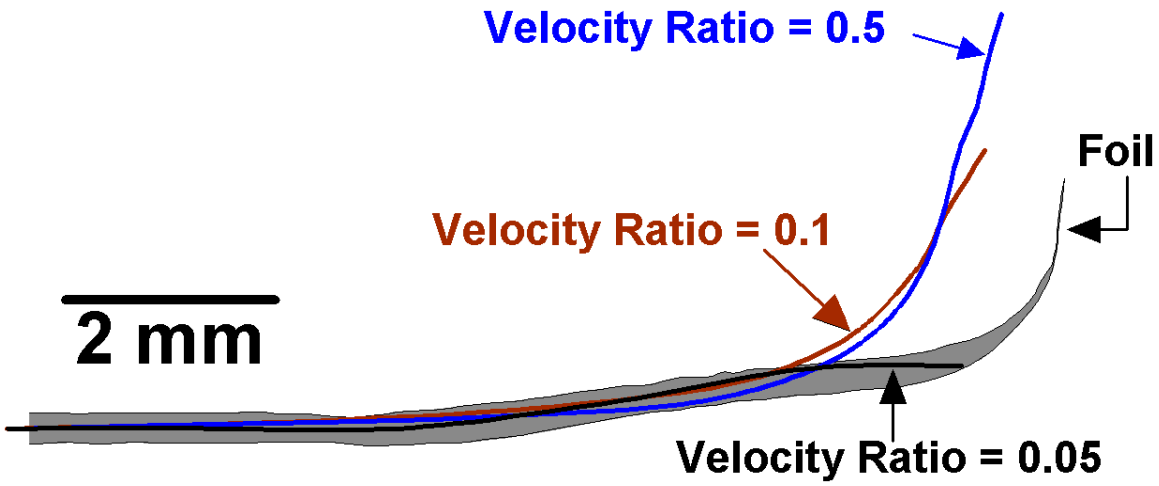

Fig. 2.12 Deformed configurations of tracer particles for three different velocity ratios are plotted. The experimental shape of the foil at the retreating side is also superimposed. A velocity ratio of 0.1 best approximates the experimental shape of the foil.

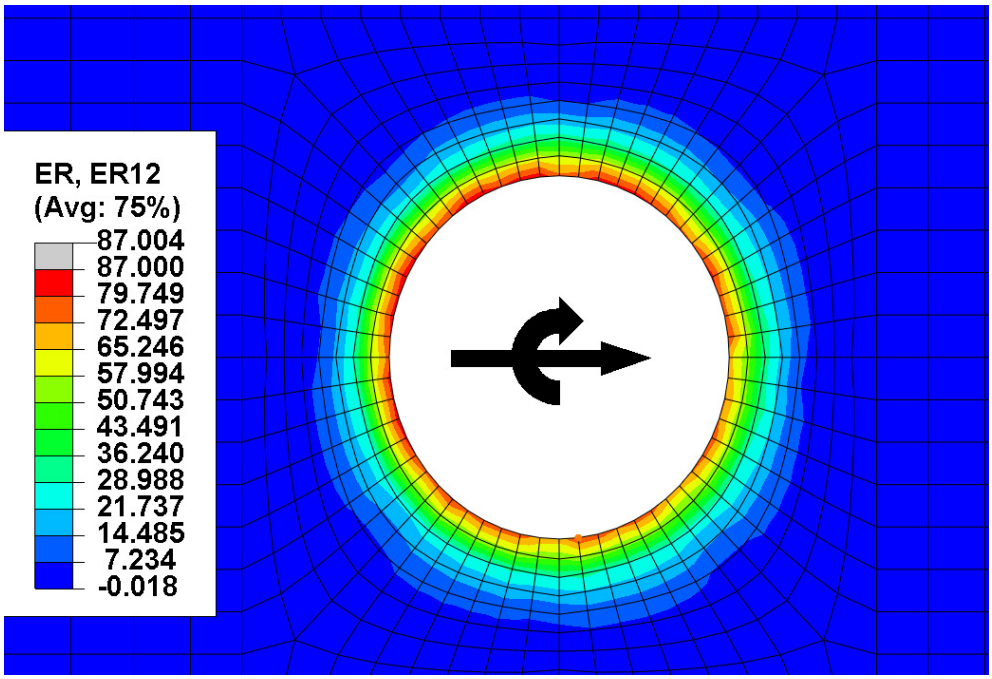

Fig. 2.13 Distribution of shear strain rate around the pin where velocity ratio = 0.1.

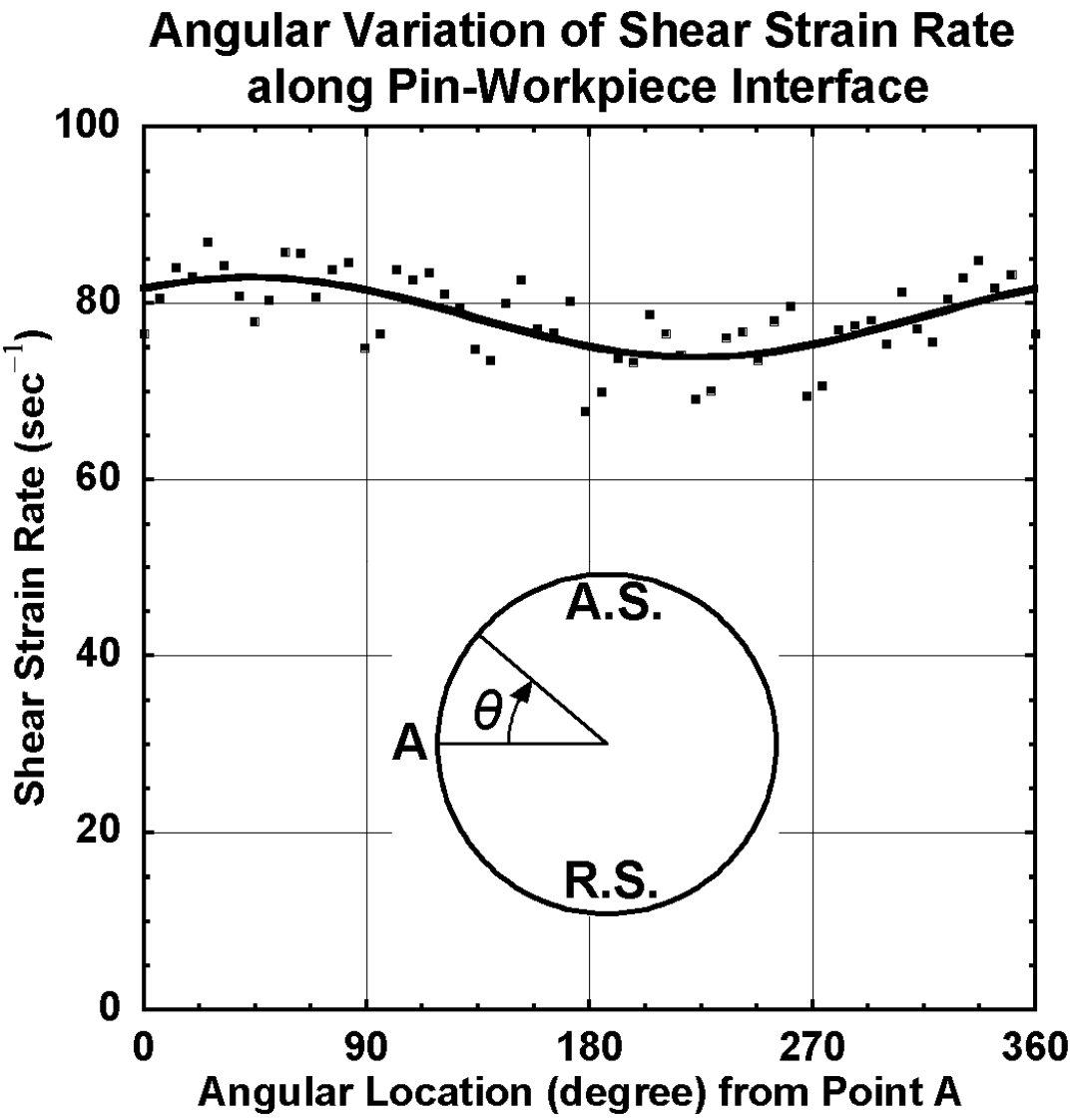

Fig. 2.14 Angular variation of shear strain rate along the pin-workpiece interface where velocity ratio = 0.1. Maximum strain rate occurs at 43° clockwise from point A. A.S. = Advancing Side, R.S. = Retreating Side.

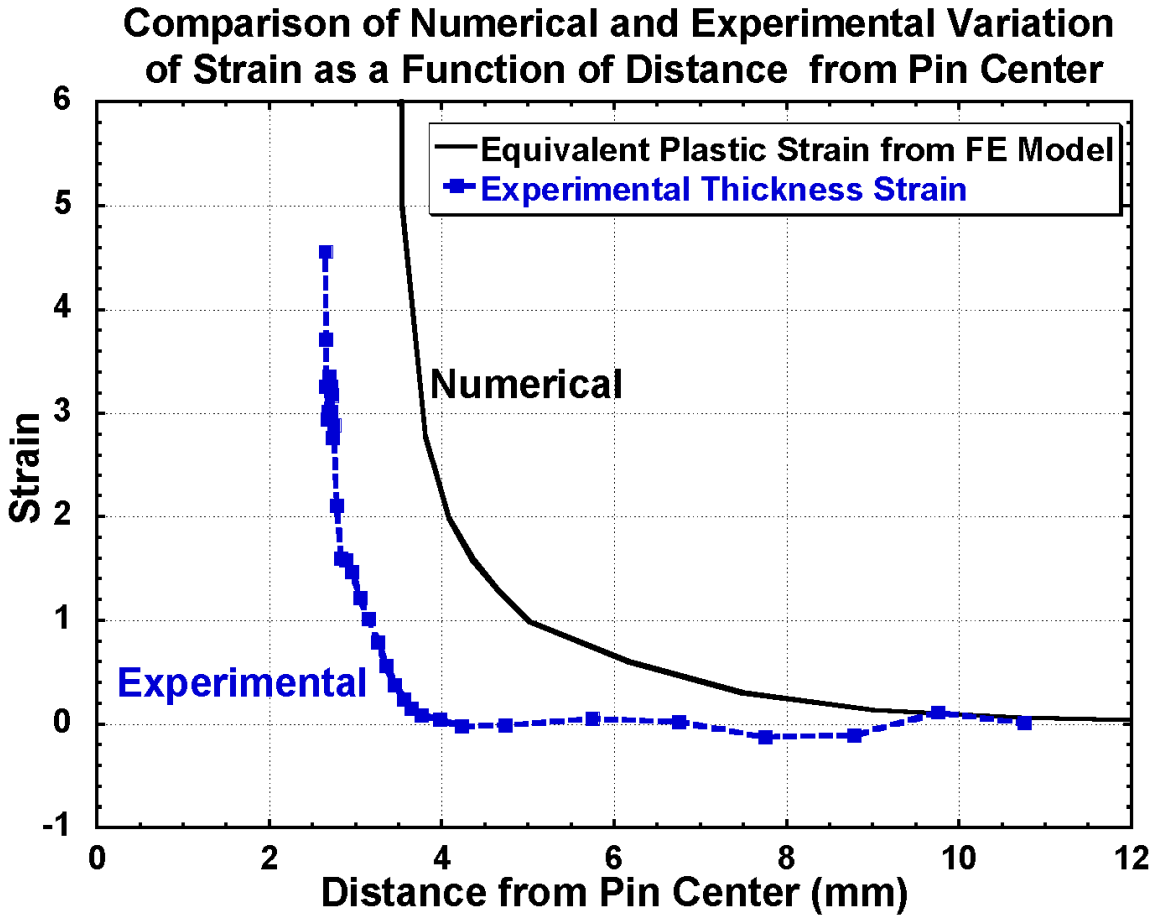

Fig. 2.15 Distribution of numerically estimated equivalent plastic strain and experimentally determined thickness strain as a function of distance from pin center. Equivalent plastic strain is numerically estimated for velocity ratio = 0.1.

Chapter 3

Simulation of a Solid State Joining Process Using Single-Shoulder Two-Pin Tool

Abstract

In friction stir welding (FSW), heat is generated by friction between the tool and the workpiece. The conventional tool design employs a cylindrical shoulder with a single profiled pin. A new process has been designed that uses two-pin tool under the same shoulder to increase shear deformation within workpiece that can enhance local heating where joining occurs. This design employs two closely spaced pins rotating in same direction within the workpiece under a separately controlled shoulder. The process is distinctly different from the Twin-stir™ variant of FSW in which each pin performs an independent function and non-interacting. Prior to gathering considerable experimental data with new equipment, a fully coupled themomechanical three-dimensional FE model was developed to compare the existing single-pin technology with new technology of friction driven stitch welding (FDSW) process. The computational results for the two-pin tool show considerable shearing along the joining interface, enhanced local heating and a reduced reaction force on the pins, that are described in this chapter. The results of this study indicate that the two-pin tool design with separate shoulder, with same direction of pin rotation

can be a superior design in comparison to the conventional single-pin FSW tool, and could minimize damage to tool material.

3.1 Introduction

In chapter 2 metal-flow around the FSW pin tool was described and strain and strain rate during FSW were estimated. In this chapter a new concept of two-pin design is analyzed which has the ability to further enhance the shear rate in material in comparison to conventional FSW. The motivation behind the two-pin design is the relative lack of success of conventional FSW in joining high melting-point metals e.g. titanium and steel. Although FSW has been applied quite successfully in joining low melting-point metallic materials, e.g. aluminum and magnesium [1, 2], considerable difficulty exists in welding high melting-point metals using FSW due to damages suffered by the tool [3, 4]. The goal of this work is to conduct an analysis of two-pin design that has the ability to localize and focus energy input into the material being joined, a process described as friction driven stitch welding in [5] and [6].

Briefly, the stitch-welding setup employs two closely spaced pins rotating in the same direction under a single shoulder, while the setup overall oscillates about the interface. The deformation fields around the pins interact with each other to produce intense shear at the interface. The device may be mistaken as the Twin-stir^{TM} variant of FSW as reported in [7], but it is unrelated to that process because it was motivated by an entirely different reason when certain limitations of existing FSW in terms of tool-material interaction was realized in 2002. Twin-stir^{TM} variants of FSW which evolved later employs two counter-rotating FSW tools with overlapping stir-zones such that the second

tool processes a previously processed area a second time, using two independent operations. Its goal was to improve the microstructure of the weld-nugget by performing the second step. But in that process the force field around one pin is not intended to be influenced by the force field of the second pin. In a stitch-welding scenario the two pins process the same material simultaneously, thus multiplying the local shear rate in the work-piece during the same operation so as to minimize the force field imparted to each pin during a single operation by efficient weakening of work-piece material. As described in [5], the general concept can involve more than two pins to accomplish the above objective. The fabricated apparatus of interest is shown in Fig. 3.1.

This chapter describes a finite element analysis of the friction driven stitch welding setup described above. Various authors have previously attempted to model the FSW process and the material flow therein based on solid mechanics. Askari *et al* [8] used a perfectly sticking contact model and validated the results by comparing the material flow with the flow patterns observed in welds with marker materials. Deng and Xu [9] used a two-dimensional finite element model to simulate the material flow in FSW. They constructed a thermal model by imposing a temperature field determined from an actual FSW test. However these models suffer from the difficulty of prescribing a stress or a displacement boundary condition at the tool-matrix interface. Schmidt and Hattel [10] have developed a fully coupled thermo-mechanical three-dimensional finite element model which assumes coulombic friction at the interface but does not assume a prevailing contact condition. Schmidt's model is particularly promising in that he was able to investigate the

conditions under which void formation at the interface occurred. In this chapter Schmidt's model is largely followed.

Bulk of the modeling effort described above has been devoted to understanding the steady state process in FSW. On the other hand the actual process of plasticizing has received less attention. Plasticizing should precede a successful FSW process and control the required parameters for successful weld; hence the following question is addressed "Starting from an undeformed sample how the material becomes plastically deformed"?

The objective of the current work is twofold. First in order to improve some of the limitations of the present single-pin FSW process, a new design of friction driven stitch welding apparatus is analyzed. It is established that by putting two closely-spaced pins rotating in the same direction, intense shear is generated at the interface, increasing the temperature and thus reducing the reaction force of the workpiece on the pins. Second, the actual process of plasticizing is modeled, starting from an undeformed sample.

3.2 A New Closely-Spaced Two-Pin Tool Design

The schematic of the design is shown in Fig. 3.2 for two-pin system. See [5] for more details. The features of the new design include:

- Closely spaced two-pin tool with an included tilt angle of 10°—12° between them. The pins rotate in the same direction causing intense shear along the joining interface
- Interchangeable pins in the pin-tool head to make the process economical.

- A separate rotating shoulder surrounding the two pins for heating the workpiece and constraining the deformed zone.
- A small oscillatory motion of the whole equipment about the interface that facilitates the material transfer across the joining line, thus simulating a stitching action.

The equipment was fabricated (Fig. 3.1) and tested. The results of the testing will be discussed in chapter 4.

3.3 Comparative Evaluation of the New Design Using Finite Element Analysis

A comparative FEA study among different pin-tool configurations was made. Two sets of comparisons were carried out, namely, (i) A two-dimensional mechanical model comparing three different geometries without considering the thermal effects (ii) A fully coupled thermo-mechanical three-dimensional model comparing the single-pin and two-pin configurations.

3.3.1 2D Comparative Study of Three Different Geometries

In this section the following three different geometric configurations were compared (i) Single Pin (ii) Two Pins rotating in the same direction and (iii) Two pins rotating in opposite direction. For all the above 2D configurations, thermal effects were ignored.

The workpiece in the 2D analysis had a circular geometry with a diameter of 40mm. Each pin, which was modeled as analytical rigid surface, was also circular with a diameter of 5mm. For the single pin case the pin lay at the center of the workpiece. For the two-pin case the pins lay in such a way that the line joining the center of the pins was inclined at

45˚ with respect to the horizontal weld line (Fig. 3.5). In this case the distance between the centers of the pins was 7mm. Note that the shoulder was omitted from this 2D model for the sake of simplicity.

A plain-strain Lagrangian analysis was carried out using a general purpose explicit code ABAQUS. The two-dimensional configurations were divided into four-node quadrilateral elements with 80 elements along each pin-workpiece interface and 112 elements along the periphery of the workpiece. The smallest element of the workpiece was closest to the pin and had the dimension 0.196mm × 0.125mm. A total of 5828 elements were used to model the workpiece.

Contact Model: A perfectly sticking condition was imposed at the interface between the pin and the work-piece, so the material at the interface rotated with the same speed as that of the pin. This condition is the simplest from the perspective of the actual process, but it was thought to be sufficient for the purpose of comparative evaluation among different configurations. The simulation was run in the natural time scale and without any mass scaling option.

Material Model: The material to be modeled was chosen as steel which was assumed to be isotropic. The elastic properties of the material are given in Table 3.1. In this 2D analysis a parabolic hardening law was used and the thermal properties were ignored. The hardening law was of the following form:

$$\sigma_Y = \sigma_0 + K\varepsilon_p^n \quad \text{……..(3.1)}$$

where σ_Y is the yield stress and ε_p is the plastic strain. K, σ_0 and n are material constants. The values of these constants are given in Table 3.2.

3.3.2 Results and Discussion of Section 3.3.1

One of the objectives of the current work was to gain an understanding of how the plasticizing process in FSW initiated in a strain-free workpiece. The simplest case of a single non-rotating pin translating through the work-piece was considered. Fig. 3.3 shows the calculated contour plot of plastic shear strain (ε_{XY}^{p}) for this case under the assumption of a perfectly sticking friction between the pin and workpiece. Fig. 3.4 shows the calculated contour plot of pressure ($=-tr(\boldsymbol{\sigma})/3$) for the same case. The pin traversed relative to the workpiece at a speed of 5mm/sec in the +ve X-direction for a period of 1 sec while the periphery of the work-piece was held stationary. High positive and negative shear-strain zones can be seen ahead of and behind the pin (Fig. 3.3) indicating the onset of shear instability. At the onset, the leftmost point of the pin (marked 'A' in Fig. 3.3) experienced a negative shear and the rightmost point (marked 'B' in Fig. 3.3) experienced positive shear. As the pin moved forward, these shear zones also moved forward along with the pin due perfectly sticking friction. But the elastically deformed matrix surrounding the pin resisted the deformation leading to a high positive pressure ahead of the pin and low pressure behind it (Fig. 3.4). Due to the pressure gradient between the front and the back of the pin the sheared layer of material flowed around the pin in the direction shown by the broken arrows (Fig. 3.3). Thus the shear failure in the matrix at the side of the pin is initiated by an extrusion process between the pin and the elastically deformed matrix. This process would be a precursor to any plasticizing process in FSW.

Next a comparative analysis of the single-pin and the two-pin configurations was made with an aim to see how the two-pin configuration with same direction of pin rotation

performed vis-à-vis a conventional single-pin and a hypothetical two-pin configuration with opposite direction of pin rotation under comparable conditions. Fig. 3.5 shows the calculated distribution of the von Mises stress for all three configurations after a certain time interval. Here each pin rotated with an angular speed of 3000 rad/sec and a traverse speed of 5 mm/sec. The rotation and translation directions are indicated by arrows. The periphery of the work-piece was held stationary. For the two pins rotating in the same direction, intense shear stress was observed along the joining interface where the elements were almost aligned with the weld line. For the two pins rotating in the opposite direction the von Mises stress in the center was low and the material in between the pins was undergoing extrusion. For the single pin case the angular distribution of von Mises stress was uniform and the peak value of von Mises stress was lower than that in the two-pin case with same direction of rotation. To gain a better understanding of the stress distributions, a path AB was drawn in each configuration as shown in Fig. 3.5. Path AB lay at an angle 45˚ with respect to the horizontal weld line and is also the line joining the center of the two pins. Along path AB the calculated von Mises stress for all three configurations is plotted, with the center of workpiece as the origin as shown in Fig. 3.6. Note that each curve is discontinuous in the region in which path AB intersects the pins. In a similar fashion the calculated equivalent plastic strain is plotted for all three cases along path AB as shown in Fig. 3.7. It is apparent from Fig. 3.6 and Fig. 3.7 that the spread of the deformation zone for the two-pin cases are greater than the single-pin case. Also except a region at the center of the workpiece, the von Mises stress and the plastic strain for two-pin cases are generally greater than the single-pin case. The region in between the pins is of particular interest. In this region the two pins rotating in the same

direction produce more strain than a single pin whereas the two pins rotating in opposite directions produce less (Fig. 3.7). This result is intuitive because the pins rotating in the same direction are able to shear the material intensely but the pins rotating in the same direction are only able to compress and extrude the material in between them.

One more parameter of interest is the force experienced by individual pin. This is important in view of the extensive pin wear observed during the friction stir processing of high-melting materials, namely, titanium, steel etc. In order to address that, the resultant of the forces imparted by the matrix on individual pins is calculated first. Then the magnitude of the resultant force is divided by the number of pins to calculate the average force per pin. Thus the average force is an indication of the overall resistance offered by the workpiece for each pin-configuration. In a similar fashion the average moment per pin for all three configurations is also calculated. The time evolution of the calculated average force and average moment for all three cases are compared in Fig. 3.8. Here a pin traverse speed of 5mm/sec and a rotation speed of 100rad/sec are used while the periphery of the workpiece is held stationary. Note that since the analysis is 2D plane strain, the force and moment are evaluated per unit thickness of the workpiece. It can be seen that initially the average force for both the two-pin configurations are less than the single-pin configuration. This is because when two rotating pins lie in the vicinity of one another, the forces they impart on the matrix are opposite in nature so that the reaction forces of the matrix are able to partially cancel each other. Also the average reaction force for the case of two pins rotating in the same direction is less than the case of two pins rotating in opposite direction. This can be qualitatively explained in the following way. The total mechanical work done by the pins on the workpiece can be expressed as:

$$W = \int M d\theta + \int F dx \text{ ..... (3.2)}$$

where M is the frictional moment on the pins and F is the resistive force. When two pins rotate in the same direction the frictional moment M becomes higher because the intense shear developed at the interface opposes rotation. This in turn reduces F, the resistive force offered by the matrix, provided that the total mechanical work (W) is same or sufficiently close. This is indeed the case as shown in the time evolution of average moment in Fig. 3.8. Note that the average moment for the two-pin case with opposite rotation is negligible compared to the other two cases. So the two-pin system with same direction of rotation reduces the matrix resistance by doing more rotational work.

The above analysis albeit simple illustrates that the two-pin system with same direction of rotation is a superior design in comparison to the two-pin system with opposite direction of rotation. Hence the later design is discarded in the subsequent work.

3.3.3 3D Thermomechanical Study of Single-pin and Two-pin Tools

In this section a fully coupled thermomechanical 3D model for the single-pin and two-pin geometries are developed. For the two-pin case only the counterclockwise rotation of the pins as well as the shoulder are considered. The case of two pins rotating in the opposite direction is not considered. The schematic of the two-pin system is shown in Fig. 3.2. The detailed dimensions of individual components are not presented for the sake of brevity. The commercial code used in this study is ABAQUS/Explicit which offers techniques like Arbitrary-Lagrangian-Eulerian formulation to handle large plastic deformation typically found in FSW/FSP.

WORKPIECE: The workpiece is modeled as a disc-shaped specimen of diameter 80mm and thickness 2mm. The interface in the workpiece is not taken into consideration in order for the material to flow seamlessly around the pin(s). In the single-pin case 16620 nodes and 14340 elements are used. In the two-pin case 32423 nodes and 27878 elements are used. In either case a 8-node solid element with trilinear displacement and temperature is used. Reduced integration with hourglass control is used to avoid mesh locking problems associated with large incompressible plastic deformation. The periphery of the workpiece is treated as an Eulerian surface where every node has a prescribed material velocity of $V_X = -2\,\text{mm/sec}, V_Y = V_Z = 0$. The rest of the surfaces are treated as sliding surface which follows the material in the normal direction but is unconstrained in the tangential direction. Since the material flows independent of the mesh, constraints are applied at every node. Before application of mesh-constraints each node is transformed with respect to appropriate coordinate system.

Application of proper mesh-constraints is crucial in modeling the FSW process because the workpiece is treated as an eulerian domain. The nodes of the inflow and outflow boundaries of the eulerian domain are fixed in space. The nodes of the bottom surface are constrained by a backup plate on which the workpiece rests. In other words the bottom surface nodes can't penetrate the backup plate. The nodes of the top surface, with the exception of the ones lying under the tool, are similarly constrained to lie in or beneath their undeformed location by putting an analytical rigid surface at the top.

The initial temperature of the workpiece as well as that of the surrounding is taken as 25˚C. As the tool stirs the material, the workpiece temperature rises due to frictional heat.

This leads to heat loss through the top and bottom surfaces of the workpiece. The heat transfer coefficient at the top surface is assumed to be $h_{\text{top}} = 10 W m^{-2} K^{-1}$ and that at the bottom surface is $h_{\text{bottom}} = 1000 W m^{-2} K^{-1}$. Since the area of the periphery is small compared to the area of top and bottom surfaces, the heat loss through the periphery is ignored.

BACKUP PLATE & TOOL: The backup plate and tool - which consists of pin and shoulder – are modeled as analytical rigid surface. With a view of simplifying the computation, all the rigid bodies are treated as isothermal and having no thermal degrees of freedom. The angular speed of the pins and the shoulder are prescribed as 200 rad/sec counterclockwise looking from the top. The pins are modeled as a frustum of a cone.

In the two-pin system each pin is tilted at an angle of 6˚ from the vertical. During the plunge period, the shoulder, pins and the fixed-part sink in a depth of 0.3mm before material starts flowing in the mesh.

The tool in the single-pin case is modeled as a combination of a separate pin and a shoulder – with the pin dimension being identical to that in the two-pin case. Moreover the pin is plunged to a depth of 0.3mm, the same plunge depth in the two-pin case, so that they displace equal volume of material. This allows the comparison of forces on the pins between the single-pin and two-pin tools.

CONTACT MODEL: A Coulombic friction with a coefficient of $\mu = 0.25$ is used to model the tangential contact between pin/shoulder and workpiece. The normal contact is

modeled by a "hard" pressure-overclosure relationship, in that it minimizes the penetration of slave nodes into master surface and disallows any transfer of tensile stress across the contact interface. The minimization of penetration of slave nodes is implemented by assigning a penalty in proportion to the penetration distance.

MATERIAL MODEL: The material in this case is Al2024-T3 whose behavior is governed by the following strain-rate and temperature dependent Johnson-Cook material model.

$$\bar{\sigma} = \left[A + B\left(\bar{\varepsilon}^{pl}\right)^{n}\right]\left[1 + C\,\ln\left(\frac{\dot{\bar{\varepsilon}}^{pl}}{\dot{\varepsilon}_0}\right)\right]\left(1 - \hat{\theta}^{m}\right) \quad \text{..... (3.3)}$$

where $\bar{\varepsilon}^{pl}$ is the equivalent plastic strain and A, B, C, n and m are material constants measured at or below the transition temperature T_{trans} . $\hat{\theta}$ is the nondimensional temperature defined as:

$$\hat{\theta} \equiv \begin{cases} 0 & \text{for} \quad T < T_{trans} \\ \dfrac{T - T_{trans}}{T_{melt} - T_{trans}} & \text{for} \quad T_{trans} \le T \le T_{melt} \\ 1 & \text{for} \quad T > T_{melt} \end{cases} \quad \text{..... (3.4)}$$

where T is the current temperature, T_{melt} is the melting temperature, and T_{trans} is the transition temperature defined as the one at or below which there is no temperature dependence on yield stress. The material constants are given below in Table 3.3 [11, 12]. When $T \ge T_{melt}$ the material behaves like a fluid with no shear resistance. In this case the

hardening history of the material is removed by setting $\bar{\varepsilon}^{pl} = 0$. The other material properties used in the model are given in Table 3.4. To speed up the simulation the density of the material is scaled by a fixed mass scaling factor 1000,000.

3.3.4 Results and discussion of section 3.3.3

Fig. 3.9 shows the calculated von Mises stress distribution for the two-pin case at $t = 6.1$ sec. At the center of the workpiece the Mises stress is low indicating local melting. The issue of melting will be discussed later in the context of temperature distribution. It is also observed that behind the shoulder the stress is very high. Behind the shoulder the material tends to rise but the top surface nodes are constrained to lie in or beneath their undeformed location by an analytical rigid surface. This leads to the forging of the material behind the tool. Forging down the material is crucial in producing void-free welds. For the single-pin case no distribution of von Mises stress is presented other than to state that melting of workpiece under the shoulder is observed in a similar fashion which makes the Mises stress low there.

The calculated temperature distribution at $t = 6.1$ sec in the region under the shoulder of the two-pin geometry is shown in Fig. 3.10. From the history output of the total heat generation it is concluded that this is a steady state temperature. The top figure corresponds to the top view and the middle figure corresponds to the front sectional view. The bottom figure corresponds to the temperature profile along a path ABCDEF which is marked in the other figures. The temperature in most of the region under the tool exceeds the melting temperature, i.e. 502˚C. The reason for high values of temperature is that all the mechanical energy dissipated by friction is assumed to convert into heat and that the heat is evenly distributed between master and slave surfaces. Clearly the dissipation of

mechanical work into other forms of energy needs to be taken into account in order to obtain more accurate values of temperature. Also the maximum temperature is achieved around and between the pins and not under the shoulder. The friction at the interface between the pins and the matrix serves as additional source of heat for the material between the pins. The heat loss in this region is also low compared to the material under the shoulder because the later is exposed to much colder surrounding. One more notable feature apparent in the front sectional view is that the temperature at the back of the trailing pin is greater than the temperature ahead of the leading pin. This is to be expected because the material is flowing in the direction from the leading pin to the trailing pin.

Fig. 3.11 shows the calculated temperature distribution for the single-pin case at $t = 1.1$ sec. The temperature profile along a path ABCD is also drawn at the bottom. The steady state temperature profile is not attained at $t = 1.1$ sec as can be seen from the history output of the heat generation. A dip in the temperature close to the pin is observed in comparison to the temperature at the edge of the shoulder which is characteristic of transient temperature field. But here too the entire region under the tool exceeds the melting temperature. Also the temperature at the trailing side of the tool is slightly greater than the temperature at the leading side of the tool.

Fig. 3.12 shows the calculated in-plane plastic shear strain (ε_{12}^{pl}) distribution for the two-pin case at $t = 1.1$ sec. The top view corresponds to the front sectional view whereas the bottom view corresponds to the top sectional view close to the bottom of the workpiece as indicated in the figure. Since the melt pool around the pins rotate with the same velocity as that of the pins, the contact condition is perfectly sticking. Also at the bottom

of the workpiece the influence of the shoulder is minimal. So here a shear strain distribution that resembles that for 2D case is obtained. For example it is observed that the interface is subjected to positive severe shear strain along the weld line and that there are negative shear strains ahead and behind each pin.

Fig. 3.13 shows the calculated in-plane plastic shear strain (ε_{12}^{pl}) distribution for the single-pin case at $t = 1.1$ sec. Here the perfectly sticking condition is not observed everywhere along the pin-surface. From the velocity distribution it is concluded that there is a loss of contact in the regions shown in angular brackets. So the shear strain distribution doesn't quite resemble that for the 2D case. In the perfect-contact zone the material velocity is equal to the pin-surface velocity whereas in the no-contact zone the material velocity is less than the pin-surface velocity. So in the no-contact zone material is compressed (negative plastic shear strain) whereas in the perfect-contact zone material is stretched (positive plastic shear strain). But the magnitude of this positive plastic shear strain is less than that for the two-pin case.

Fig. 3.14 shows a comparison of calculated average in-plane force per pin for the two cases. Average in-plane force is the resultant of the forces parallel to the plane in which the pins move, divided by the number of pins in each case. Even though the average in-plane force is oscillating in nature it is much less for the two-pin case than the single-pin case. The reason is twofold. First the opposite direction of velocity of the two pins close to the interface tends to nullify the forces the matrix exerts on each pin as explained in the 2D analysis. Second the melting of the material takes place in both the cases but due

to the higher temperature attained by the workpiece in the process zone of the two-pin configuration, there is more thermal softening and hence less workpiece resistance.

3.4 Conclusions

- It has been calculated from the simple translation of a pin through the matrix under perfectly sticking friction that the shear zone initiates at the side of the pin. This shear zone gets extruded between the pin and the elastically deformed matrix and flows around the pin from high pressure zone to low pressure zone.
- A 2D plane strain finite element analysis has been carried out to determine the efficacy of the three different geometric configurations, namely (i) single pin (ii) closely spaced two pins rotating in the same direction (iii) closely spaced two pins rotating in opposite direction. It has been found that the calculated von Mises stress and equivalent plastic strain along the joining interface of the two pins rotating in the same direction is maximum among all three configurations.
- The calculated average resistive force of the matrix per pin is the least for the case of two pins rotating in the same direction. From the above inferences it is concluded that a two-pin system with the same direction of rotation is a superior design in comparison to a two-pin system with the opposite direction of rotation.
- 3D thermomechanical simulations were carried out to do a comparative analysis between two configurations, namely (i) the single-pin and (ii) the two-pin with same direction of rotation.

    1. For the two-pin case the calculated steady-state temperature profile at $t = 6.1$ sec shows melting under the shoulder. Also the highest

temperature is attained at the joining interface between the pins and not under the shoulder. The temperature profile for the single-pin case at $t = 1.1$ sec is transient in nature. Still melting is observed under the shoulder.

2. For the two-pin case there is no slip between the pins and the adjacent material. Hence a severe plastic deformation was observed along the joining interface in the same manner as that in the 2D case. For the single-pin case there is a slip between the pin and the material at two locations. Hence the magnitude of the plastic shear strain is less compared to the two-pin case.
3. The calculated average resistive force of the matrix per pin for the two-pin case is less compared to the single-pin case.

3.5 Acknowledgement

This work is sponsored by the National Science Foundation (Grant No. DMI-0544920). Additional support is also acknowledged from the Boeing Airplane Company.

3.6 References

[1] S.W. Kallee, W.M. Thomas and E.D Nicholas, *Magnesium Alloys and their Applications,* Wiley-VCH, Munich, (2000) 175

[2] C.J. Dawes and W.M. Thomas, *Weld. J.* 75(3) (1996) 41.

[3] T.J. Lienert Jr., W.L. Stellwag, B.B. Grimmett and R.W. Warke, *Weld. J.*, 82(1) (2003) 1-s.

[4] A.L. Pilchak, M.C. Juhas and J.C. Williams, *Metall. Mater. Trans.* A 38(2) (2007) 435.

[5] A.K. Ghosh, US Patent No. 7597237, (2009).

[6] S. Mukherjee and A.K.Ghosh, *NSF-DMI Grantees Conference*, St. Louis, MO (2006).

[7] W.M. Thomas, I.M. Norris, D.G. Staines and E.R. Watts, *The SME Summit*, Oconomowoc, Milwaukee, WI (2005).

[8] A. Askari, S. Silling, B. London and M. Mahoney, *Friction Stir Welding and Processing*, TMS Publication, Indianapolis, IN, (2001) 43.

[9] X. Deng and S. Xu, *J. Manuf. Processes* 6(2) (2004) 125.

[10] H. Schmidt and J. Hattel, *Modeling Simul. Mater. Sci. Eng.* 13 (2005)77.

[11] *ASM Handbook*, The American Society of Metals, Metals Park, OH, 2 (1995) 70.

[12] Lesuer. D.R., 2000, "*Experimental Investigations of Material Models for Ti-6Al-4V Titanium and 2024-T3 Aluminum*", www.tc.faa.gov/its/worldpac/techrpt/ar00-25.pdf, pp. 18.

$\rho(kg/m^3)$	$E(GPa)$	ν
7800	210	0.3

Table 3.1. Material property data for steel.

$K(MPa)$	$\sigma_0(MPa)$	n
650	250	0.18

Table 3.2. Material constants in the hardening curve of steel in eqn. 3.1.

$A(MPa)$	$B(MPa)$	n	C	$\dot{\varepsilon}_0(s^{-1})$	$T_{melt}(^{\circ}C)$	$T_{trans}(^{\circ}C)$	m
369	684	0.73	0.0083	1	502	25	1.7

Table 3.3. Material constants in the hardening curve of Al2024-T3 in eqn. 3.3.

Conductivity	190.4 $Wm^{-1}K^{-1}$
Density	2770 $kg.m^{-3}$
Young's modulus	73.1 GPa
Poisson's ratio	0.33
Thermal Expansion Coefficient	2.268E-5 K^{-1}
Specific Heat	875 $Jkg^{-1}K^{-1}$

Table 3.4. Material property data for Al2024-T3.

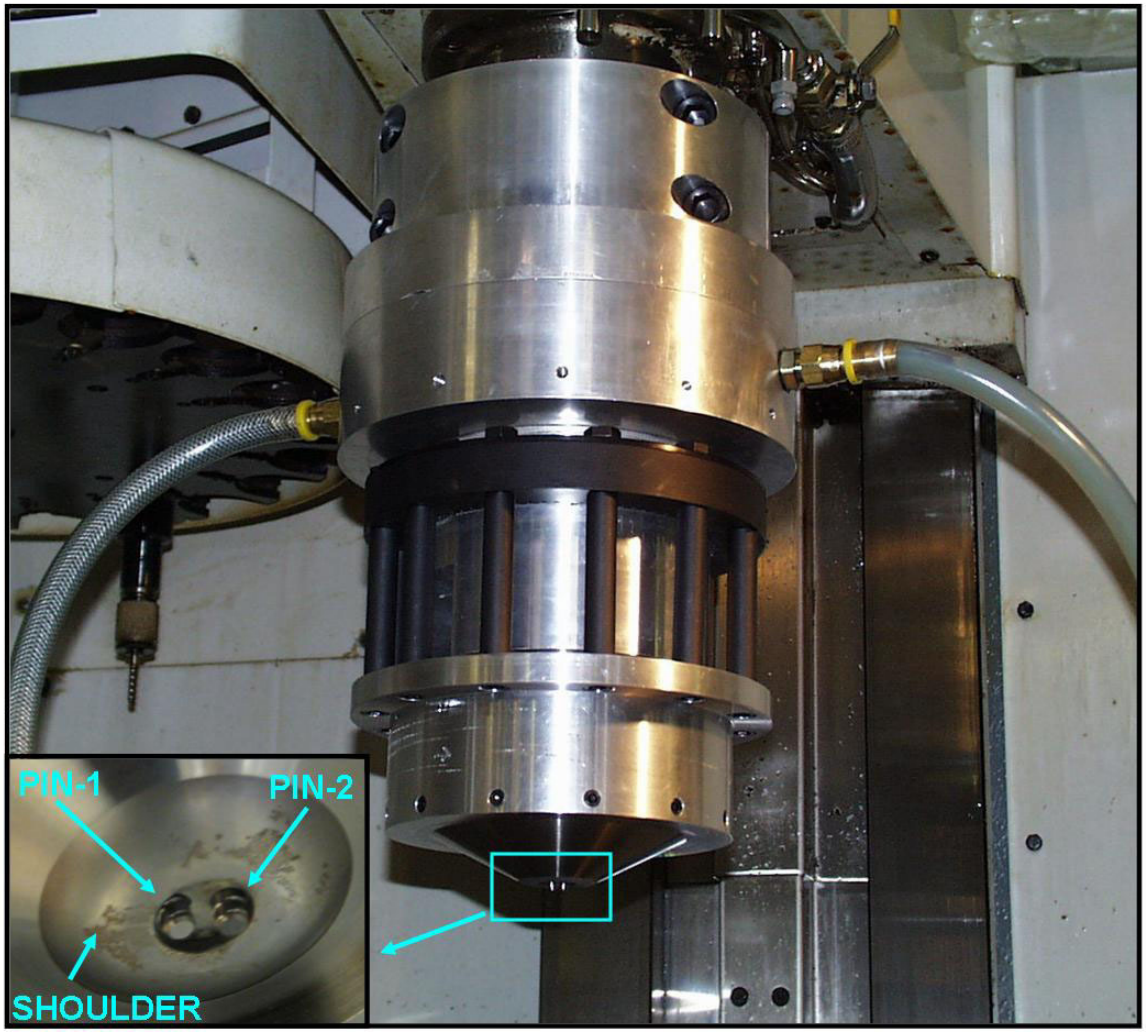

Fig. 3.1 The Friction driven stitch welding apparatus. (Inset) the pins and shoulder are shown.

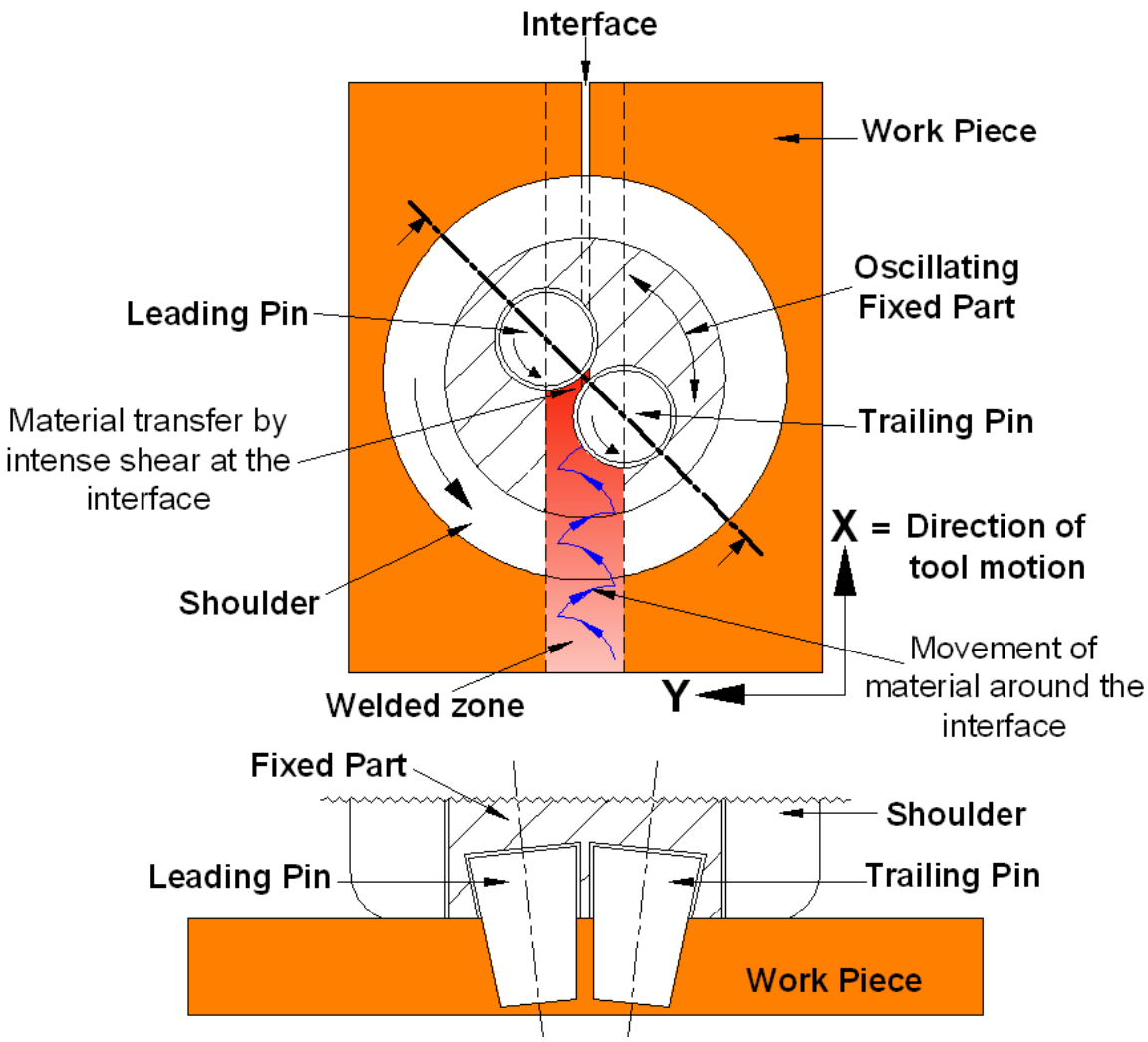

Fig. 3.2 Schematic of the concept of two-pin friction driven stitch welding according to [5]. The bottom view is the rotated sectional view along the plane shown in the top view.

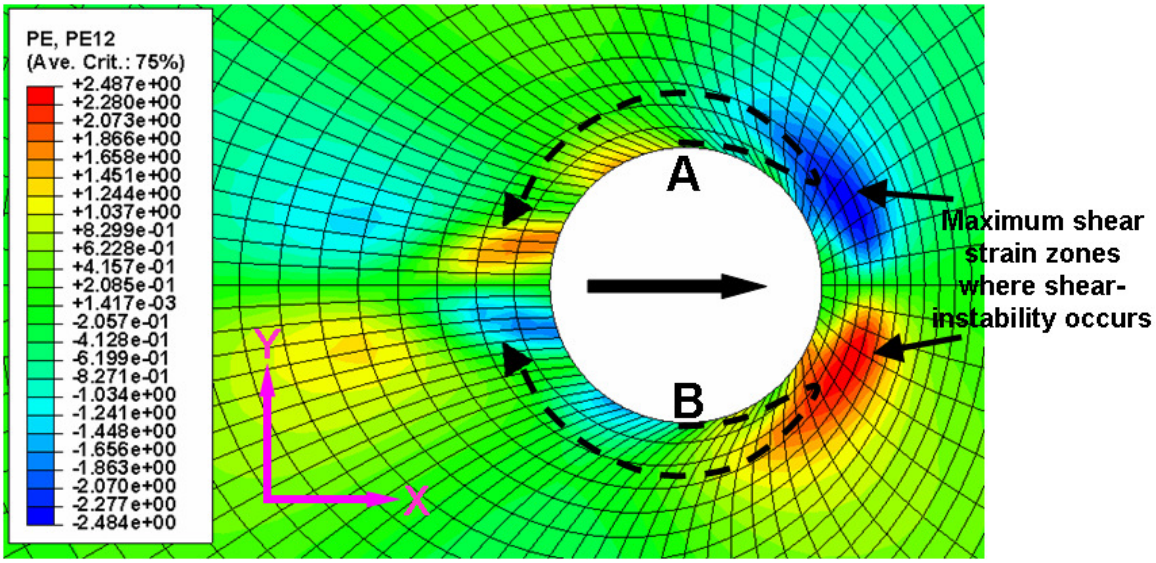

Fig. 3.3 Calculated shear zone development due to traverse of a single pin. The path of the movement of sheared layer is shown by broken arrows.

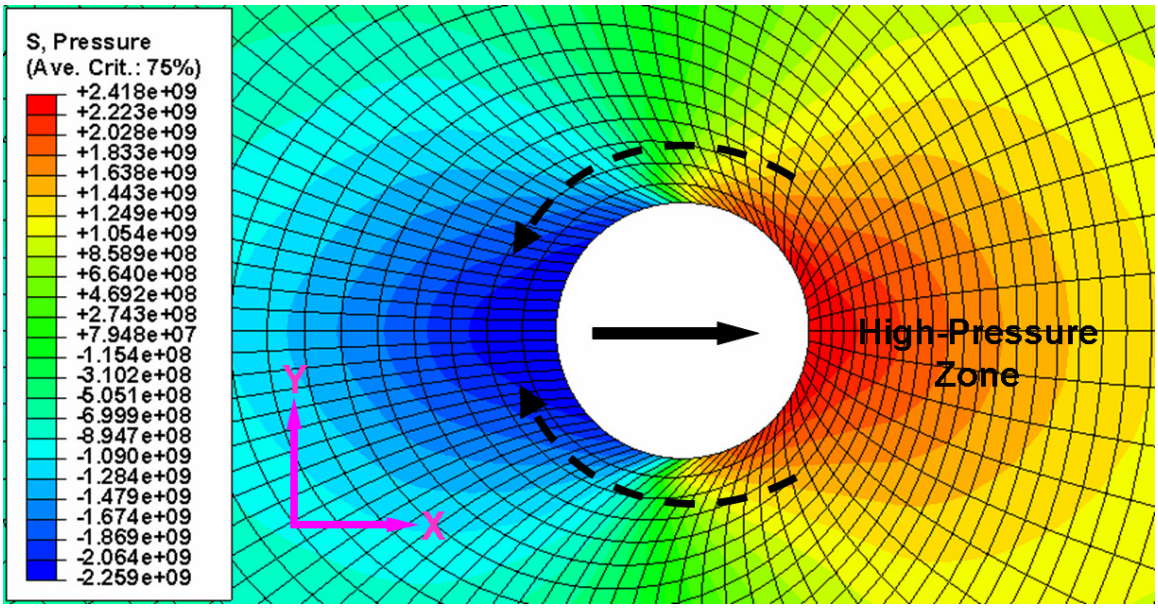

Fig. 3.4 Calculated pressure development due to traverse of a single pin.

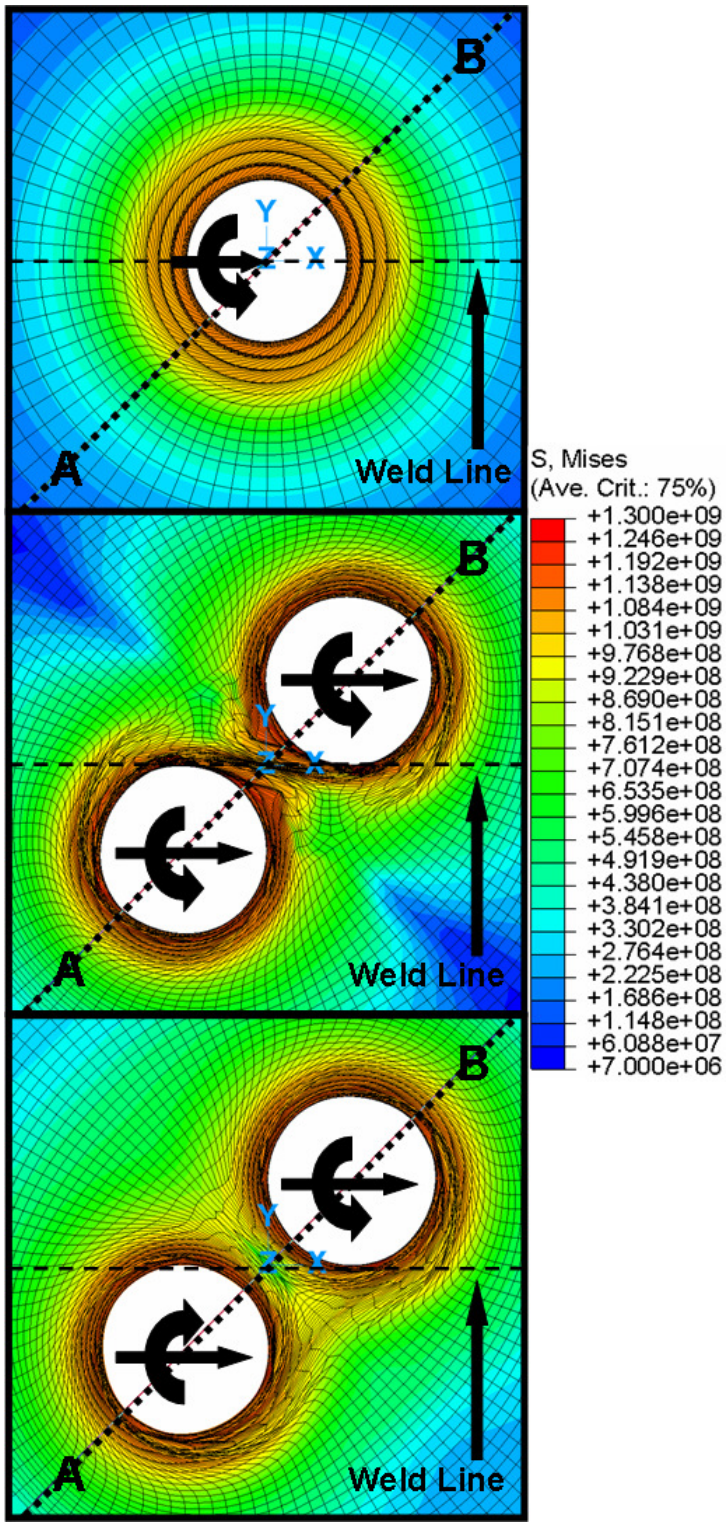

Fig. 3.5 The calculated von Mises stress distribution for the three cases considered in the 2D analysis. Arrows indicating pin rotation and translation are shown. Path AB is also shown.

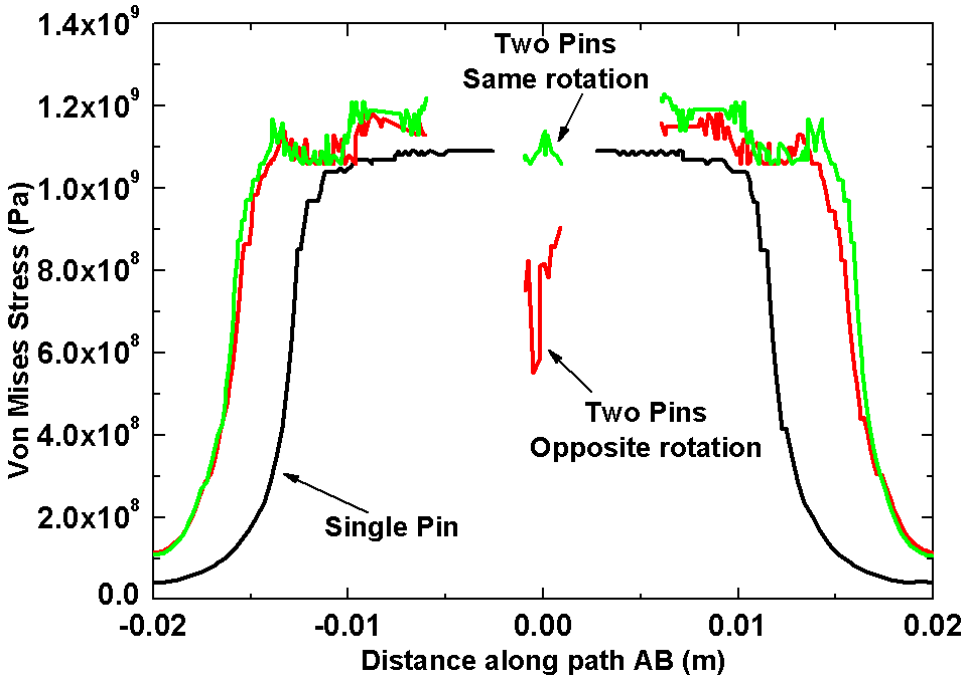

Fig. 3.6 The calculated von Mises stress plotted along path AB for the three cases. The discontinuous segments of the curves correspond to the extremities of the pins.

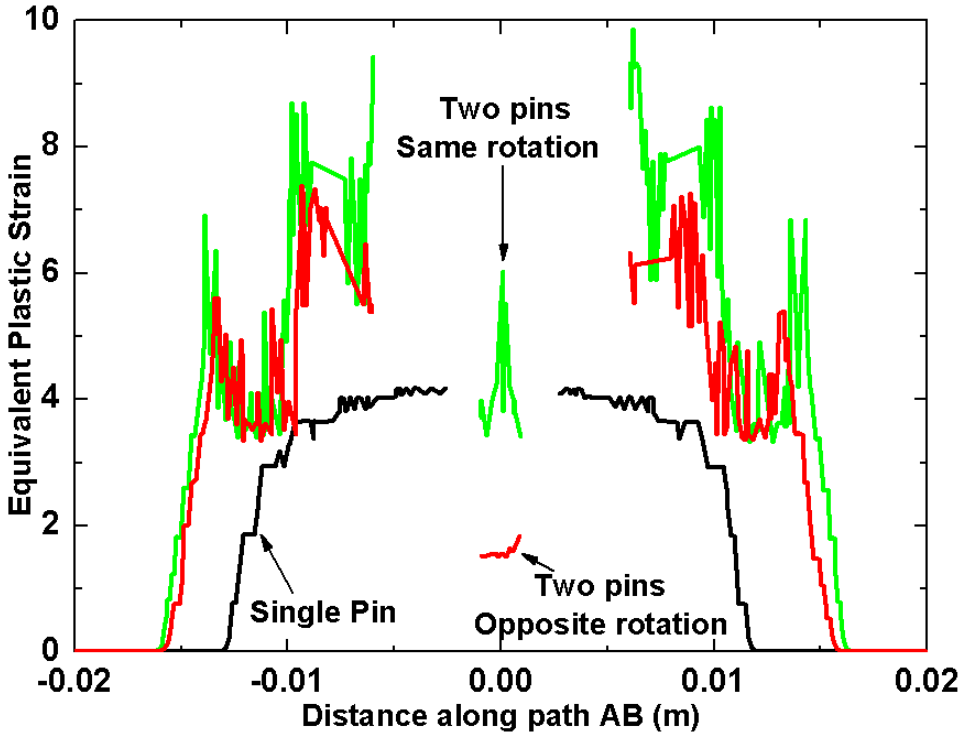

Fig. 3.7 Calculated equivalent plastic strain plotted along path AB for the three cases. The discontinuous segments of the curves correspond to the extremities of the pins.

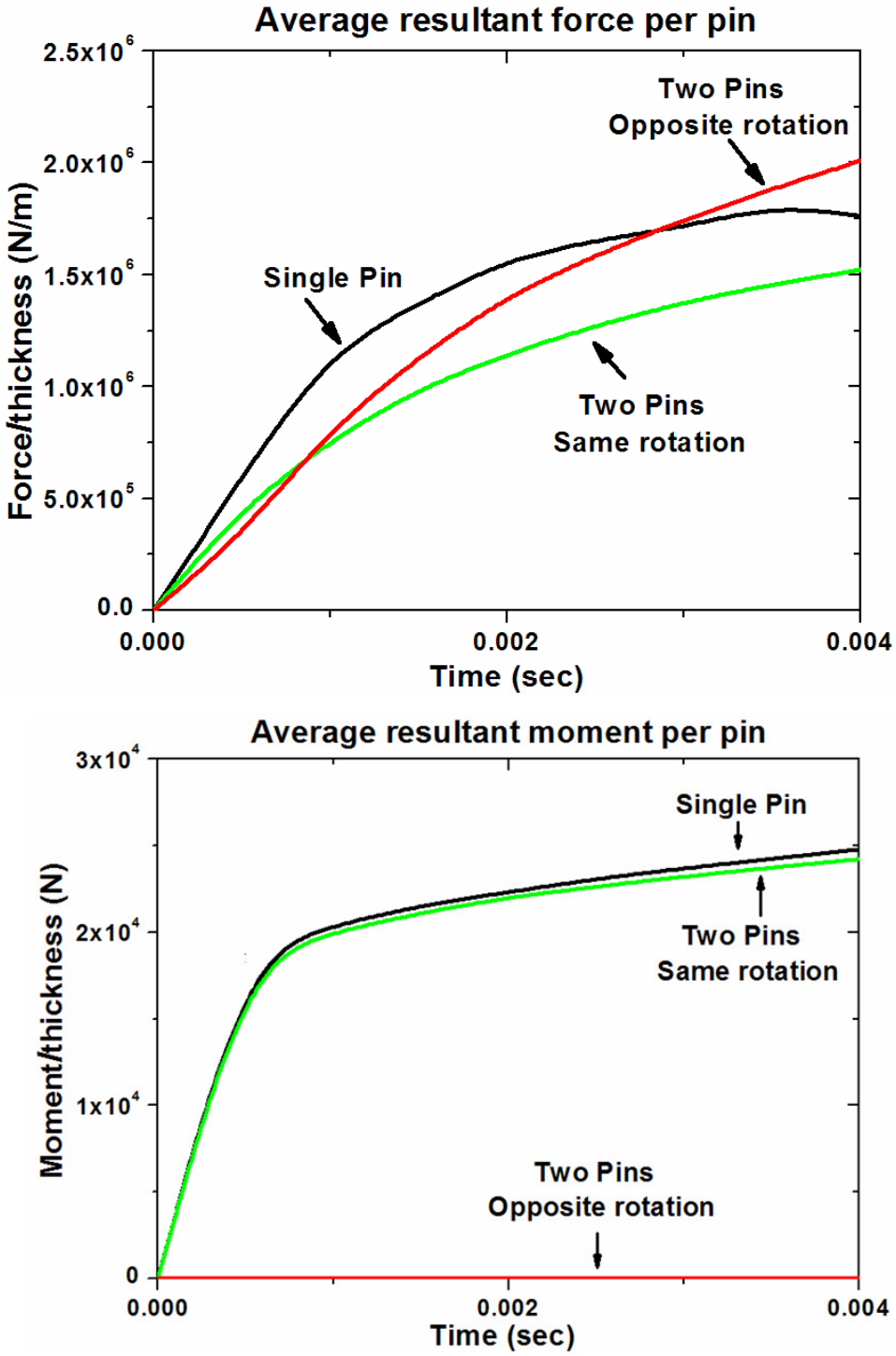

Fig. 3.8 Time evolution of average force and average moment per pin calculated for all three configurations.

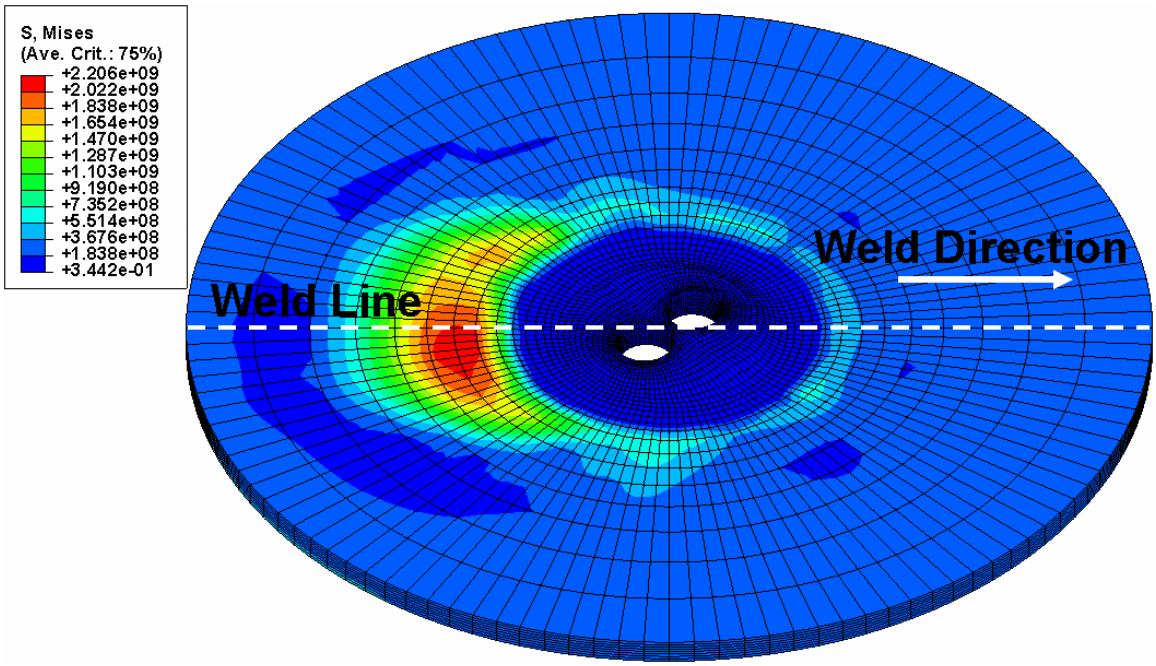

Fig. 3.9 The calculated von Mises stress distribution at $t = 6.1$ sec for two-pin rotating in the same direction.

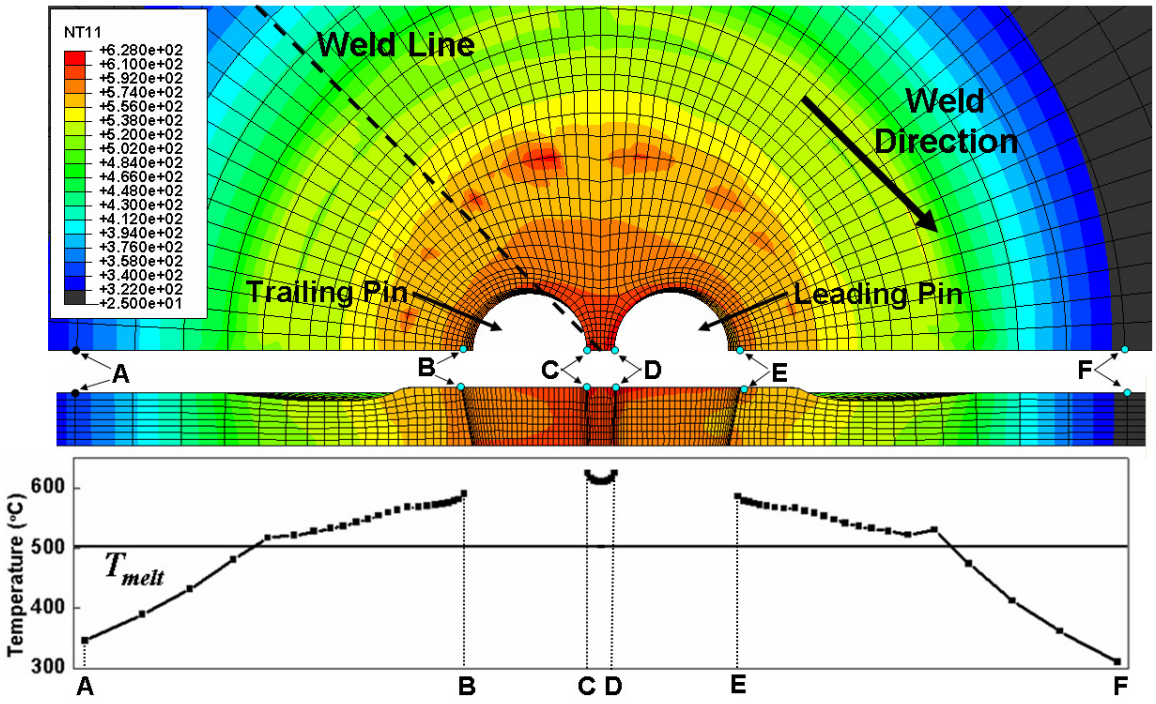

Fig. 3.10 Calculated nodal temperature distribution for two-pin case at $t = 6.1$ sec. In the top and front sectional views, path ABCDEF is shown. The temperature profile is drawn along path ABCDEF. The melting temperature $T_{melt} = 502\,^{\circ}\mathrm{C}$ is shown by the horizontal line.

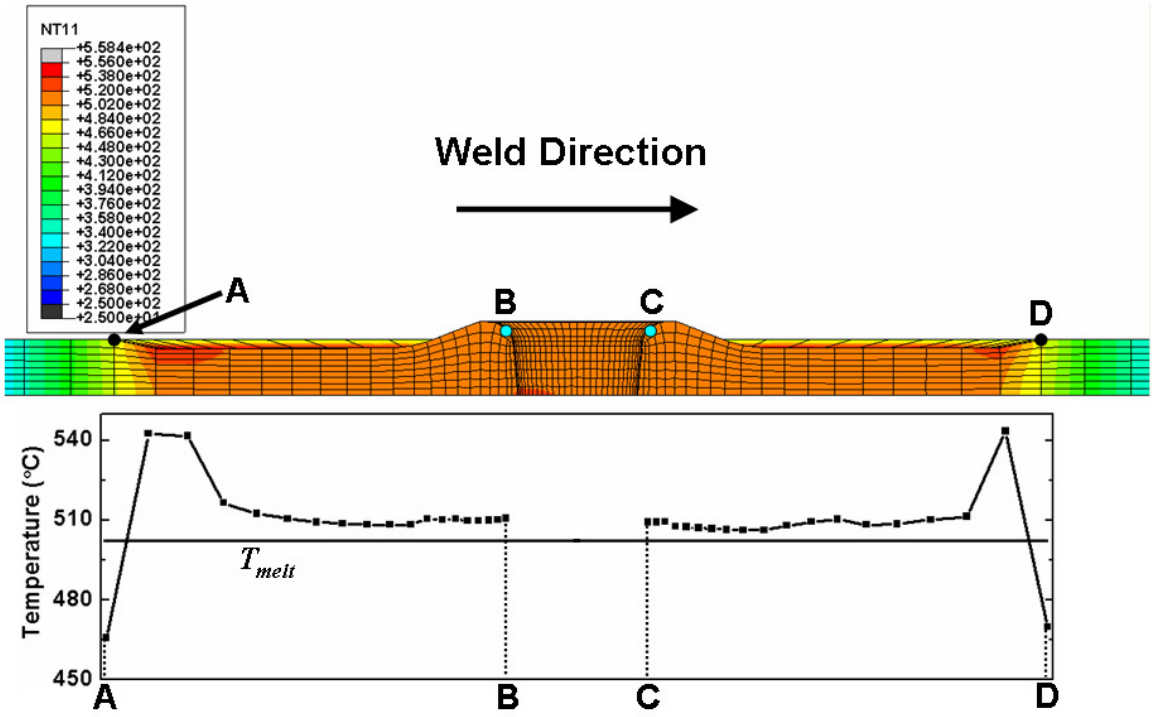

Fig. 3.11 Calculated nodal temperature distribution for single-pin case at $t = 1.1$ sec. In the front sectional view, path ABCD is shown. The temperature profile is drawn along path ABCD. The melting temperature $T_{melt} = 502\,^{\circ}\mathrm{C}$ is shown by the horizontal line.

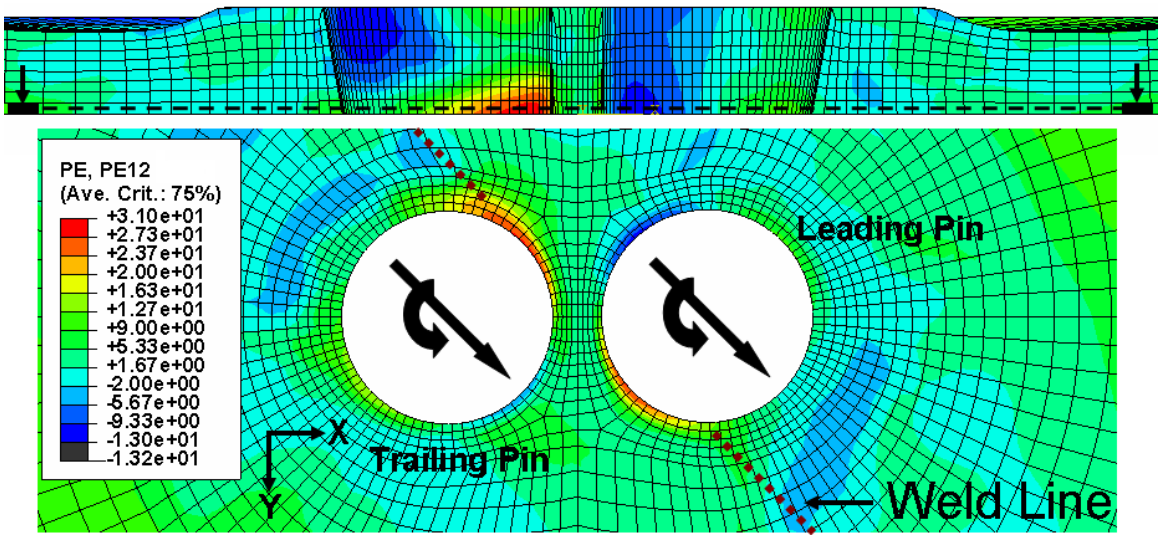

Fig. 3.12 In-plane plastic shear strain calculated for the case of two pins at $t = 1.1$ sec. The bottom view is a top sectional view close to the bottom of the workpiece.

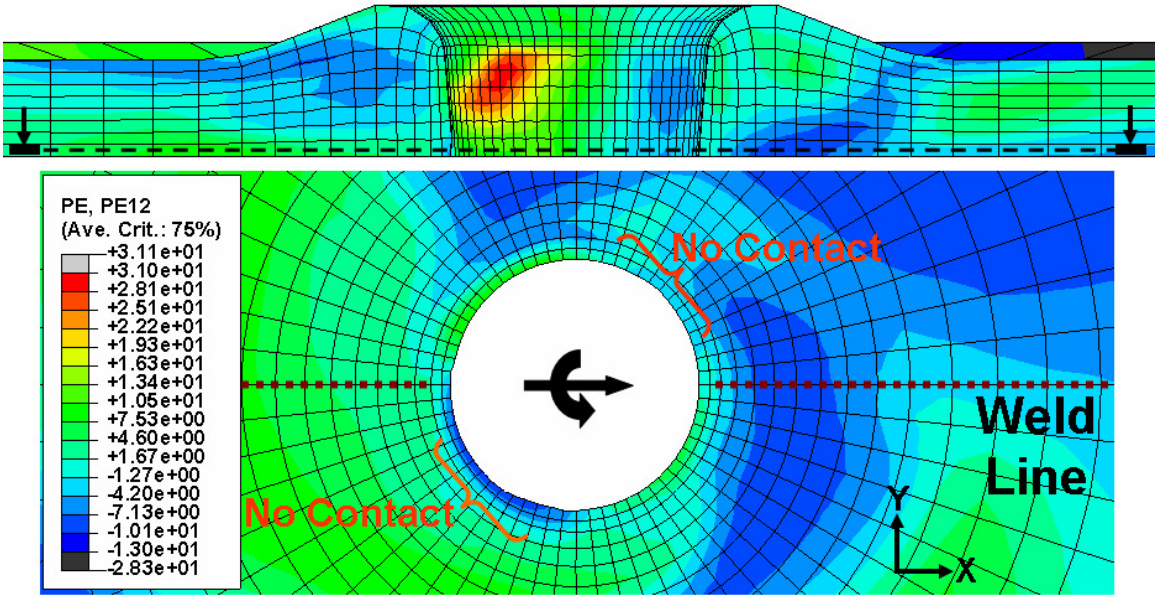

Fig. 3.13 In-plane shear strain calculated for the case of single pin at $t = 1.1$ sec. The bottom view is a top sectional view close to the bottom of the workpiece.

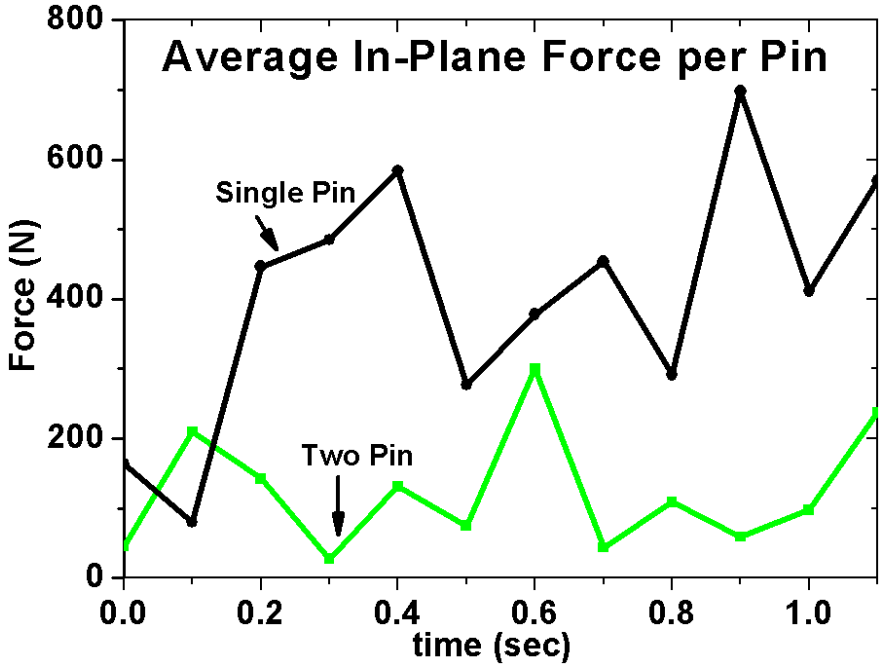

Fig. 3.14 Calculated average in-plane force per pin plotted against time for the two cases.

Chapter 4

Experimentation Using Friction Driven Stitch Welding Apparatus

Abstract

The Friction Driven Stitch Welding (FDSW) apparatus, described in Chapter 3, is fabricated and tested. Modifications of the FDSW apparatus, deemed necessary to lend it functionality, are also described.

4.1 Introduction

As described in Chapter 3, the shear rate within the material can be enhanced by using two closely spaced pins rotating in the same direction. This idea was employed to fabricate the FDSW apparatus. The details of development of this apparatus and its further modifications are described in this chapter.

4.2 The FDSW Apparatus

DESCRIPTION: A design of the FDSW apparatus is shown in Fig. 4.1. The actual apparatus mounted in a milling machine is shown in Fig. 4.2. At the bottom of the apparatus, two conical pins stick out of the rotary shoulder as shown in Fig. 4.1. The

shoulder and pins rotate independent of each other. The main power of the apparatus comes from milling machine motor which gets divided into two branches by a series of gears. The spur gear assembly also drives the outer ring-gear which in turn drives the shoulder. The shafts which deliver power to the pin are inclined 6° with respect to the vertical. The angular transmission of power is achieved by using universal joints. The angular disposition of the pins allows them to come at close proximity in the process zone but space out in the housing where they are mounted. A cooling/lubricating fluid flows along the interface between rotating spindles and housing as well as the pin-tips. This is necessary because the pin tips are expected to get hot during FDSW. The thrust load on the shoulder is transmitted to the housing via a thrust bearing. Also the alignment during rotation of the shoulder is maintained by a caged-needle-bearing assembly.

TESTING: The apparatus was tested and it ran fairly smoothly. However couple of design changes became necessary after testing.

- Slight wobbling of the ring-gear was observed due to which there were spikes of load. The wobbling of ring-gear was because it was not supported at both ends by bearings.
- While carrying an actual run of FDSW a high load on the milling machine motor was observed. There are a large number of rotating parts in FDSW apparatus, e.g., the gears, gear-shafts, U-joints, spindles and pin-tips. Added to that are the ring-gear, the rotary-housing and the shoulder which are massive and away from the rotation axis. Thus they have a large moment of inertia and considerable horse-power is required to keep these parts in motion.

The milling machine motor supplies a maximum power of 2.5hp at 1000rpm. This was deemed inadequate to run the complete FDSW apparatus. Thus a decision was made to use a separate power supply for the movement of the shoulder and rotary-housing which had large rotary inertia.

4.3 Modified FDSW- Bosch Grinder Apparatus with Cage

DESCRIPTION: The motor was selected to have sufficient horsepower to rotate the shoulder and rotary-housing during FDSW. Also the motor needed to be lightweight enough so that it could be mounted in the FDSW apparatus. A Bosch 1873-8 large angle grinder which is shown in Fig. 4.3 fulfilled these two requirements. The grinder motor can supply 3HP at 8500 RPM which was deemed sufficient for FDSW. Fig. 4.4 and Fig. 4.5 show the assembly which was used to mount the motor with FDSW apparatus. A sturdy cage was formed around the apparatus so that vibration due to motor was not transferred on the apparatus. The power was supplied from the motor to the shoulder via a V-belt.

TESTING: The system also ran smoothly. The shoulder and the pins were independently powered. However during an actual run the following problem was encountered. As load was applied on the shoulder, Bosch motor started drawing large amount of current. The maximum current capability of the supply line is 30A beyond which the circuit is tripped. High current is undesirable for the Bosch motor itself which is designed to draw only 15A. It was concluded that even though the motor could supply the desired power it had low torque capability under the current and voltage settings. During FDSW process high torque is required to shear the metal. The motor was unable to supply the torque and started drawing large amount of current.

4.4 Future Work - Modified FDSW Apparatus Driven by Thin Ring High Torque Motor

The future design (Fig. 4.6) includes a thin ring high torque motor which is to be used to run the shoulder. This motor is an Allied Motion Megaflux Series (MF0255025) brushless motor which is to be installed inside the equipment thus permitting high torque in a confined space. The motor comes with a separate controller and power supply which guarantees required power and torque. The motor has a continuous stall torque of 31N.m. It is believed that this motor is capable of supplying the required torque and power for the FDSW apparatus.

4.5 Summary

The friction driven stitch welding apparatus was tested using a single power source of a milling machine. The milling machine motor reached its limiting torque capacity before stitch welding could take place. A separate power source, i.e. a Bosch grinder motor, was connected to drive the rotating parts of the FDSW apparatus. However, on application of load to the shoulder, the grinder motor drew significant amount current, well above its rated amperage thus tripping the circuit. A thin-ring, high-torque brushless motor, which has a high continuous torque capacity, is recommended for further development of the FDSW apparatus.

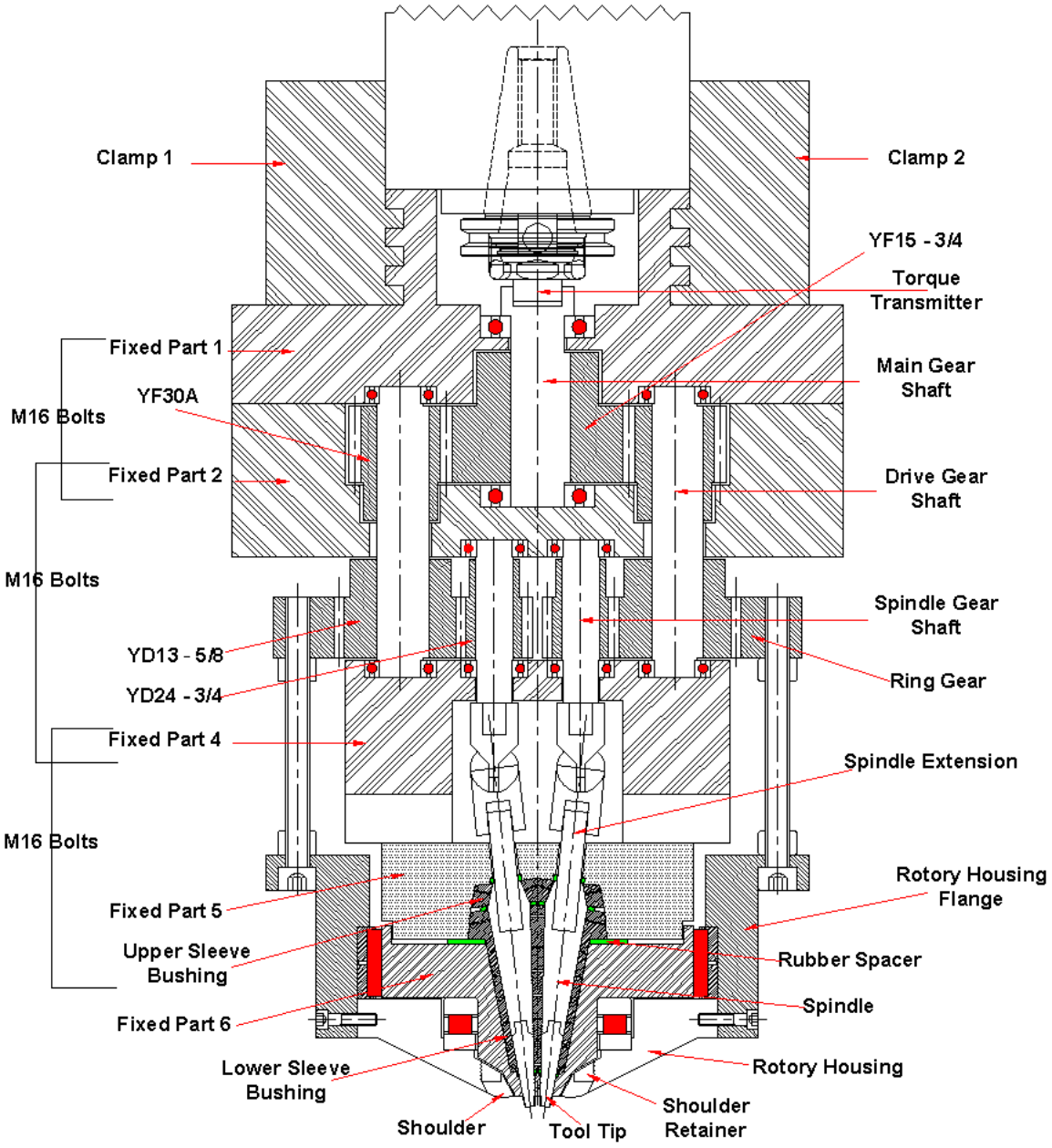

Fig. 4.1 Design of the friction driven stitch welding apparatus.

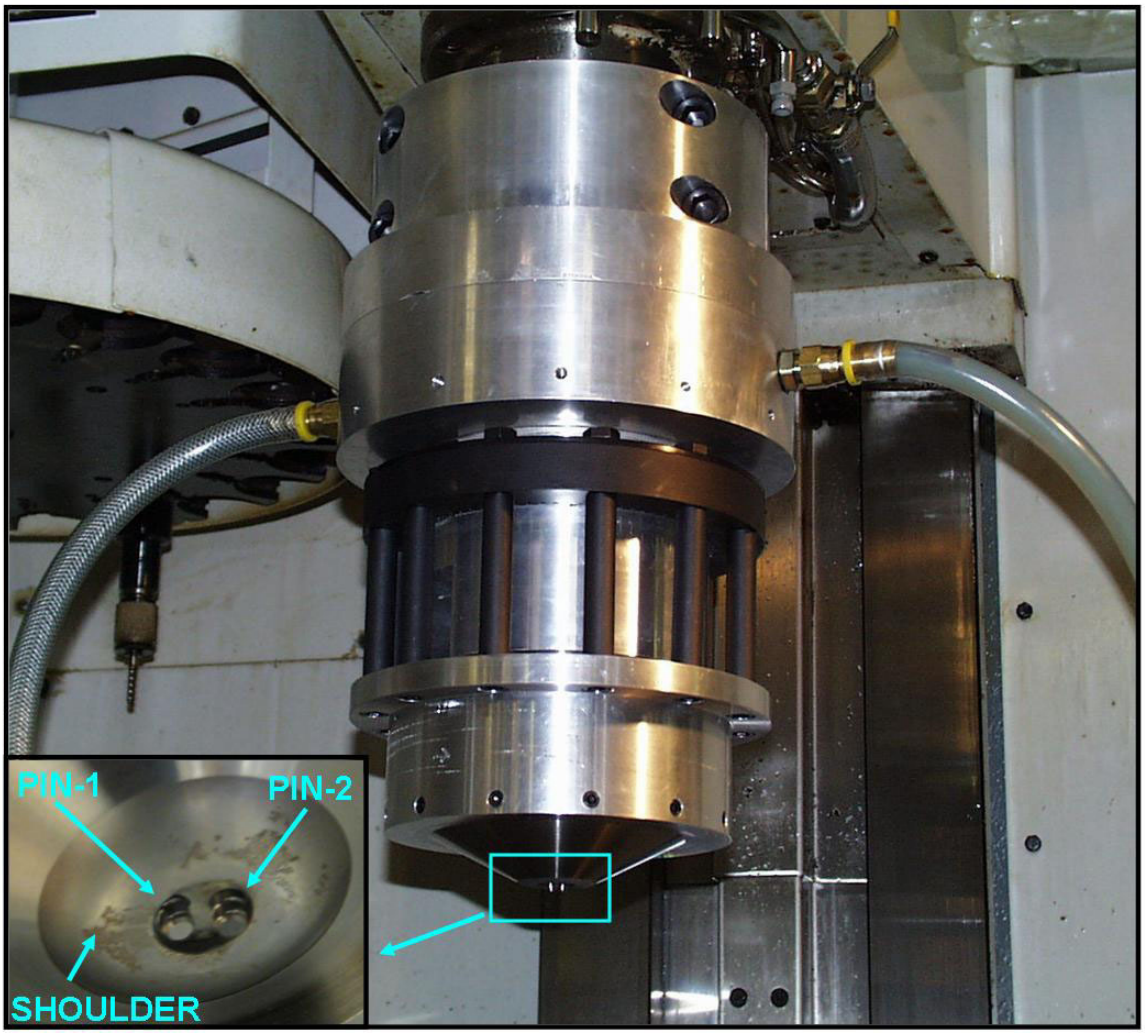

Fig. 4.2 The fabricated friction driven stitch welding apparatus. (Inset) The pins and shoulder are shown.

Fig. 4.3 A Bosch large angle grinder.

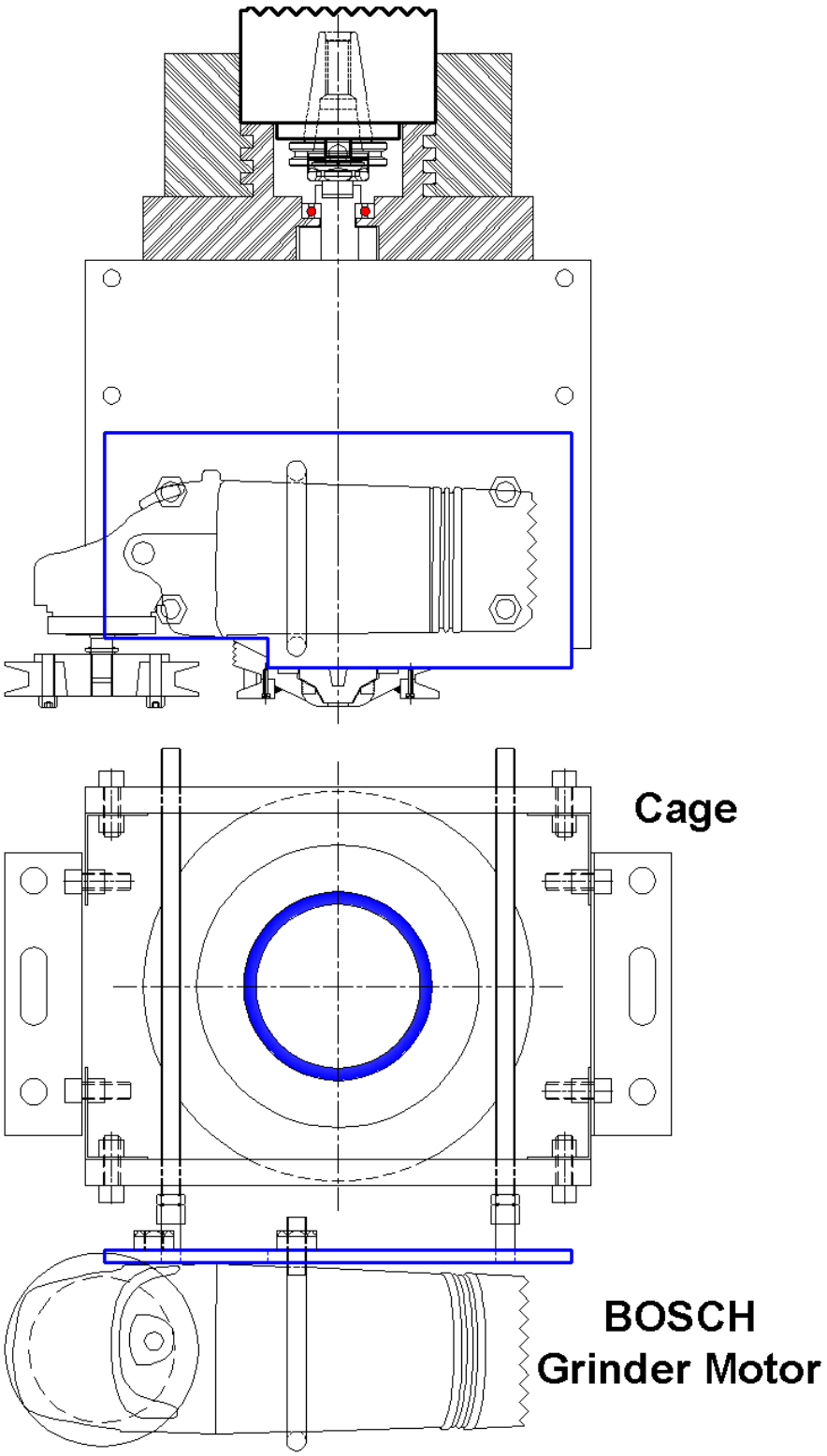

Fig. 4.4 Modified friction driven stitch welding apparatus with Bosch grinder motor as a power supply to the shoulder.

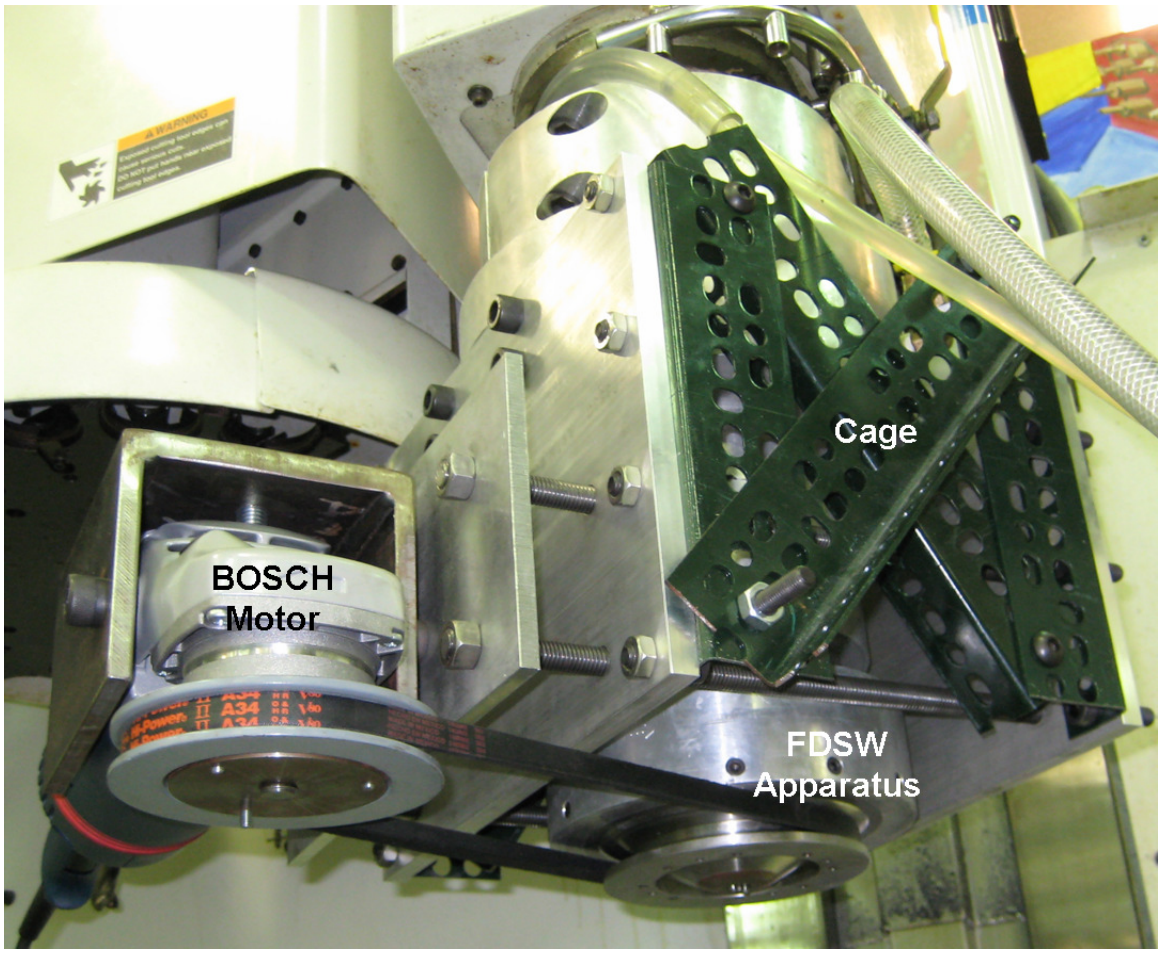

Fig. 4.5 An image of the modified friction driven stitch welding apparatus with Bosch grinder motor.

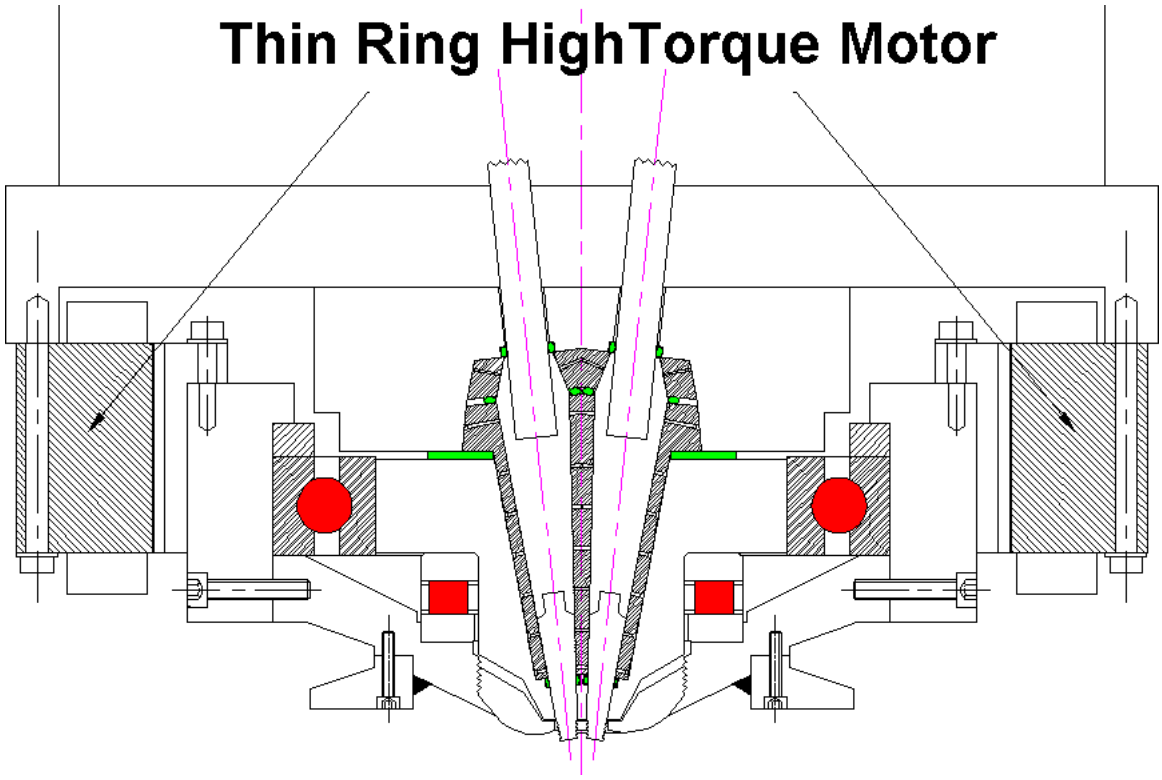

Fig. 4.6 Thin ring high torque motor to be used to drive the shoulder.

Chapter 5

Friction Stir Processing of Direct Metal Deposited AISI 4340 Steel – a Novel Technique of Damage Repair

Abstract

A combination of laser-assisted Direct Metal Deposition (DMD) and Friction Stir Processing (FSP) was used to explore techniques of repair of an AISI 4340 steel part which underwent seawater corrosion. FSP of DMD-deposited AISI 4340 steel is the subject of this research. Appropriate heat treatment of DMD deposit was undertaken prior to FSP. Microstructural characterization was performed after every processing step and was related to the mechanical property. Corrosion behavior was also evaluated before and after FSP. It was observed that FSP increases the ductility of the DMD deposit without affecting corrosion rate.

5.1 Introduction

Many navy weapons systems and support equipments are complex and expensive components which are subjected to constant wear and corrosion. Replacement of old parts and procurement of new ones which are low in quantity but high in value can be difficult and costly [1]. For this reason, research regarding repair and restoration of existing components is extremely important. Towards that end laser-assisted DMD was already employed to repair turbine blades, torpedo

shells, tools, dies etc [2-4]. However DMD process is often limited by porosity [5], cracking [6], residual stress [7], and solute segregation [8] in the deposit which adversely affect mechanical integrity and/or corrosion resistance. Some of these limitations can be overcome by surface modification of DMD deposit via friction stir processing. FSP was employed to reduce porosity in cast alloys and refine microstructure in wrought alloys including 304L stainless steel, aluminum and copper [9, 10]. Thus a combination of DMD followed by FSP can be used to produce superior quality of repair, but such an idea has hardly been explored.

In this chapter the effects of FSP on a sample of DMD 4340 steel were investigated. A methodology of repair of a large area in a DMD 4340 steel part using FSP was developed. The repair process was kept "local", namely, the processing and heat treatment involved in the repair region did not influence the structure and properties of other regions of the part. The navy part under investigation was exposed to seawater and underwent loading. In view of that particular attention was given to mechanical integrity and corrosion resistance of repair.

5.2 Experimental

The overall methodology of repair using DMD and FSP is described in Fig. 5.1. The corrosion hole present in the marine component was machined to a regular shape. In certain situations this may mean removal of an entire layer of material containing the corrosion hole. The machined hole was subsequently filled with DMD deposit. For reasons explained later, the DMD deposit was flame-treated followed by FSP. The final surface finish was obtained by grinding. The scope of this investigation was limited to the processing of as-deposited DMD 4340 steel layer on an AISI 4340 steel substrate, supplied by POM Group Inc., Auburn Hills, Michigan, USA. The substrate dimension was 125mm × 101.6mm × 51mm and the DMD layer dimension was 102.5mm × 101.6mm × 4.2mm. The chemical compositions of DMD and substrate are listed in

Table 5.1. As discussed later, the DMD layer had martensite microstructure which imparted high hardness to the deposit. The substrate microstructure however consisted of ferrite and pearlite, which is why the substrate is much softer than the DMD. To maintain integrity of repair it is desirable that the microstructure, strength and ductility of the repaired area are similar to that of the substrate. It is also advantageous to soften as-deposited DMD layer prior to FSP to prevent tool wear. In view of that a local heat treatment was employed on the surface of the sample using an oxy-propane torch. The torch was moved uniformly over the entire surface of the sample so that the temperature was nearly uniform. To minimize the heat loss, the sample was insulated all around with alumina felt except at the top surface. A K-type thermocouple was used to periodically measure the surface temperature of the sample. Flame heating was stopped after approximately 45 min when the surface temperature reached 720°C which was slightly below the A_1 temperature (729°C). The sample was subsequently cooled while it was insulated all around including the top surface.

Flame softening of DMD 4340 steel was followed by friction stir processing using a flat annular shaped tool which was made out of a tungsten alloy. This tool had only a flat, annular shoulder and no pin as shown in Fig. 5.1. It also had a recess in the center to allow the material to flow in. It performed surface processing of the work-piece by imparting large force under relatively high temperature. The process zone extended well below the surface. The tool was cooled using a continuous supply of water to prevent overheating. FSP was carried out at a tool rotation rate of 800rpm and a feed rate of 12.7mm/min. The tool was plunged to a depth of 0.13 mm inside the surface of the deposit which ensured large contact load during FSP.

The 4340 samples were etched using 2% nital. Scanning electron microscopy was used to analyze the microstructure of 4340 steel sample under various processing conditions. Vickers microhardness was measured along various regions and is related to the microstructure. TEM

samples were prepared from both within and outside the process zone of FSP 4340 steel sample. First thin slices of 300-400 µm thickness were cut from the FSP sample using diamond saw. Then 3 mm diameter discs were punched out from the slices and these discs were further ground using abrasive SiC papers to approximately 10-20 µm thickness. These thin discs were further prepared by using dimple grinder followed by ion milling to make them electron transparent. A JEOL 3011 TEM operating at 300 kV was used to investigate the microstructure.

Repair of a large area required multiple overlapping FSP passes. To understand the nature of overlap among FSP process zones, two different processing schemes were created as shown in Fig. 5.2. In the scheme shown in Fig. 5.2A the FSP passes do not overlap and the retreating edge of one pass coincides with the advancing edge of the next pass. However in Fig. 5.2B a second set of FSP passes exist midway between the first set of passes which ensures a 50% overlap. Using the second scheme (Fig. 5.2B) an area large enough to prepare tensile and corrosion test specimens was processed.

Corrosion test specimens were extracted from substrate, DMD and FSP 4340 steel samples. Another specimen was extracted which contained half DMD and half substrate with the interface plane between DMD and substrate lying at mid-thickness of specimen. Yet another corrosion specimen with half FSP and half substrate was also extracted. All corrosion test specimens were sent to Corrosion Testing Laboratories Inc., Newark, Delaware, USA. The specimens were rectangular in shape of dimension 50.8mm × 25.4mm × 3.3mm. The specimens had a 3.2mm diameter through-hole at one side to keep it suspended using a string. The corrosion rate was determined by exposing the specimens to synthetic seawater at laboratory ambient temperature (20°C) for 30 days as per ASTM-G31 standard. The test solution was prepared from commercially available synthetic seawater salt (Lake Products, Maryland Heights, Missouri, USA) that met ASTM D1141 standard. The salts were dissolved in de-ionized water to prepare

the final test solution which had a pH of 8.2. A poly-tetra-fluoro-ethylene string was used to keep the test specimens suspended and totally immersed in the test solution. The test vessel was sealed off for the remainder of duration of the test. After 30 days of exposure the test specimens were removed, cleaned, reweighed and visually evaluated.

Tensile test specimens were extracted from substrate, DMD and FSP 4340 steel samples and are tested in-house. The specimen had a gage length of 15.2mm, a gage width of 6.5mm and a gage thickness of 3.3mm. It also had a shoulder region of radius 6.35mm and a grip section of length 15.5mm on both sides. For the FSP sample the longitudinal axis of the tensile test specimen was perpendicular to the FSP pass direction. Room temperature tensile tests were performed at a constant crosshead speed of 0.5mm/min.

5.3 Results and Discussion

5.3.1 Electron Microscopy

Fig. 5.3A shows a macro-image of as-deposited DMD and substrate 4340 steel. Fig. 5.3B and 5.3C show the microstructure of as-deposited DMD and substrate 4340 steel respectively. In Fig. 5.3A the top surface of the DMD shows individual layers corresponding to each pass of laser beam. The as-deposited DMD (Fig. 5.3B) consists of martensite and bainite whereas the substrate (Fig. 5.3C) consists of ferrite and pearlite. Even though the microstructure of as-deposited DMD is shown here as dual phase martensite and bainite, on other occasion virgin and/or tempered martensite microstructure were observed. Essentially the microstructure of as-deposited DMD depends on the local temperature, cooling rate and thermal history – which can be highly transient and complex during laser deposition. The simplest scenario is a highly rapid solidification of the melt pool under the laser beam, which yields predominantly virgin martensite. However the virgin martensite can undergo tempering as the laser beam passes through adjoining regions. The

extent of tempering depends upon laser power, beam diameter and speed, shielding gas flow rate etc. The aforementioned factors also govern the solidification rate of the melt pool which can be moderate so that phases other that martensite can form. A TTT diagram of 4340 steel [11] shows a “bainite nose” at the lower portion of the diagram. A cursory analysis shows that a low cooling rate of 10°C/sec between 500°C and 300°C can yield bainite microstructure.

The purpose of flame softening is to further temper the DMD layer and improve its toughness. The choice of heating using a flame as opposed to conventional furnace heating is dictated by the requirement of local repair. Furnace heating would require that the whole part be heat-treated. During various stages of the tempering of martensite, there is segregation of carbon atoms into transition carbide and eventually to cementite and ferrite. However the extent of carbide segregation depends on the temperature and time and this results in a gradient in microstructure along the depth of DMD layer. The microstructure of flame softened DMD layer is shown in Fig. 5.4. At mid-depth of DMD layer (Fig. 5.4C) the microstructure still consists of bainite and martensite. However microstructure at the top of DMD layer (Fig. 5.4B) becomes a mixture of bainite, allotriomorphic ferrite and ferrite-carbide aggregate.

Fig. 5.5A shows the sectional view for a single FSP pass. The heat affected zone underneath the tool has a “U” shape and the trough of the “U” lies approximately 3.6mm below the top surface. Fig. 5.5B shows the microstructure of the FSP process zone which appears to be martensitic. However outside the process zone the microstructure (Fig. 5.5C) consists of bainite, ferrite and ferrite-carbide aggregate which is similar to the flame-softened microstructure. The microstructure in Fig. 5.5B can’t be resolved unequivocally, so further investigation is carried out by extracting TEM samples from within the FSP process zone. Fig. 5.6 shows a bright field image showing a lens shaped martensite. Selected area diffraction patterns from martensite grains are used to calculate the lattice parameter. The obtained lattice parameters are $a = b = 2.856$Å and

c = 2.902Å which corresponds to BCT structure. Fig. 5.7 shows a bright field image of another region of the TEM sample. A selected area diffraction pattern obtained from the region marked "F" is used to calculate the lattice parameter. The lattice parameter of BCC ferrite is a = 2.905 Å. This confirms that the heat affected zone under the FSP tool has a mixed microstructure involving martensite and ferrite. The presence of martensite at the top of FSP stir zone where there was none before FSP, leads to the belief that temperature there reaches above the ferrite-to austenite (A_1) transformation temperature. This is what is suggested by Konkol et al [12] in the context of FSW of HSLA-65 steel. Also Lienert et al [13] has measured the peak temperature at the shoulder during FSW of mild steel to be approximately 990°C. It seems eminently possible that the 4340 steel material under the shoulder rises above A_1 temperature, austenizes and quickly forms martensite as the FSP tool leaves the process zone.

Fig. 5.8 shows the microstructure of three FSP passes in sectional view. The microstructure is a result of multiple FSP passes without overlap as shown in Fig. 5.2A. It's apparent from the macrograph that even though the FSP passes don't overlap the heat affected zones do overlap. However the depth of the process zone is non-uniform and minimum in between passes. It is expected that FSP passes in Fig. 5.2B with 50% overlap will create more uniform depth of process zone.

5.3.2 Hardness

In Fig. 5.9 the hardness profiles of three different treatment conditions of DMD 4340 sample are compared, namely, (1) as-deposited (2) flame-softened (3) flame-softened followed by FSP. The as-deposited DMD microstructure contains martensite which is why the hardness is high at the top surface (~ 640 HVN). However as-deposited DMD layer hardness decreases with depth. In the current sample, DMD consists of four layers. During the deposition of a layer, all the layers lying beneath it undergo tempering via conductive heat transfer. Thus the DMD layer adjacent to

the interface undergoes the most tempering and is the softest DMD layer (Hardness ~ 540 HVN). The 4340 steel substrate structure is ferrite-pearlitic, which is why the hardness is relatively low (~ 345 HVN). On flame-softening the martensite at the top of the DMD layer undergoes tempering and transforms to ferrite and cementite. But underneath the surface this transformation remains incomplete and the extent of tempering decreases with depth. After flame-softening the top surface is relatively soft (Hardness ~ 350 HVN). After FSP the heat affected zone undergoes a partial conversion to martensite. This increases that hardness again within the heat affected zone of FSP.

5.3.3 Tensile Test

Fig. 5.10 shows the true stress versus true strain curves for substrate, DMD and FSP 4340 steel specimens. Table 5.2 lists the numerical values of the yield strength, tensile strength and ductility under three different processing conditions. It can be seen that the Yield Strength and the UTS of substrate 4340 steel is much less than the DMD 4340 steel whereas the ductility is much greater. This is expected because of the martensitic structure of the DMD. The Yield Strength and the UTS of FSP 4340 steel is somewhat less than that of DMD 4340 steel. This can be attributed to the mixed microstructure of FSP which makes it softer and more ductile compared to the DMD.

5.3.4 Corrosion Test

Table 5.3 shows the results of the corrosion test data for 4340 steel. It can be seen that within the limits of experimental error, the corrosion rates of substrate, DMD and FSP 4340 steel are similar. After the exposure all the specimens developed reddish-orange deposits which are possibly ferrous and ferric hydroxides. In addition the corrosion appears to be uniform over the sample surface. It appears that the various processing and heat treatments described in this chapter do not alter the corrosion rate in any significant way. However 4340 steel is known to

undergo other forms of corrosion, namely, stress corrosion cracking, tempered martensite embrittlement and hydrogen embrittlement etc. The propensity towards these forms of failure is not evaluated in a typical immersion test.

5.4 Summary

In this study flame-treatment followed by FSP of a DMD 4340 steel-part was carried out with the objective of damage repair. As-deposited DMD 4340 steel had martesite-bainite microstructure whereas substrate 4340 steel had ferrite-pearlite microstructure. Upon flame treatment a gradient in microstructure developed within DMD deposit. The top layer of flame-treated DMD developed a microstructure consisting of bainite, ferrite and ferrite-carbide aggregate whereas the layers below it retained martensite-bainite morphology albeit with varying degrees of tempering. After FSP the top layer again developed martensite microstructure. FSP improved the ductility of DMD 4340 steel at the expense of reduced strength. Visual examination and weight loss measurements revealed no significant difference in corrosion rates of DMD, flame-treated and FSP 4340 steel upon immersion in synthetic seawater.

5.5 Acknowledgement

This work was supported by Focus:Hope and ONR. TEM investigation was carried out by Dr. Sudip Bhattacharya.

5.6 References

[1] AMPTIAC Quarterly, 8(3) (2004), *www.ammtiac.alionscience.com/pdf/AMPQ8_3.pdf*

[2] J. Wang, S. Prakash, Y. Joshi, and F. Liou, *Proc. Thirteenth Annual Solid Freeform Fabrication Symposium,* Austin, TX, August 5-7, (2002).

[3] T.W. Skszek and M.T.J. Lowney, *Die reconfiguration and restoration using laser-based deposition, in: Solid Freeform Fabrication Proceedings,* Austin, TX. (2000) 219.

[4] K.H. Richter, S. Orban and S. Nowotny, *Proc. 23rd International Congress Applications Lasers and Electro-Optics*, (2004).

[5] J. Choi and Y. Chang, *Intl. J. of Machine Tools Manuf.* 45 (2005) 597.

[6] Y.S. Tian, C.Z. Chen, S.T. Li and Q.H. Huo, *Appl. Surf. Sci.*, 242 (2005) 177.

[7] A.H. Nickel, D.M. Barnett and F.B. Prinz, *Mater. Sci. Eng. A*, 317 (2001) 59.

[8] C.T. Kwok, S.L. Fong, F.T. Cheng and H.C. Man, *J. Mater. Proc. Tech.*, 176 (2006), 168.

[9] M.D. Fuller, S. Swaminathan, A.P. Zhilyaev and T.R. McNelley, *Mater. Sci. Eng.* A 463 (2007) 128.

[10] R.S. Mishra and Z.Y. Ma, *Mat. Sci. Engg.* R 50 (2005) 1.

[11] W.D. Callister, *Materials Science and Engineering-an Introduction*, Fig. 10.23.

[12] P.J. Konkol, J.A. Mathers, R. Johnson and J.R. Pickens, *J. Ship Production* 19(3) (2003) 159.

[13] T.J. Lienert, W.L. Stellwag, B.B. Grimmett and R.W. Warke, *Weld. J. Res. Suppl.* 82 (2003) 1s

	C	Cr	Mn	Mo	Ni	O	Si	Fe
DMD	0.38	1.2	0.37	0.59	2.9	0.066	0.072	Balance
SUBSTRATE	0.40	0.99	0.76	0.26	1.68	0.0053	0.26	Balance

Table 5.1: Chemical Composition (Wt %) of DMD and Substrate 4340 steel.

	0.2% Yield Strength (MPa)	UTS (MPa)	Ductility (% Elongation)
Substrate 4340 steel	285	601	34.7
As-Deposited DMD 4340 steel	1189	1627	3.3
FSP 4340 steel	917	1180	9.5

Table 5.2: Mechanical Property Data of 4340 steel under various processing conditions.

.

Sample	Corrosion Rate (μm/yr)
Substrate	51
As-deposited DMD	53
FSP	53
Substrate + DMD	64
Substrate + FSP	45

Table 5.3: Corrosion Rates of 4340 steel under various processing conditions.

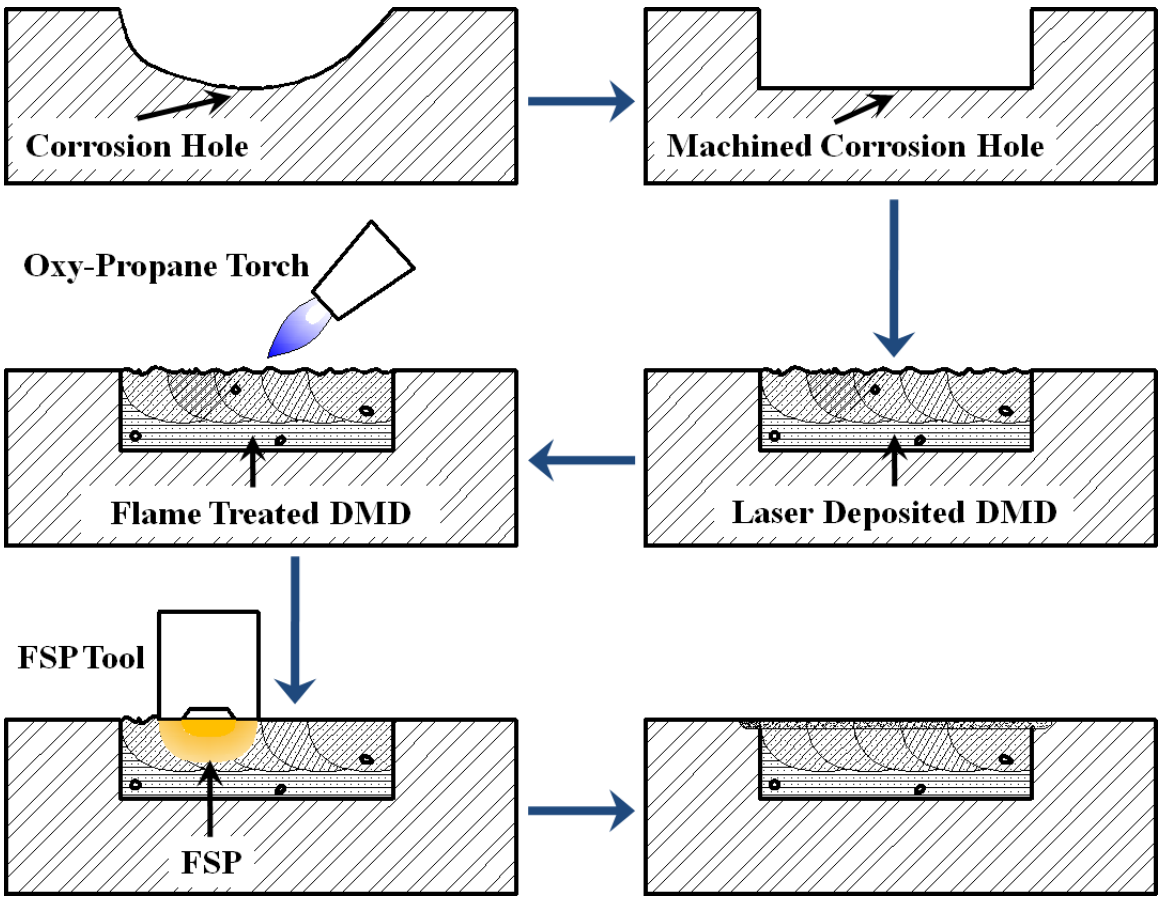

Fig. 5.1 Methodology of repair of 4340 steel using DMD and FSP. First the corrosion hole is machined to a regular shape. This is followed by laser deposition and flame-treatment of the deposit. Then FSP is carried out on the DMD which is finally ground to desired surface finish.

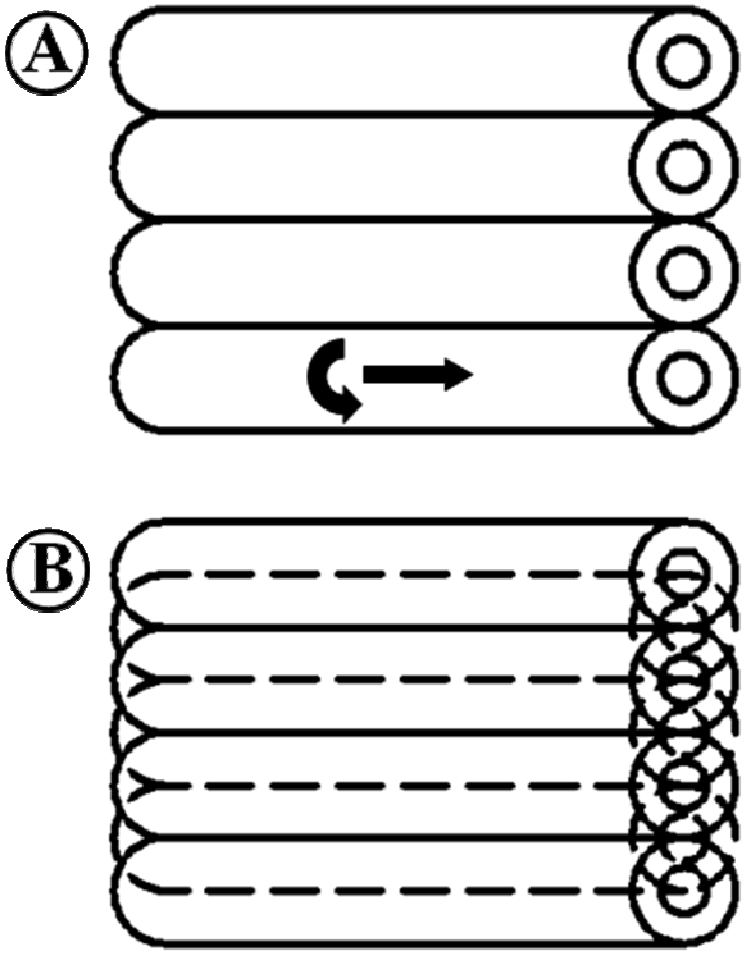

Fig. 5.2 (A) Four FSP passes with no overlap. (B) Seven FSP passes with 50% overlap. The second set of FSP passes are shown in broken outline.

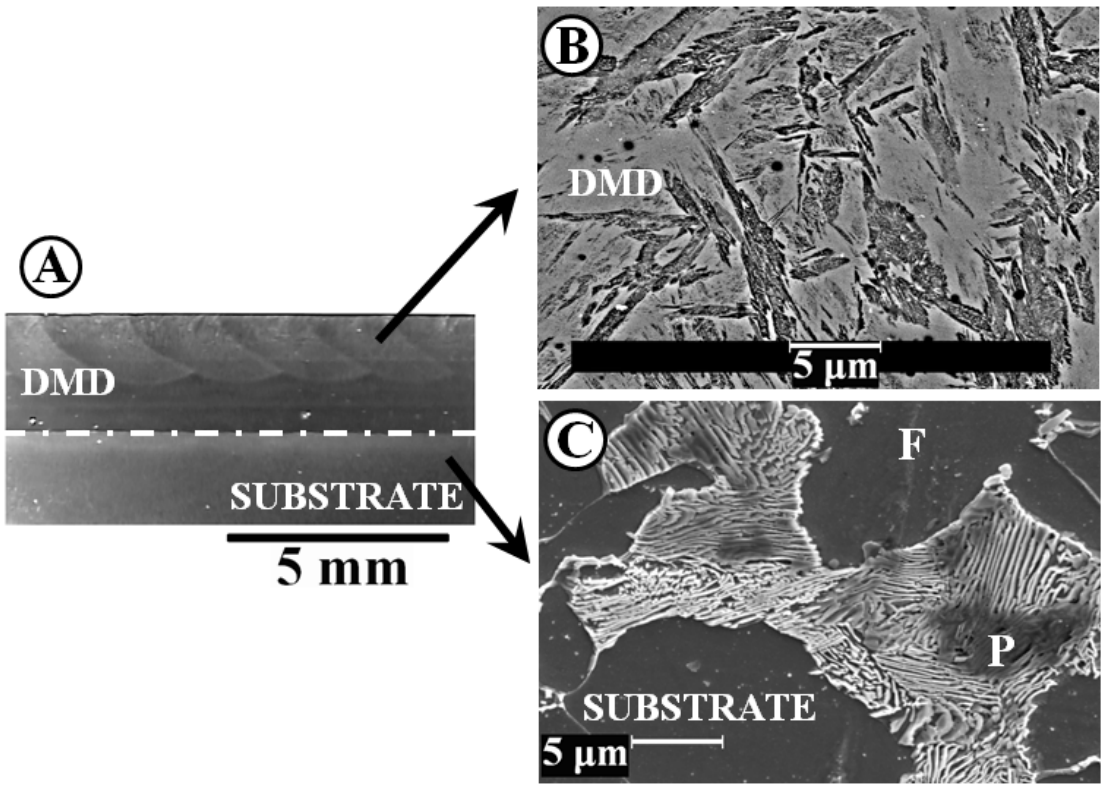

Fig. 5.3 (A) As-received DMD 4340 steel on 4340 steel substrate. (B) DMD with the martensite and bainite morphology. (C) Ferrite and pearlite morphology of substrate.

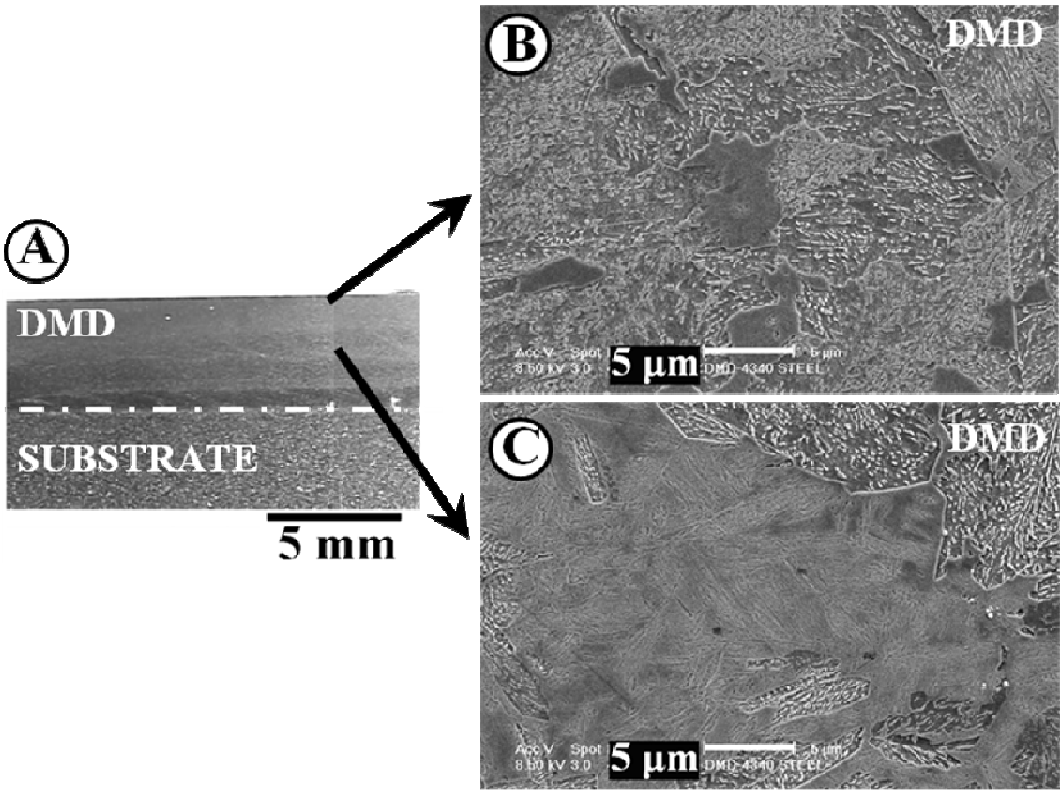

Fig. 5.4 (A) Flame softened DMD 4340 steel on 4340 steel substrate. (B) A mixed microstructure of bainite, ferrite and ferrite-carbide aggregate at the top of DMD layer. (C) Martensite and bainite at mid-depth of DMD layer.

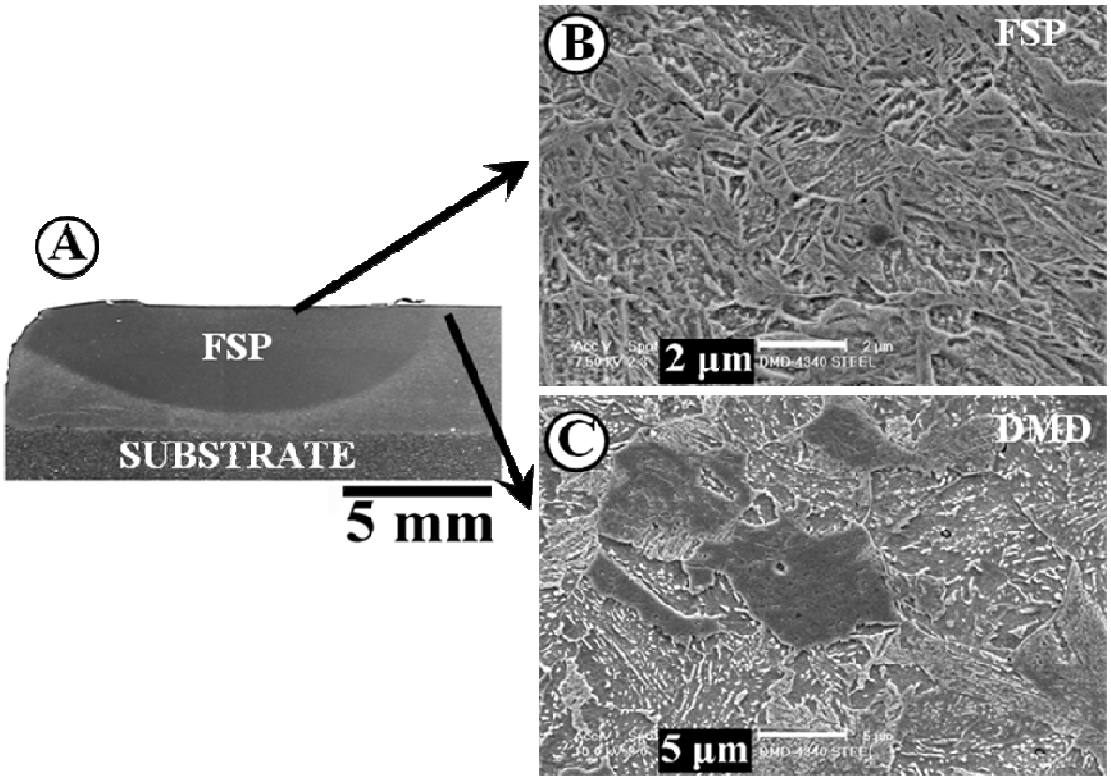

Fig. 5.5 (A) Macro-Image of FSP 4340 steel on 4340 steel substrate. (B) Martensitic morphology at the top of the process zone in FSP 4340 steel. (C) Bainite, ferrite and ferrite-carbide aggregate outside FSP process zone.

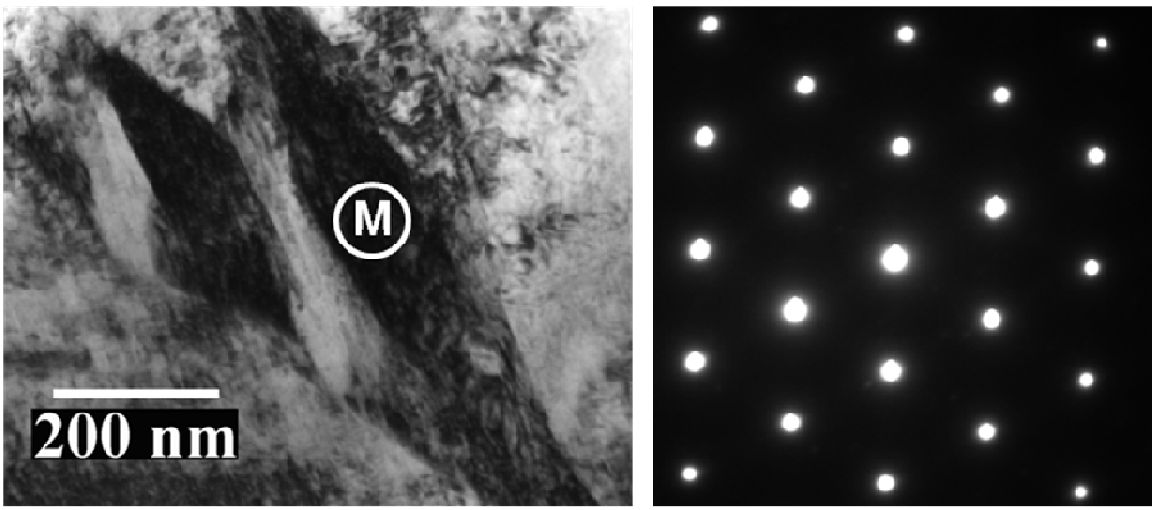

Fig. 5.6 (Left) Martensite needles within FSP process zone. (Right) Selected area diffraction pattern from region marked “M” within a martensite needle. The selected area diffraction pattern corresponds to BCT structure. Zone axis [-111].

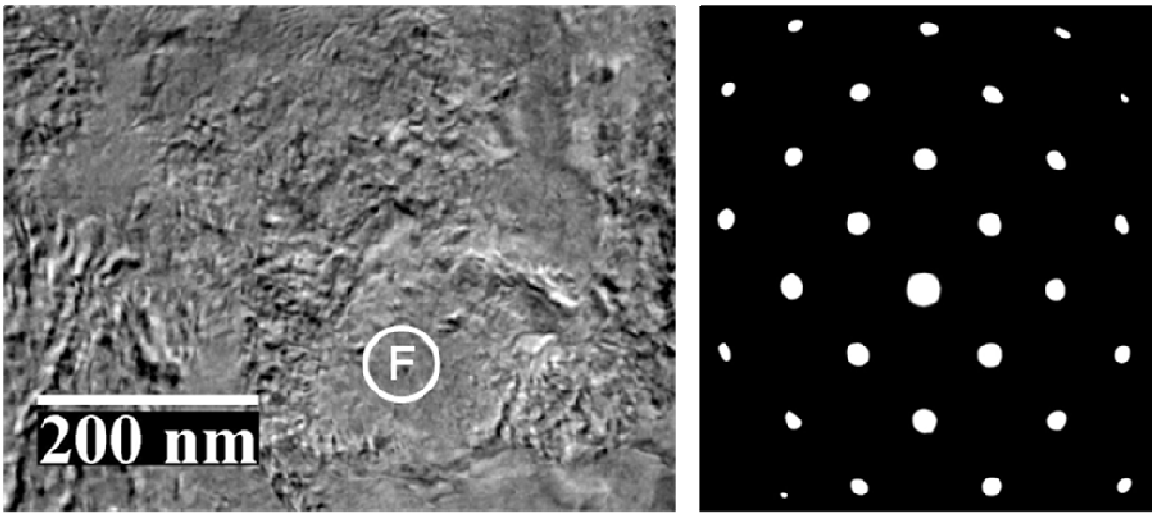

Fig. 5.7 (Left) Ferrite grains within the FSP process zone. (Right) Selected area diffraction pattern from region marked “F”. The selected area diffraction pattern corresponds to BCC structure. Zone axis [0 0 1].

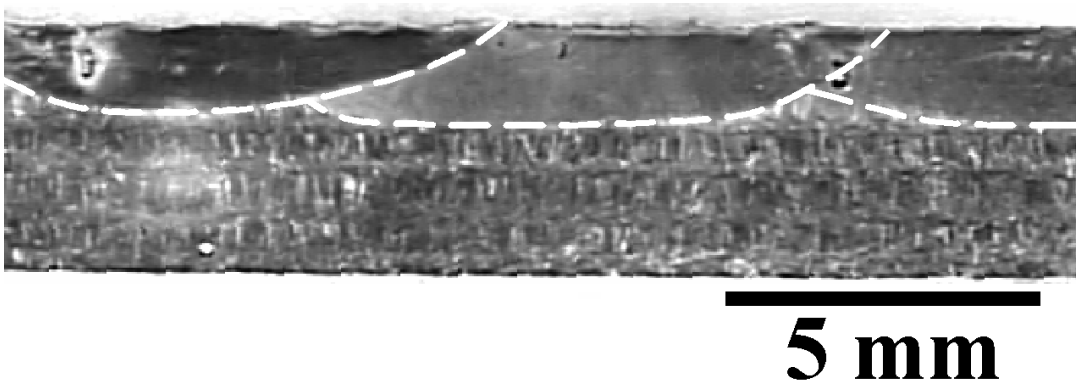

Fig. 5.8 Three overlapping FSP passes are shown. Process zone for each pass is outlined.

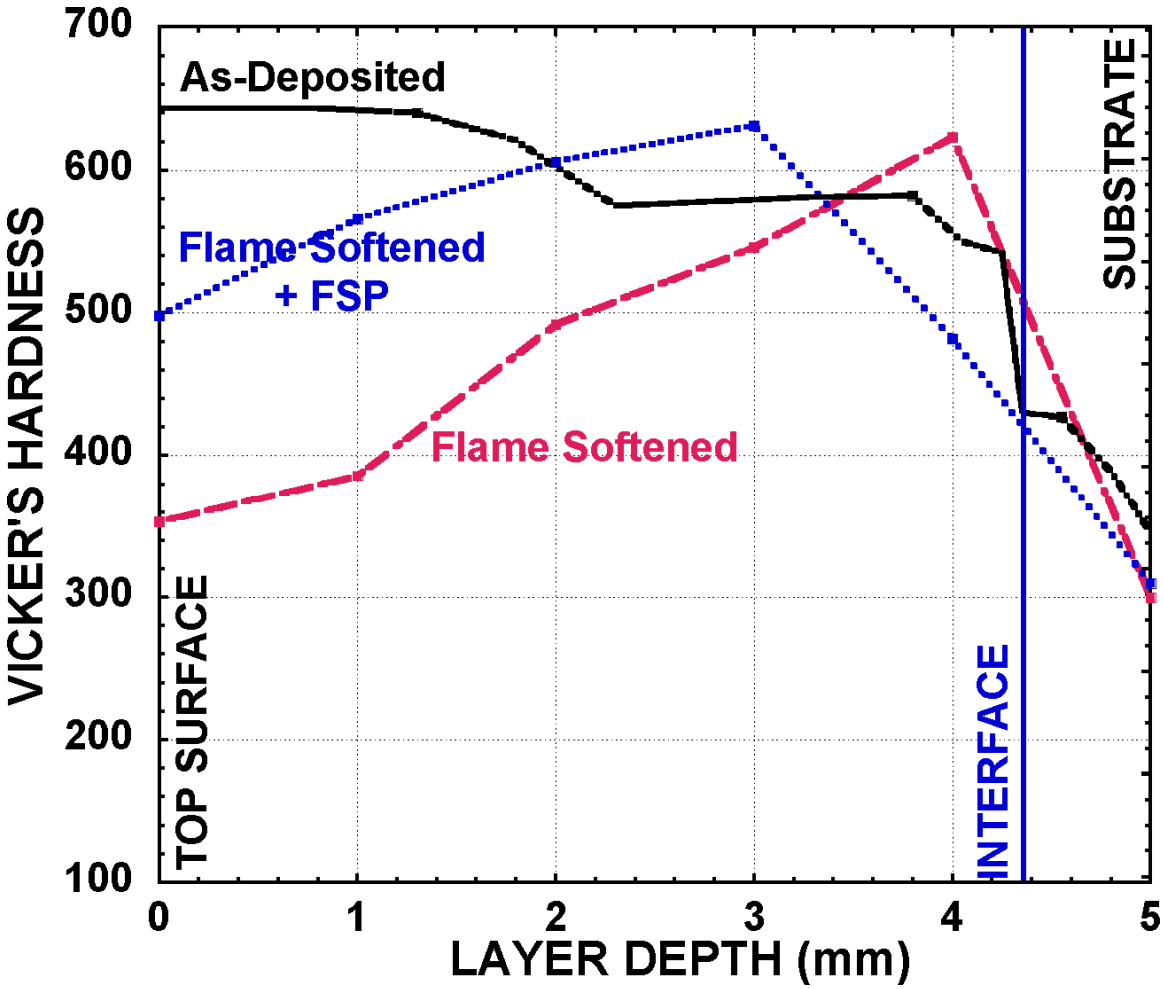

Fig. 5.9 Variation of hardness of deposited 4340 steel layer as a function of depth. Three different processing conditions are shown, namely, as-deposited, flame-softened and flame-softened followed by FSP.

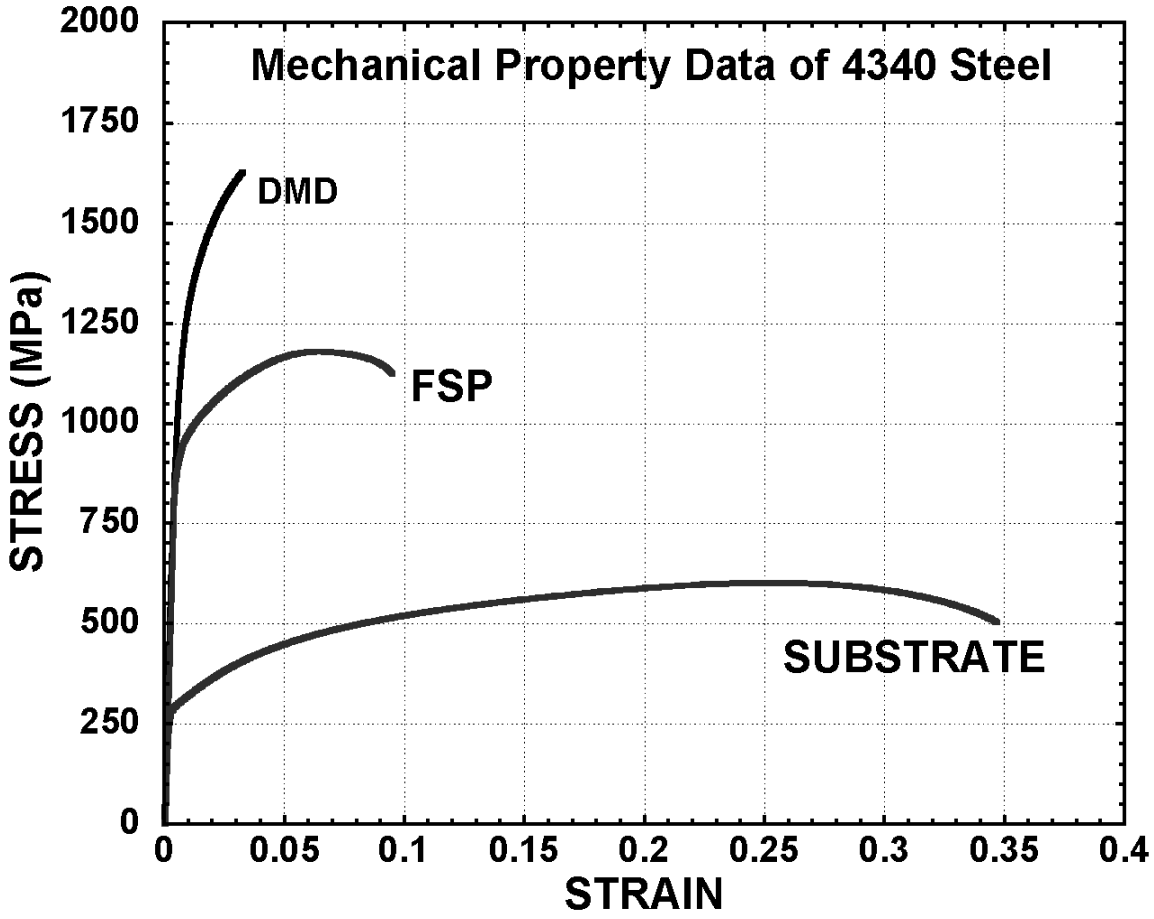

Fig. 5.10 Stress vs. strain curves of 4340 steel under three different processing conditions, namely, as-deposited, flame-softened and flame-softened followed by FSP.

Chapter 6

Friction Stir Processing of Direct Metal Deposited Copper-Nickel 70/30 – a Novel Technique of Damage Repair

Abstract

A combination of laser-assisted Direct Metal Deposition (DMD) and Friction Stir Processing (FSP) was used to explore techniques of repair of a Cu-Ni 70/30 part which underwent seawater corrosion and erosion. FSP of DMD-deposited Cu-Ni 70/30 is the subject of this research. A technique of processing a large area by overlapping individual FSP passes is described. Microstructural characterization was performed after every processing step and was related to the mechanical property. Corrosion behavior was also evaluated before and after FSP. It was observed that FSP reduced porosity, refined grains, reduced ductility and increased corrosion rate in Cu-Ni 70/30.

6.1 Introduction

Many navy weapons systems and support equipments are complex and expensive components which are subjected to constant wear and corrosion. Replacement of old parts and procurement of new ones which are low in quantity but high in value can be difficult and costly [1]. For this reason, research regarding repair and restoration of

existing components is extremely important. Towards that end laser-assisted DMD has already been employed to repair turbine blades, torpedo shells, tools, dies etc [2-4]. However DMD process is often limited by porosity [5], cracking [6], residual stress [7], and solute segregation [8] in the deposit which adversely affect mechanical integrity and/or corrosion resistance. Some of these limitations can be overcome by surface modification of DMD deposit via friction stir processing. FSP has been employed to reduce porosity in cast alloys and refine microstructure in wrought alloys including 304L stainless steel, aluminum and copper [9, 10]. Thus a combination of DMD followed by FSP can be used to produce superior quality of repair, but such an idea has hardly been explored.

In this chapter the effects of FSP on a sample of DMD Cu-Ni 70/30 was investigated. Copper-nickel alloys find widespread use in marine environment due to their excellent corrosion resistance [11]. The objective of this work is to repair a certain Cu-Ni 70/30 part which pumps large amount of seawater thus undergoing corrosion and erosion. The repair process was kept “local”, namely, the processing involved in the repair region did not influence the structure and properties of other regions of the part. This made FSP an ideal technique for local repair. The part under investigation was exposed to seawater and underwent loading. In view of that particular attention was given to mechanical integrity and corrosion resistance of repair.

6.2 Experimental

The overall methodology of repair using DMD and FSP is described in Fig. 6.1. The marine component to be repaired had a corrosion hole which was machined to a regular

shape. In certain situations this may mean removal of an entire layer of material containing the corrosion hole. The machined hole was filled with DMD deposit which subsequently underwent FSP. The final surface finish was obtained by machining. The scope of this investigation was limited to the processing of as-deposited Cu-Ni 70/30 layer on a Cu-Ni 70/30 substrate, supplied by POM Group Inc., Auburn Hills, Michigan, USA. The substrate dimension was 125mm × 101.6mm × 12.7mm and the DMD layer dimension was 102.5mm × 101.6mm × 3.13mm. The chemical composition of typical Cu-Ni 70/30 alloy is listed in Table 6.1 [12]. Small amounts of iron and manganese are added to improve corrosion resistance in high-velocity (from 1.5-4.5 m/sec) water including seawater.

FSP of Cu-Ni 70/30 was performed using a tungsten alloy tool with scrolled shoulder and scrolled pin as shown in Fig. 6.2B and Fig. 6.2C. The tool material was tungsten-25% rhenium with hafnium carbide particles distributed in the metal matrix. The alloy has high melting point (3120°C) and a low ductile-brittle transition temperature [13, 14] which makes it an ideal candidate for FSP tool material. Fig. 6.2A shows the schematic of overall tool design. The H13 shaft had a channel for the water to flow through. It also had threads towards the end which houses the H13 collar and a semicircular key. The H13 collar locked tungsten-rhenium piece into position and the key transmitted the torque. All the H13 pieces were heat treated to high hardness (Rockwell C 55). A separate two-piece cooling block which was made of 303 stainless steel made an important part of the water cooling system. The cooling block was mounted from the head of the milling machine using a separate fixture not shown here. Copper tubes, which were joined to the cooling block by silver-brazing, made the inlet and outlet. The cooling

block was made leak-proof by using o-rings. The cooling block served to prevent overheating of the tool. It was observed that without cooling the key driving the tungsten piece sheared off, causing friction and wear in the conical surfaces of the H13 collar.

FSP was carried out at a tool rotation rate of 1200rpm counterclockwise. Three different feed rates, namely, 12.7mm/min, 25.4mm/min and 50.8mm/min were used. The tool was tilted 3° towards the backside with respect to the surface normal during FSP. The counterclockwise rotation of the tool and the orientation of scrolls on shoulder and pin are such that the plasticized material under the shoulder is collected and transported to the base of the pin and further to the tip of the pin. Material flow such as this creates defect-free stir zone. Other parameters of importance during FSP is the dwell time and contact load. It was observed that without a significant dwell period of 4min-5min, the process zone did not get hot enough which resulted in groove-type defect in the stir zone accompanied by chipping and fragmentation of processed material. It is also important to maintain a uniform contact load during the process. The traditional way of doing FSP wherein a uniform plunge depth is maintained, results in an overheated process zone accompanied by large amount of flash.

Cu-Ni 70/30 samples were etched using a combination of 16g chromium tri-oxide (CrO_3), 1.8g ammonium chloride (NH_4Cl), 10mL nitric acid (HNO_3), and 200mL water (H_2O) [15]. The etchant preferentially attacks copper-rich phases [15]. Scanning electron microscopy was used to analyze the microstructure of Cu-Ni 70/30 samples before and after FSP. Energy dispersive spectroscopy was used to measure compositional variations among various regions. Vickers microhardness was measured in various regions and was related to the microstructure.

Repair of a large area requires multiple overlapping FSP passes. Overlap was done with FSP passes running parallel to each other in the same direction with an offset of 1.5mm between successive passes. The offset was such that the advancing side of one pass was overlapped by the retreating side of the next pass. This was done so because defects generally arise at the advancing side. Using the scheme an area large enough to prepare tensile and corrosion test specimens was processed.

Corrosion test specimens were extracted from substrate, DMD and FSP Cu-Ni 70/30 samples. All corrosion test specimens were sent to Corrosion Testing Laboratories Inc., Newark, Delaware, USA. The specimens were rectangular in shape of dimension 50.8mm × 25.4mm × 3.3mm. The specimens had a 3.2mm diameter through-hole at one side to keep it suspended using a string. The corrosion rate was determined by exposing the specimens to synthetic seawater at laboratory ambient temperature (20°C) for 30 days as per ASTM-G31 standard. The test solution was prepared from commercially available synthetic seawater salt (Lake Products, Maryland Heights, Missouri, USA) that met ASTM D1141 standard. The salts were dissolved in de-ionized water to prepare the final test solution which had a pH of 8.2. A poly-tetra-fluoro-ethylene string was used to keep the test specimens suspended and totally immersed in the test solution. The test vessel was sealed off for the remainder of duration of the test. After 30 days of exposure the test specimens were removed, cleaned, reweighed and visually evaluated.

Tensile test specimens were extracted from DMD and FSP Cu-Ni 70/30 samples and were tested in-house. The specimen had a gage length of 15.2mm, a gage width of 6.5mm and a gage thickness of 3.3mm. It also had a shoulder region of radius 6.35mm and a grip section of length 15.5mm on both sides. For the FSP sample the longitudinal axis of the

tensile test specimen was perpendicular to the FSP pass direction. Room temperature tensile tests were performed at a constant crosshead speed of 0.5mm/min.

6.3 Results and Discussion

Fig. 6.3A shows a macro-image of as-deposited DMD and substrate Cu-Ni 70/30. Fig. 6.3B and 6.3C show the microstructure of as-deposited DMD at different magnifications. Fig. 6.3D shows the microstructure of substrate Cu-Ni 70/30. The substrate grains are elongated which is typical of rolled microstructure. The length of the DMD dendrites is between 30-60μm and the width is between 4-15μm. The dendrites are at various angles with respect to plate normal. The growth direction of dendrites is related to the local heat-flux direction during DMD [16]. As shown in Fig. 6.3C the primary dendrite arm spacing is ~5.7μm and the secondary dendrite arm spacing is ~2.8μm.

6.3.1 Electron Microscopy of Single FSP Pass

Figure 6.4 shows a top view of FSP of Cu-Ni 70/30 alloy under three different conditions, namely, a rotation rate of 1200 RPM and feed rates of 12.7mm/min, 25.4mm/min and 50.8mm/min. The stir zone appears defect-free from the surface. Figure 6.5 shows the cross sectional image of the FSP nugget for 1200 RPM, 12.7mm/min. Figure 6.6 shows a similar cross sectional image for 1200 RPM, 25.4mm/min. Material flow in the nugget is complex. Vertical mixing of material can be seen from the counterclockwise circulation of material indicated by arrows although the extent of circulation is different for two conditions. Also onion ring like structure is seen in some portion of the nugget. Figure 6.7 shows a magnified portion of Figure 6.5 which lies at

the advancing side of the pin down below. Substrate grains at the side of the pin are pushed upwards and substrate grains at the bottom of the pin are pushed downwards. One interesting observation from Fig. 6.5 and Fig. 6.6 is that porosity in the FSP nugget region is much less than that in the unprocessed DMD. In fact the unprocessed DMD contains large pores along the layer immediately above the interface. In order to ensure that porosity is consistently less everywhere within the FSP stir zone, a longitudinal section of the nugget parallel to the tool motion is taken. Figure 6.8A shows the longitudinal section, where no large pore comparable to that in DMD is seen. Fig. 6.8B shows the equiaxed nugget grain structure (average grain size ~ 2.5μm) which is typical of FSP. The long dendrites within the DMD transforms to a much finer equiaxed grain structure due to dynamic recrystallization. The change in porosity as a result of FSP is also measured. The DMD Cu-Ni 70/30 sample has two DMD layers. The layer adjacent to the substrate (i.e. the 1^{st} layer) has more porosity (3.3%) than the 2^{nd} layer (1.3%) which is the top DMD layer. Porosity in the FSP nugget zone is the least (0.35%). The comparison of porosity between the two layers is shown in Figure 6.9. The average pore size in 1^{st} DMD layer is 62μm, which for the 2^{nd} layer is 38μm and for the FSP zone it is 7μm. It appears that the forging and stirring action during FSP at elevated temperature close up the pores.

A portion of the nugget zone shows onion ring structure which is shown in Figure 6.10. The dark contrast appears because of the fine grained structures with a grain size of 1μm and the light contrast appears because of the coarse grained structure with a grain size of 2.5μm. The banded structure is a result of different grain sizes.

Figure 6.11 shows an energy dispersive spectroscopy analysis of DMD and FSP regions. The dendritic regions have a copper content of ≈ 63% whereas the inter-dendritic regions have a copper content of ≈ 71%. After FSP the grain structure becomes equiaxed and the constituents are more homogeneously distributed. After FSP the equiaxed grains and the grain boundary regions have a copper content of ≈ 67%. The homogenization of elemental composition in the nugget zone occurs because DMD dendrites are broken down and recrystallized during FSP.

6.3.2 Hardness

Figure 6.12 shows the hardness profile across FSP nugget of Cu-Ni 70/30 alloy for three different processing conditions. The hardness profile is measured along a line which is 2mm below the top surface. No dependence of hardness on feed-rate is observed. However hardness is consistently higher in the nugget region (~145 HV) due to the finer grain size. Also the gradient of hardness with respect to distance is more at the advancing side than at the retreating side. Advancing side of the FSP pin generally sees a higher velocity gradient and hence a higher strain gradient [16] which results in a higher hardness gradient.

6.3.3 Electron Microscopy of Overlapping FSP Passes

Figure 6.13A shows a schematic of seven overlapping FSP passes. Successive FSP passes move from left to right in the figure so that the advancing side of one pass is overlapped by the retreating side of the next pass. Fig. 6.13B shows the top view and 6.13C shows the front view of overlapping passes. As observed before DMD has large porosity which

is substantially reduced by FSP. There are regions of light and dark contrast within the process zone which is due to variations of grain size. The top view in Fig. 6.3B shows very fine cracks running parallel to the FSP passes at locations where two passes overlap. Other regions of the process zone show the characteristic onion ring patterns. One possible reason for cracking in overlap regions is that FSP stir zone has low ductility – so that when an already processed region undergoes further processing it cracks.

6.3.4 Tensile Test

Fig. 6.14 shows the true stress versus true strain curves for DMD and FSP Cu-Ni 70/30 specimens. Table 6.2 lists the numerical values of yield strength, tensile strength and ductility under two different processing conditions. FSP has much higher yield strength and slightly higher UTS and a lower ductility in comparison to DMD. This is explicable because FSP has fine equiaxed grain structure whereas DMD has long dendritic grain structure.

6.3.5 Corrosion Test

Table 6.3 shows the 30 day immersion test data for Cu-Ni 70/30 specimens under various processing conditions. Cu-Ni 70/30 has excellent corrosion resistance and its corrosion rates are much lower than that of 4340 steel which has a corrosion rate of the order of 50μm/yr (Table 5.3). DMD has higher corrosion rate than substrate Cu-Ni 70/30. Higher corrosion rate in DMD can be attributed to increased copper concentration along dendrite boundary whereby a galvanic couple is formed with dendrite interior where copper concentration is low. FSP homogenizes the elemental composition, so it might be

expected that FSP material will show lower corrosion rate. However FSP has still higher corrosion rate compared to DMD with preferential attack along overlap regions along weld passes. Earlier it was observed that cracks can form along overlap regions thereby increasing the surface area of corrosion attack. Another contributing factor is the grain boundary area. Grain boundaries being an area of lattice mismatch are susceptible to corrosion attack. Substrate Cu-Ni 70/30 has the least grain boundary area whereas FSP Cu-Ni 70/30 has the highest grain boundary area.

6.4 Conclusions

As-deposited DMD Cu-Ni 70/30 has dendritic solidification microstructure with the length of the dendrites between 30-60μm and the width between 4-15μm. After FSP, extensive recrystallization in the nugget region leads to finer and equiaxed grains of size 1-2.5μm. Porosity is observed in the as-deposited and FSP Cu-Ni 70/30 alloy. In the DMD layer adjacent to the substrate, porosity is ≈ 3.3%, in the next layer the porosity is ≈ 1.3%. Porosity in the FSP nugget is significantly reduced to ≈ 0.35%. Energy dispersive spectroscopy suggests a higher copper concentration along DMD dendrite boundaries. FSP homogenizes the elemental composition. Tensile and corrosion tests are carried out on DMD and FSP Cu-Ni 70/30 alloy. FSP Cu-Ni 70/30 has higher yield-strength, lower ductility and higher corrosion rate than DMD Cu-Ni 70/30.

6.5 References

[1] AMPTIAC Quarterly, 8(3) (2004), *www.ammtiac.alionscience.com/pdf/AMPQ8_3.pdf*

[2] J. Wang, S. Prakash, Y. Joshi, and F. Liou, *Proc. Thirteenth Annual Solid Freeform Fabrication Symposium,* Austin, TX, August 5-7, (2002).

[3] T.W. Skszek and M.T.J. Lowney, *Die reconfiguration and restoration using laser-based deposition, in: Solid Freeform Fabrication Proceedings,* Austin, TX. (2000) 219.

[4] K.H. Richter, S. Orban and S. Nowotny, *Proc. 23rd International Congress Applications Lasers and Electro-Optics*, (2004).

[5] J. Choi and Y. Chang, *Intl. J. of Machine Tools Manuf.* 45 (2005) 597.

[6] Y.S. Tian, C.Z. Chen, S.T. Li and Q.H. Huo, *Appl. Surf. Sci.*, 242 (2005) 177.

[7] A.H. Nickel, D.M. Barnett and F.B. Prinz, *Mater. Sci. Eng. A*, 317 (2001) 59.

[8] C.T. Kwok, S.L. Fong, F.T. Cheng and H.C. Man, *J. Mater. Proc. Tech.*, 176 (2006), 168.

[9] M.D. Fuller, S. Swaminathan, A.P. Zhilyaev and T.R. McNelley, *Mater. Sci. Eng.* A 463 (2007) 128.

[10] R.S. Mishra and Z.Y. Ma, *Mat. Sci. Engg.* R 50 (2005) 1.

[11] *ASM Handbook*, The American Society of Metals, Metals Park, OH, 13(B), (1995) 125

[12] *ASM Handbook*, The American Society of Metals, Metals Park, OH, 2, (1995)

[13] http://www.rhenium.com/tung_rhen.asp?menu_id=2&pic_id=9

[14] P.L. Raffo**,** *J. Less Common Metals* 17(2) (1969) 133

[15] *ASM Handbook*, The American Society of Metals, Metals Park, OH, 9, (2004) 775

[16] W. Kurz, C. Bezençon and M. Gäumann, *Sci. Tech. Adv. Mater.* 2 (2001) 185

[17] R. Nandan, G.G. Roy, T.J. Lienert and T. DebRoy, *Sci. Tech. Welding Joining.* 11(5) (2006) 526.

Pb	Fe	Zn	Mn	Ni	Other	Cu
0.05	0.4-0.7	1.0	1.0	29-33	0.5	Bal

Table 6.1: Composition in wt% of Cu-Ni 70/30 Alloy.

	0.2 % Yield Strength (MPa)	UTS (MPa)	Ductility
DMD Cu-Ni 70-30	187.1	339.4	13.8%
FSP Cu-Ni 70-30	325	350.2	1.2%

Table 6.2: Mechanical Property Data for Cu-Ni 70/30.

Sample	Corrosion Rate (μm/yr)
Cu-Ni 70/30 Substrate	2.0
DMD Cu-Ni 70-30	9.1
FSP Cu-Ni 70-30	12.7

Table 6.3: Corrosion Rates of Cu-Ni 70/30 under various processing conditions.

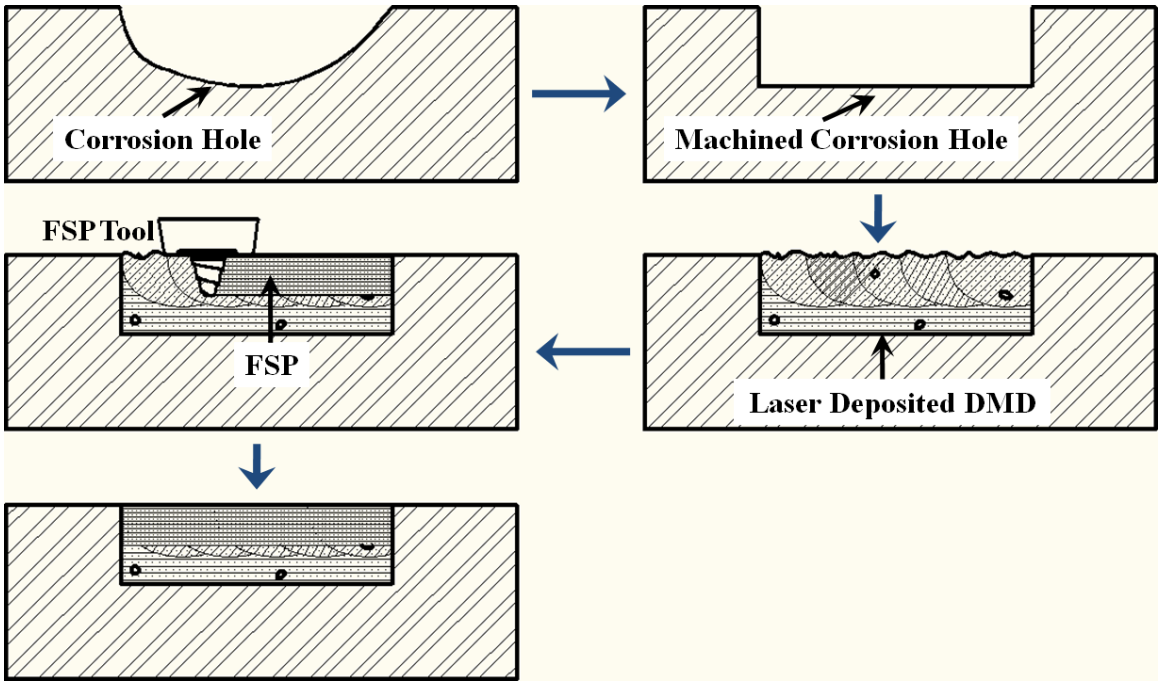

Fig. 6.1 Methodology of repair of Cu-Ni 70/30 using DMD and FSP. First the corrosion hole is machined to a regular shape. This is followed by laser deposition and FSP. The surface is finally machined to desired finish.

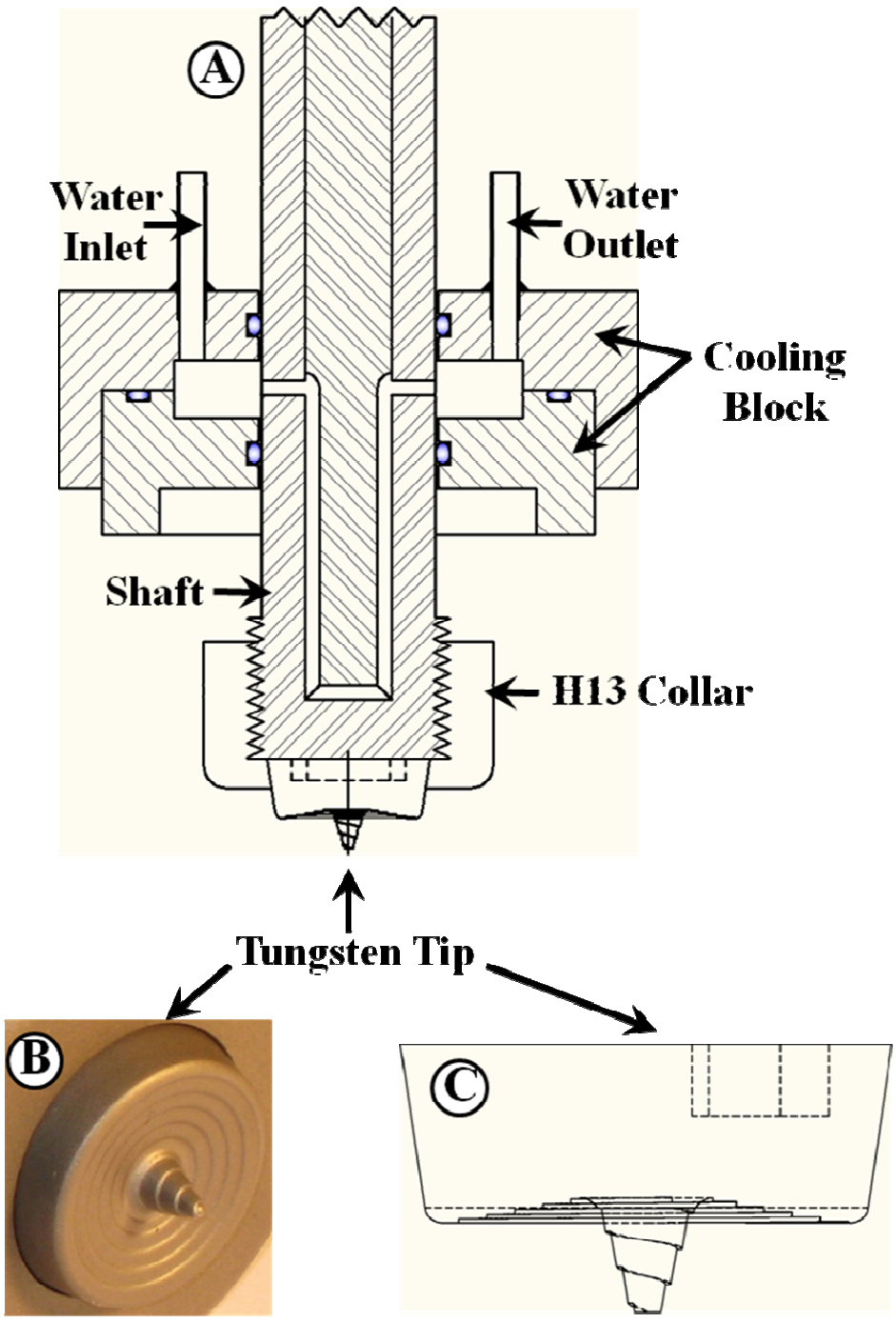

Fig 6.2 (A) Schematic design of FSP tool showing tungsten tip, H13 collar and shaft as well as cooling block. (B) Image of tungsten tool-tip. (C) Schematic of tungsten tip showing scroll in shoulder and pin.

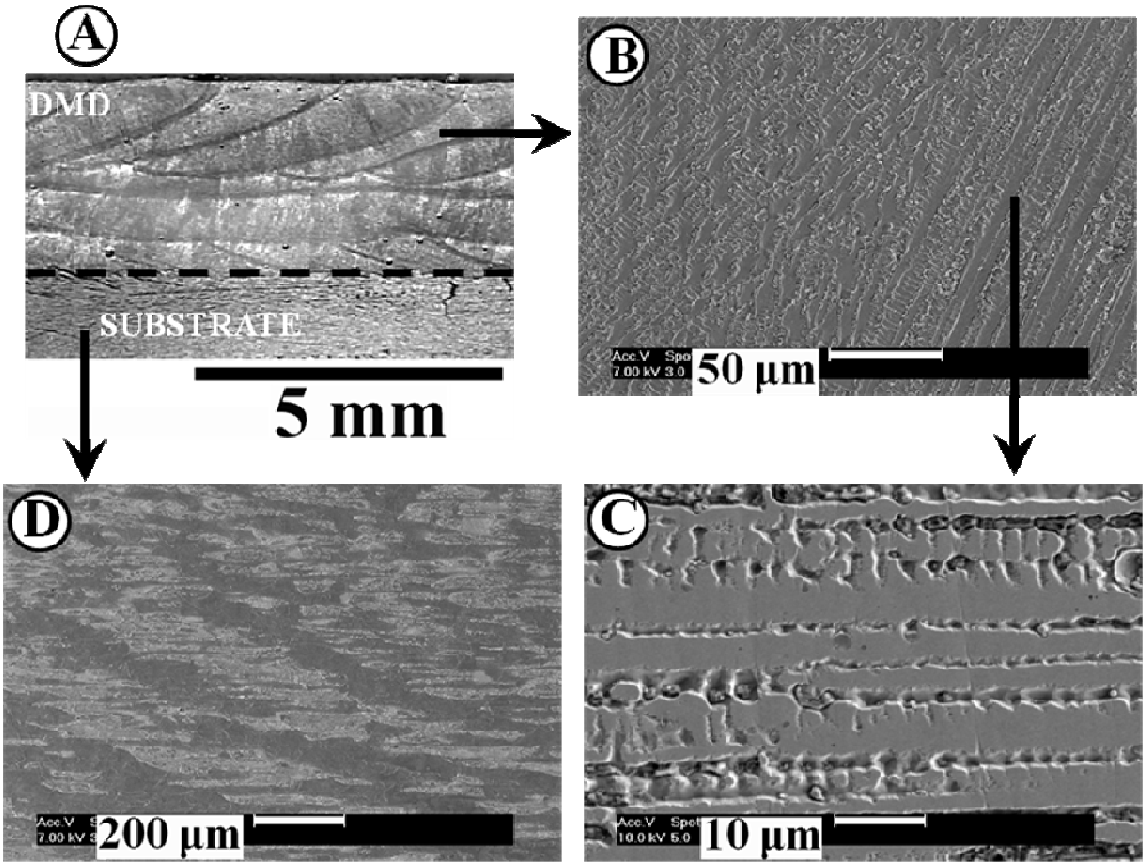

Fig 6.3 (A) Macro-image of DMD and substrate Cu-Ni 70/30 alloy. (B) A magnified view of DMD showing varying orientations of dendrites. (C) A magnified view of DMD showing primary and secondary dendrites. (D) elongated substrate grains.

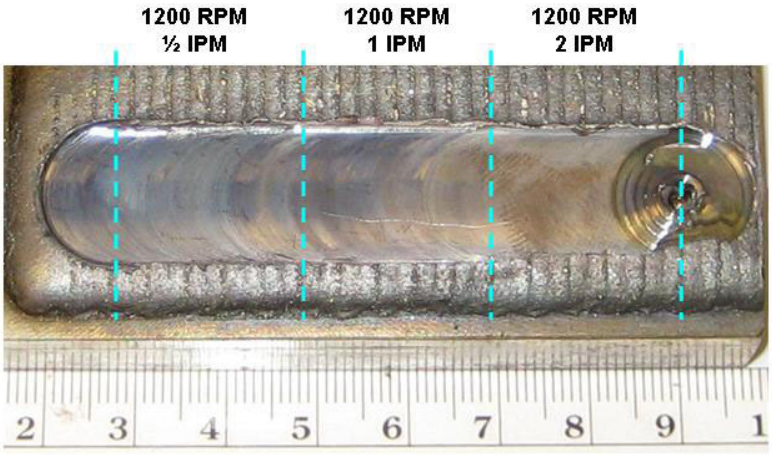

Fig 6.4: Macro-image of FSP of Cu-Ni 70/30 alloy.

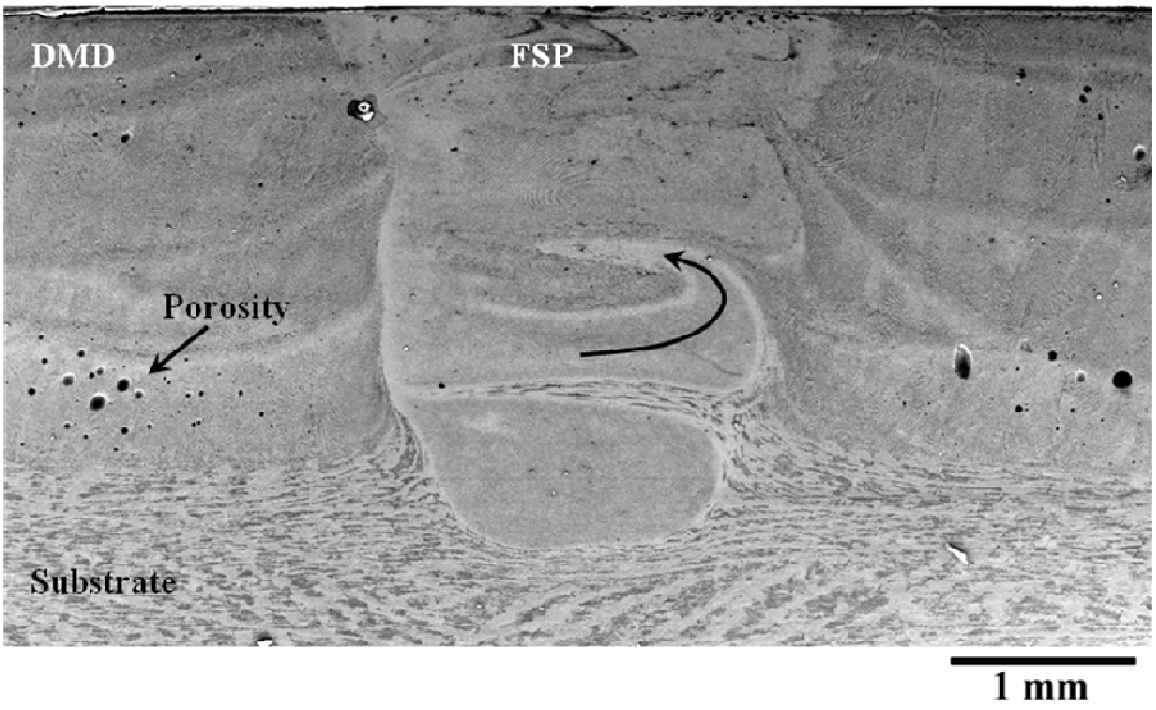

Fig 6.5 Cross-sectional image of FSP Nugget for 1200rpm, 12.7mm/min. Counterclockwise circulation of material is observed within the nugget.

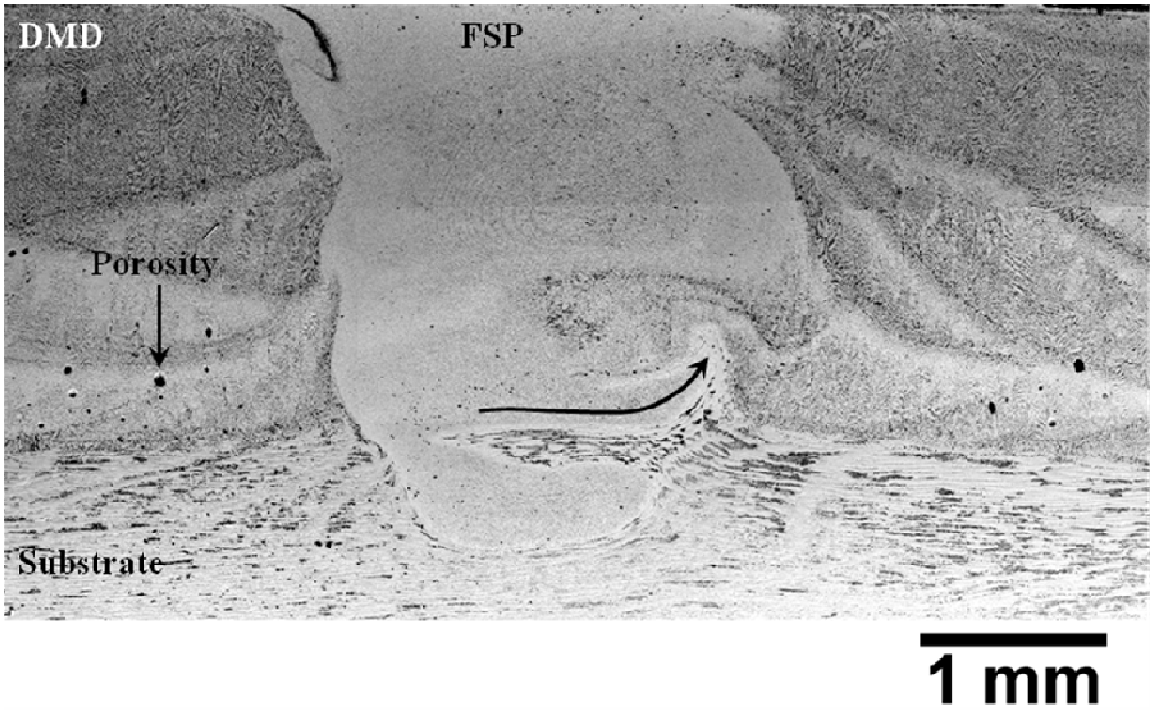

Fig 6.6 Cross-sectional image of FSP nugget for 1200rpm, 25.4mm/min. Counterclockwise circulation of material is observed within the nugget.

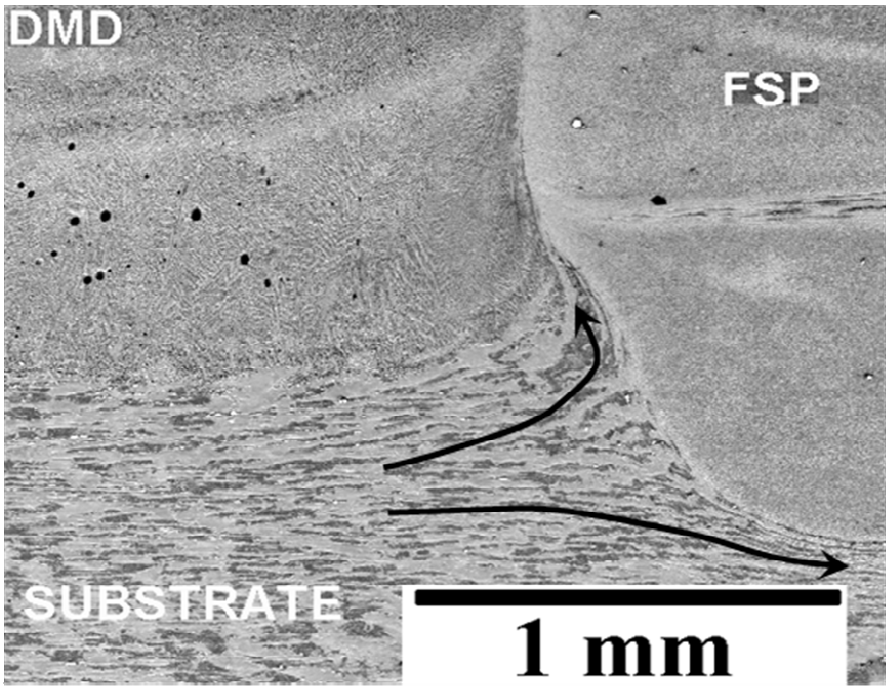

Fig 6.7 Cross-sectional image of FSP nugget for 1200rpm, 12.7mm/min. The material at the advancing side of the pin deforms and flows upwards. Material at the bottom of the pin is pushed downwards.

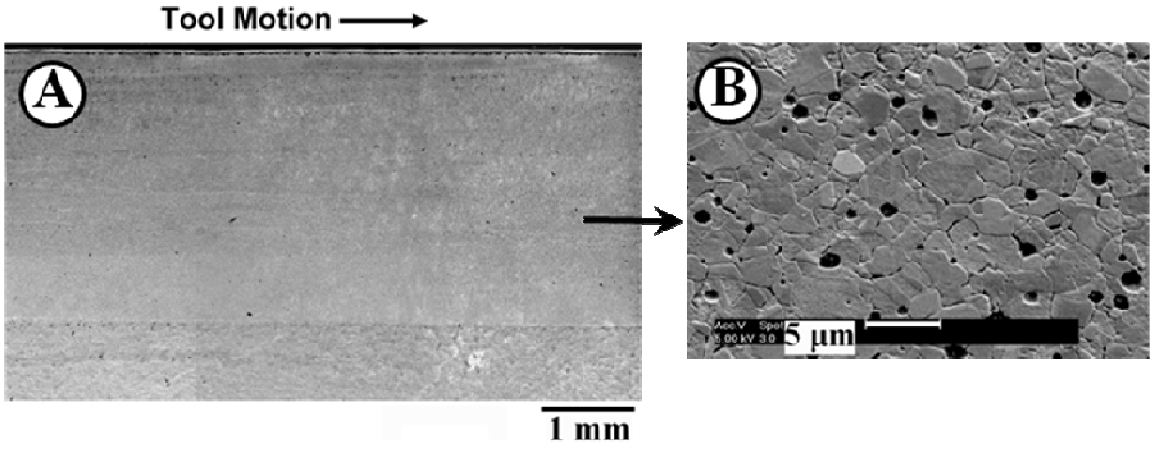

Fig 6.8 (A) Longitudinal-sectional image of FSP nugget for 1200rpm, 12.7mm/min. (B) Equiaxed grains in FSP nugget zone. The particles with black contrast are chromium-bearing etching products.

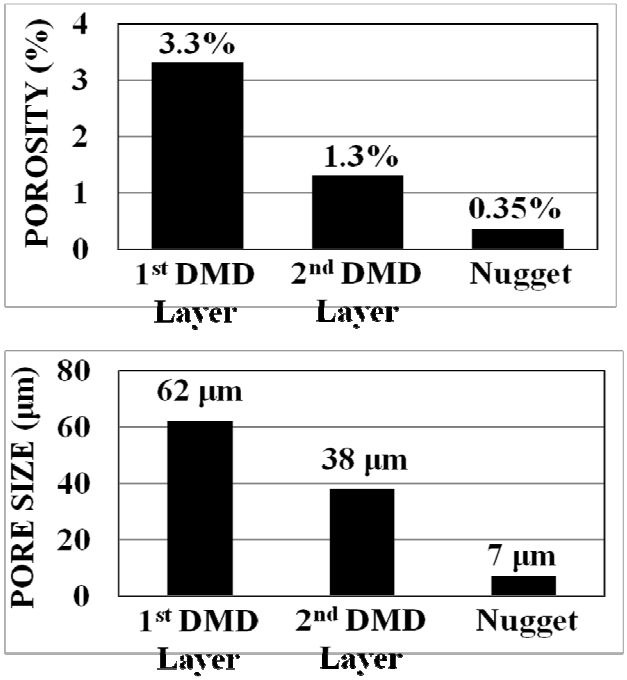

Fig 6.9 Comparison of porosity in the DMD and FSP Cu-Ni 70/30. 1st DMD layer is the layer adjacent to the substrate. 2nd DMD layer is the top layer.

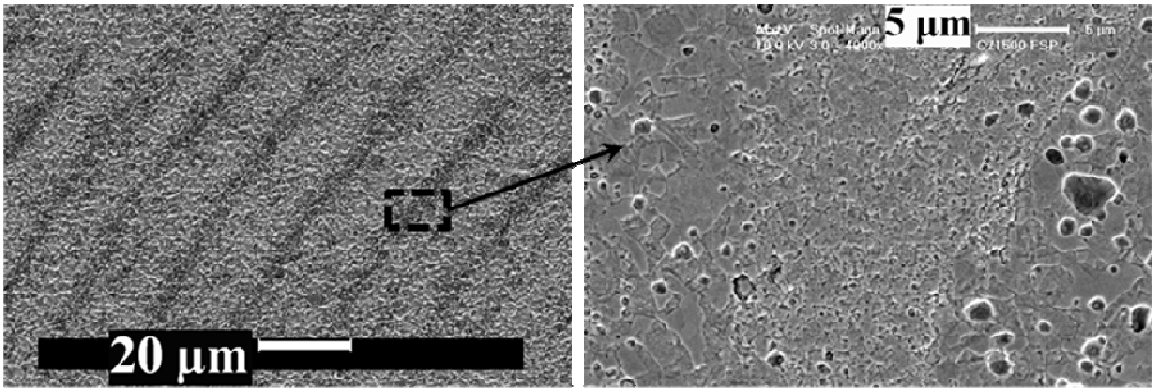

Fig 6.10 Onion ring structure in the nugget created by variation in grain size. Bands with dark contrast are fine-grained region (grain size ~1µm). Light contrast is the coarse-grained region (grain size ~2.5µm). The particles with black contrast are chromium-bearing etching products.

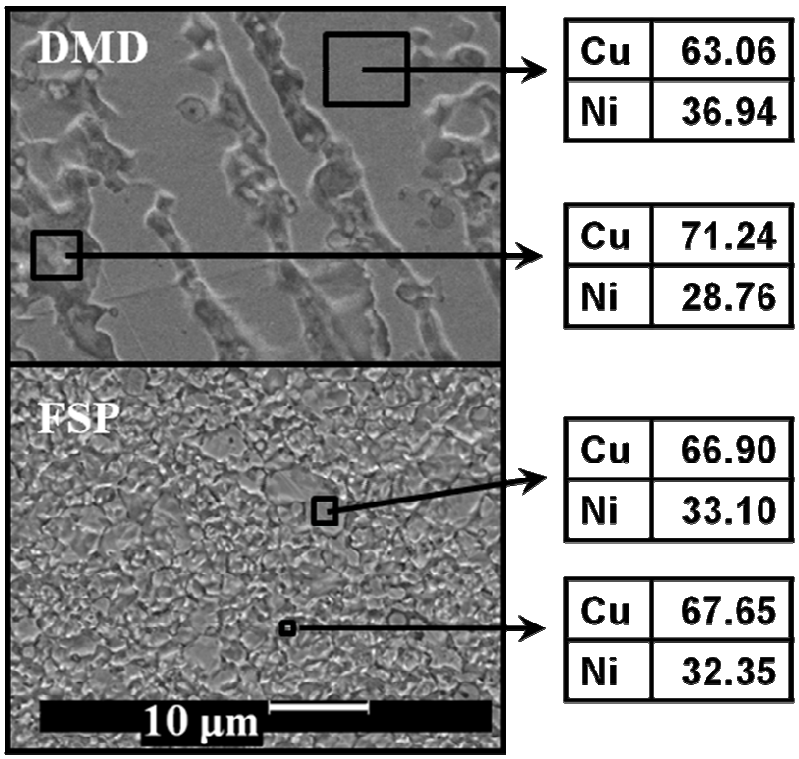

Fig 6.11 EDS analysis of DMD and FSP Cu-Ni 70/30 alloy. Copper and nickel weight percents are shown.

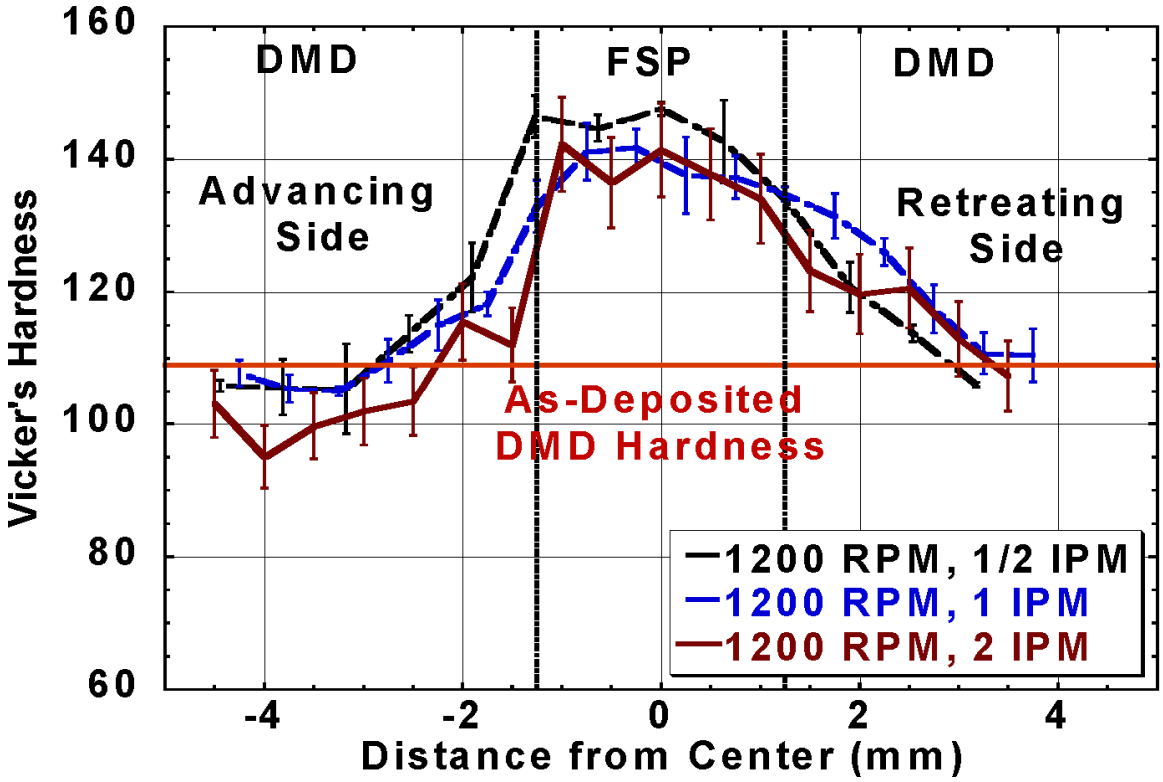

Fig 6.12 Hardness profile across FSP nugget of Cu-Ni 70/30.

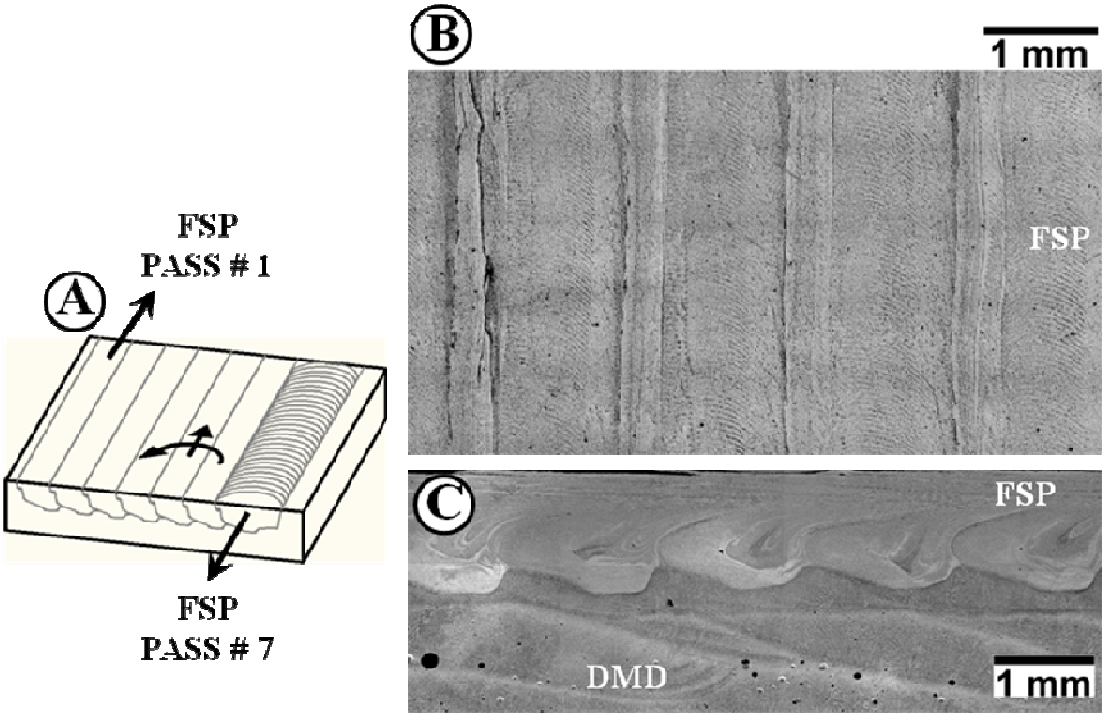

Fig 6.13 (A) Schematic of seven overlapping FSP passes (B) Top view of overlapping passes (C) Front view of overlapping FSP passes.

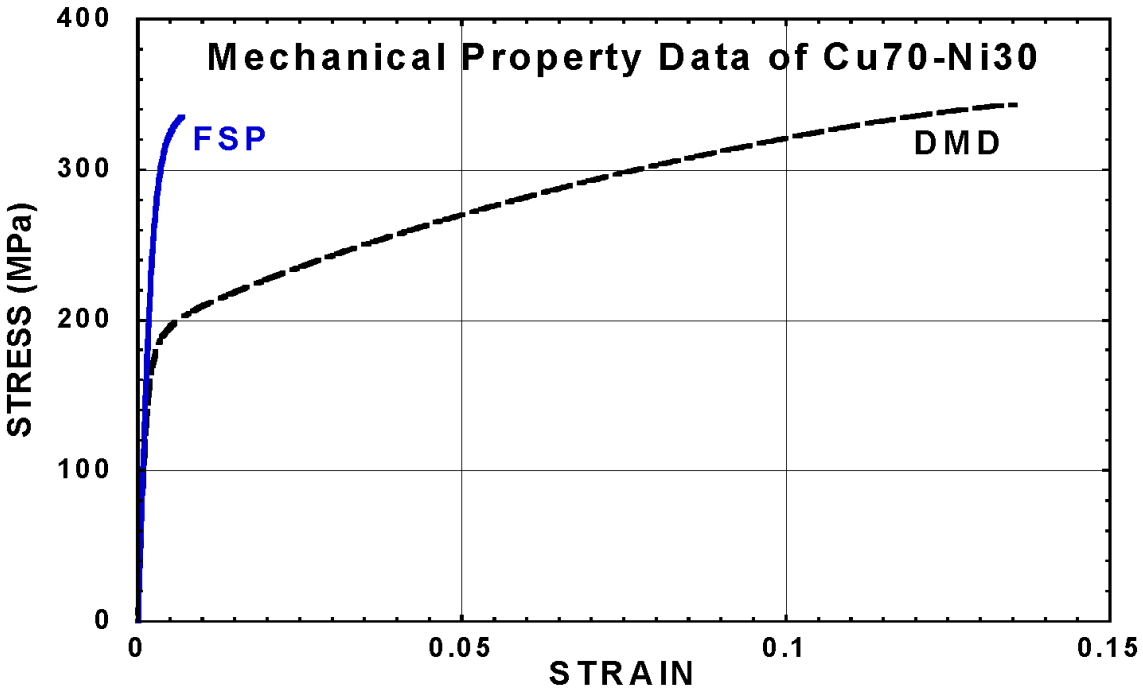

Fig. 6.14 Stress vs. strain curves for DMD and FSP Cu-Ni 70/30.

Chapter 7

Simulated Damage Repair Using Friction Stir Processing of 7475 Aluminum

Abstract

Friction Stir Processing (FSP) was carried out on 7475 aluminum with the objective of damage repair. Three different pin geometries were experimented with to carry out single and overlapping FSP passes. Microstructural characterization, tensile test and corrosion test were performed before and after FSP. Several concepts of direct plug-based repair were demonstrated on 7475 aluminum plates without resorting to Direct Metal Deposition (DMD). Repair was also carried out on an actual torpedo fuel tank using FSP.

7.1 Introduction

7475 aluminum finds widespread use in marine environments, e.g. in torpedo fuel tanks, due to its light weight combined with high strength, superior fracture toughness and resistance to fatigue crack propagation. However aluminum is prone to corrosion when exposed to seawater. Current methods of prevention of corrosion involve anodizing the aluminum followed by application of thick paint. However, the effectiveness of coating in preventing corrosion is limited by wear. Pitting corrosion is a common phenomenon in torpedo fuel tanks.

Research is required on ways and means of preventing corrosion on fuel tanks. In addition to devising new methods of preventing corrosion, it is also important to repair and restore fuel tanks which are rendered useless due to pitting. In Chapters 5 and 6, laser assisted DMD was applied as a means of repairing damaged parts. However DMD deposition of 7475 aluminum leads to evaporative loss of low-melting magnesium and zinc from the deposit [1]. It also often creates solidification and liquation cracking in the DMD.

In this chapter direct plug-based repair of 7475 aluminum part without DMD is discussed. Several concepts of repair, demonstrated on 7475 aluminum plates, can be easily extended to repair a torpedo fuel tank. A technique of repairing an actual torpedo fuel tank using FSP is also discussed. The difficulties encountered in the process were the thin-shell and curvature of the tank as well as the exit hole that FSP leaves as the tool withdraws from the work-piece. Detailed discussions on the ways and means to circumvent these problems are presented.

7.2 Experimental

7.2.1 FSP Using Scrolled Pin Geometry

A 304.8mm × 304.8mm × 19.05mm 7475-T7651 aluminum plate was procured from Kaiser Aluminum Inc. The composition of 7475 aluminum is shown in Table 7.1. FSP was performed using a scrolled pin geometry which is shown in Fig. 7.1A and Fig. 7.1B. The tool contained a scrolled concave shoulder and a scrolled conical pin. The concave shoulder allows the material to rise under pressure. The scrolled geometry allows

material to seamlessly flow from the edge of the shoulder to the center and from the base of the pin to the tip.

The tool rotation rate used during FSP is 1000rpm counterclockwise. Two different feed-rates were used, i.e., 25.4mm/min and 101.6mm/min. A defect-free stir zone was created under both conditions. Since the higher feed-rate lowers the processing time, a feed-rate of 101.6mm/min was chosen to perform FSP over an area by overlapping passes. The objective of processing an area was to extract specimens for tensile and corrosion test. The spacing between individual passes was 1.5mm which resulted in significant overlap between two consecutive passes. Also the advancing side of one pass was overlapped by the retreating side of the next pass.

Vickers microhardness was measured along various regions of both single FSP pass and overlapping FSP passes. Corrosion test specimens were extracted from as-received and FSP 7475 aluminum samples. All corrosion specimens were sent to Corrosion Testing Laboratories Inc., Newark, Delaware, USA. The specimens were rectangular in shape of dimension 50.8mm × 25.4mm × 3.3mm. The specimens had a 3.2mm diameter through-hole at one side to keep it suspended using a string. The corrosion rate was determined by exposing the specimens to synthetic seawater at laboratory ambient temperature (20°C) for 30 days as per ASTM-G31 standard. The test solution was prepared from commercially available synthetic seawater salt (Lake Products, Maryland Heights, Missouri, USA) that met ASTM D1141 standard. The salts were dissolved in de-ionized water to prepare the final test solution which had a pH of 8.2. A poly-tetra-fluoro-ethylene string was used to keep the test specimens suspended and totally immersed in the test solution. The test vessel was sealed off for the remainder of duration of the test.

After 30 days of exposure the test specimens were removed, cleaned, reweighed and visually evaluated.

Tensile test specimens were extracted from as-received and FSP 7475 aluminum samples and were tested in-house. The specimen had a gage length of 15.2mm, a gage width of 6.5mm and a gage thickness of 3.3mm. It also had a shoulder region of radius 6.35mm and a grip section of length 15.5mm on both sides. For the FSP sample the longitudinal axis of the tensile test specimen was parallel to the FSP pass direction. Room temperature tensile tests were performed at a constant crosshead speed of 0.5mm/min.

7.2.2 FSP Using Partially-Scrolled and Pyramidal Pin Geometry

The objective of this work was to investigate the effects of pin geometry on stir zone. Improper pin geometry can create defects in the stir zone, whereas proper pin geometry creates void-free stir zone, reduces process-load and prolongs tool life. The focus of this work was to study the effect of pin geometry on material flow and deposition within stir zone. The partially-scrolled pin geometry is shown in Fig. 7.2 and the pyramidal pin geometry is shown in Fig. 7.3. The partially scrolled geometry is essentially the scrolled geometry (Fig. 7.1) with four flat regions. The edges of scrolls and their intersection points with flats are regions of sharp curvature. In comparison the pyramidal pin geometry is relatively smooth with only the edges of the pyramid having a gentle curvature. In essence these two pin geometries represent the two extremes of rough and smooth pin geometries. Partially scrolled pin geometry was run with three different rotation rates i.e. 1000rpm, 1500rpm and 2000rpm and three different feed rates i.e. 12.7mm/min, 25.4mm/min and 50.8mm/min. Pyramidal pin geometry was run with three

different rotation rates i.e. 250rpm, 500rpm and 1000rpm and three different feed rates i.e. 12.7mm/min, 25.4mm/min and 50.8mm/min. A 3° back-tilt of the tool was used in both cases.

7.2.3 Simulated Damage Repair in a Flat Plate Using FSP

The concept of damage repair is fairly simple and integral to the process of FSP. The methodology of damage repair is shown in Fig. 7.4. A 50.8mm × 3.2mm × 3.2mm groove was machined in a 7475 aluminum plate (Fig. 7.4A). The groove simulated a damage which needed to be repaired. Two pieces of 7475 aluminum were press-fitted into the groove and FSP was performed on that region. As shown in Fig. 7.5B, FSP indistinguishably blends in the press-fitted pieces and the outer block thus completing the repair.

7.2.4 Simulated Repair of Torpedo Fuel Tank Using FSP

Torpedo fuel tanks - also referred to as AFT fuel tank in naval parlance - are cylindrical shells made of 7175 aluminum (Fig. 7.5). The length of the cylinder is ≈ 1235mm and the diameter of the cylinder is ≈ 532mm. The thickness of the cylindrical shell is ≈ 5.6mm. The fuel tanks are stored with fuel inside it, so they develop corrosion pits on the inside surface of the tank (Fig. 7.5). The pits are often through thickness and render the tank unusable. FSP was thought to be an ideal technique of repair of torpedo fuel tanks. In previous section the feasibility of plug based repair for 7475 aluminum block was demonstrated. As a natural extension of that idea a new repair method was developed wherein a hole was drilled in place of corrosion damage, filled with 7475 aluminum plug

and then processed by FSP. An image of the torpedo fuel tank with a tapped hole is shown in Figure 7.6. The hole was drilled and tapped in place of the corrosion pit. The repair of the corrosion hole in torpedo fuel tank was to be carried out under two constraints, namely, the exit hole of FSP was to be outside of the surface of the tank wall and the entire FSP operation was to be performed without having to open the fixtures and reach the interior of the tank.

In view of the aforementioned constraints a fixture was designed which rigidly clamped the fuel tank during FSP as shown in Fig. 7.7. In Fig. 7.7 a precision cut portion of a torpedo fuel tank is shown. Repair was demonstrated on a section of a torpedo fuel tank since the whole tank is too large to be handled inside the milling machine. Backup support is critical to FSP. Without proper backup support defects are generated within stir zone. Fig. 7.7A shows the backup used in this experiment. It consisted of two 1018 steel arcs which conformed to the tank inner diameter, two swivel leveling pads and a coupling nut. By tightening the coupling nut the fixture could apply radially outward pressure on the inner surface of tank. The lid of the tank was closed and the tank was locked to the work-table by means of two steel locking bars which were tightened by bolts (Fig. 7.7B).

A hole of diameter 31.75mm was drilled and tapped (Fig. 7.6). A threaded 7475 aluminum plug of the same diameter was screwed into the hole. The plug piece had a square rod that stuck out vertically (Fig. 7.8C). On top of the plug lay a wedge-shaped ramp piece made of 7475 aluminum (Fig. 7.8A, 7.8B). The function of the ramp piece was to provide material so that a FSP exit hole could be created outside the tank. The top surface of the ramp piece was flat but the bottom surface of the piece conformed to the outside surface of the tank. The ramp piece also had a square hole in the middle which

encompassed the square section of the plug (Fig. 7.8D). Thus the ramp piece was fixed in a certain angular location. The ramp piece was also secured by means of a coupling nut, a lock nut and locking piece as shown in Fig. 7.9. The lock nut applied pressure on the locking piece which in turn fixed the tail end of the ramp. The coupling nut locked the front end of the ramp piece. Once the ramp piece was secured by means of fasteners, FSP was used to permanently join the ramp piece with the tank wall. This was accomplished by an FSP pass as shown in Fig. 7.10. The FSP pass started from start point S, went halfway around the plug and finished at F. The tool path ran along the thread between the tank wall and disc thereby creating a bond between the plug, ramp and the tank wall. The FSP pass had a groove in the stir zone because a gap existed between arc support and tank inner wall where the material flowed in during FSP. However FSP fully bonded the ramp piece and the plug to the tank, so the locking fixture was removed and FSP pass was again run along the interface between plug and tank wall (Fig. 7.11). The purpose of the last FSP pass was to join the plug to the tank wall. In the finishing operation the outside surface of the tank wall was restored by removing the excess material in the plug and ramp pieces. The final surface as shown in Fig. 7.12 was slightly depressed because during FSP, the tool sank below the original surface. The problem could be avoided by using a thicker ramp piece.

7.2.5 Simulated Repair by Squashing a Rotating Plug inside a Hole Followed by FSP Using Flat Tool

The technique described in the previous section successfully joined a plug to the tank wall. However it was quite intricate in that it required preparation of a ramp piece with

complicated geometry. Also the ramp piece material was machined off after FSP which is undesirable. In the following sections, techniques of repair without making a ramp piece will be described. One such technique is illustrated in Fig. 7.13 where a plug was used to fill in and repair a hole. The concept of repair was demonstrated in a flat plate although the technique is equally applicable on a cylindrical shell. Here the plug-diameter was slightly smaller than the hole-diameter so that it could enter the hole smoothly. The plug was taller (5.8mm) than the depth of the hole (4.8mm) so that the plug-volume was greater than the hole-volume. This ensured that the plug could completely fill the hole when squashed. The plug was rotated at a very high rpm (5000 rpm) so that sufficient heat was generated. Initially the plug was slowly inserted (feed-rate 0.25mm/min) in the hole so that the bottom of the hole and the plug came into contact and heated up. The heat softened the plug and allowed smooth flow of material. Following this the plug was plunged rapidly at a rate of 1mm/min until the whole plug volume was squashed. After this the tool rotation and feed-rate were stopped simultaneously to allow the bond to set in. Next the top of the plug was machined off and FSP was performed using a flat shoulder tool to process the top surface (Fig. 7.13).

7.2.6 Simulated Repair by Squashing a Series of Discs inside a Hole

Another concept of repair is illustrated in Figure 7.15 with two discs which could be smoothly inserted inside the hole. The disc was squashed inside the hole by a flat FSP tool rotating at a high rpm (2000 rpm). The frictional heat and applied load ensured that the material flowed and filled up all the voids. Enough pressure was applied with the FSP tool so that the entire disc underneath the tool was engulfed by the shear flow and bonded

with the underlying hole. Then another disc was used on top of the disc previously used. The entire hole was filled up in this process. The actual hole-diameter used in the experiment was 12.7mm and depth was 4mm. Four discs of diameter 12.7mm and thickness 1.5mm were used to fill up the hole.

7.3 Results and Discussion

7.3.1 FSP Using Scrolled Pin Geometry

The microstructure of 7475 aluminum FSP nugget for a feed-rate of 25.4mm/min using scrolled pin is shown in Fig 7.17. Note that the nugget has a ring-shaped dark and white contrast similar to onion-ring structure found in conventional tool nuggets. The banded contrast appears due to varying grain-size as well as precipitate density [2].

Fig. 7.18 shows the microstructure of overlapping FSP passes as well as the hardness variation along a line CD 2mm below the top surface. During the overlapping of FSP passes the material undergoes a complicated thermal cycle. Each FSP pass generates some heat which raises the temperature of the overall workpiece. Therefore each FSP pass occurs at a slightly higher temperature than its previous pass. In Fig. 7.18 the rightmost FSP pass is pass#10 and the leftmost FSP pass is pass#18. The higher temperature at FSP pass#18 leads to more dissolution of constituents on that side. On cooling more precipitates form on that side thus imparting higher hardness.

Table 7.2 summarizes the mechanical property data of as-received and FSP aluminum. It is observed that FSP leads to a reduction in strength and increase in ductility. This is because the base material has an optimum T7 heat treatment. During FSP not all the constituents go to solution. So after FSP when the precipitates form, the amount of

precipitates in the nugget is less than that in base metal. This explains the reduction in strength.

Table 7.3 summarizes the corrosion rate of as-received and FSP aluminum. The corrosion behavior of FSP 7475 is better than as-received 7475 aluminum. The reason is that the as-received 7475 Al has more number of precipitates. The distortion along the precipitate/matrix boundary increases the number of corrosion sites.

7.3.2 FSP Using Partially-Scrolled and Pyramidal Pin Geometry

Before discussing the nugget zone microstructure a study on unetched FSP 7475 aluminum was conducted. Fig. 7.19 shows two micro-images of nugget zone at two different magnifications. In Fig. 7.19A, large 1-2μm diameter iron-bearing constituents and rod-shaped precipitates are observed. In Fig. 7.19B EDS analysis reveals that the rod shaped precipitates are rich in zinc, copper and magnesium. Fig. 7.20 shows the effect of etching on FSP 7475 aluminum. The etchant used here is Keller's reagent (1ml HF + 1.5ml HCl + 2.5ml HNO_3 + 95ml H_2O). The sample was first etched for 1 sec and then subsequently for an additional 4 sec. After 1 sec etching it was observed that the etchant preferentially attacks grain boundary phases which are rich in zinc, copper and magnesium. Voids are formed by dissolution of nano-precipitates. Continued etching leads to the formation of local cracks along grain boundaries. The voids and cracks in the etched microstructure are thus artifact of etching.

Fig. 7.21 shows the microstructure of FSP nuggets for various rpm and feed-rate combinations using partially scrolled pin geometry. It's observed that high rate of rotation (2000 rpm) creates void in the nugget zone. High rpm leads to high temperature

during FSP thus causing low-melting phases along grain-boundary to melt leading to intergranular fracture. However lower rpm generally gives defect-free stir zone. Fig. 7.22 shows the microstructure of FSP nuggets for various rpm and feed-rate combinations using pyramidal pin geometry. For the 250 rpm case microstructure could only be obtained for a feed-rate of 12.7mm/min. For the rest of the run a deep groove forms due to insufficient contact load. In all cases the nugget region shows elongated defects at the advancing side and approximately parallel to the pyramidal surfaces. The void size reduces with increasing rpm but increases with feed-rate. This indicates the possible relationship between void size and temperature. In general however defects are likely to occur with smooth pin geometry because it doesn't create vertical movement of material in the nugget zone which is critical to creating defect-free stir zone.

7.3.3 Simulated Repair by Squashing a Rotating Plug inside a Hole Followed by FSP Using Flat Tool

Fig. 7.14 shows the microstructure of a rotating plug squashed at a very high rate of rotation (5000 rpm) followed by flat tool FSP. The repair methodology is described in Fig. 7.13. The microstructure shows evidence of material flow characteristic of the two-step repair process. During the first step the rotating plug undergoes compressive loading against the bottom of the hole at high temperature. The arrows indicate material flow towards the bottom followed by a radially outward movement. Evidence of recrystallization on the side walls also suggests that material flows radially outward and undergoes shear along the side walls. However gaps remain on certain locations of the side walls and the bottom surface suggesting that the contact stress was not uniform. The

material flow due to the flat FSP tool is apparent in that every material point at a depth up to ~1.5mm from the top surface undergoes heavy shear. The grains within the plug as well as the plug-plate interface bend towards left under compressive and shear load.

7.3.4 Simulated Repair by Squashing a Series of Discs inside a Hole

Fig. 7.16 shows the microstructure of repair performed by stacking four thin discs. The repair methodology is described in Fig. 7.15. From the microstructure it appears that all the interfaces between the plug and the hole came under severe load under which the interface became wavy. Very high hot work is evident in the microstructure due to which grains became refined. Interfaces in the side deformed under compressive load and high temperature. The combined volume of the plugs was greater than the volume of the hole. It was observed that the extra plug material leaked through the side interface and formed flash on the top surface. The bonding is good on the bottom surface close to the axis of the hole where the temperature was the highest. However at the edges of the bottom surface of plugs, gaps remain.

7.4 Summary and Conclusions

FSP of 7475 aluminum was performed using three different pin geometries – a scrolled pin, a partially scrolled pin with flats and a pyramidal pin. The scrolled pin and the partially scrolled pin yield defect-free stir zone under certain processing conditions. However the pyramidal pin yield voids in the stir zone under all conditions. The as-received 7475 aluminum had a rolled and elongated grain structure. After FSP the grain structure became equiaxed and recrystallized. FSP of 7475 aluminum leads to a reduction

in strength, increase in ductility and lowering of corrosion rate in artificial seawater. The feasibility of plug-based repair of torpedo fuel tank was demonstrated. Repair of a torpedo fuel tank with a large corrosion hole was successfully carried out using a threaded plug. Plug-based repair without using the ramp piece was attempted with two different techniques. In the repair technique by stacking of thin discs, the interface between discs and the hole got hot and severely deformed thus creating conditions for an effective repair.

7.5 References

[1] M.J. Cieslak, P. W. Fuerschbach, *Metall. Trans.* B 19B, (1988) 319

[2] M.W. Mahoney, C.G. Rhodes, J.G. Flintoff, R.A. Spurling, W.H. Bingel, *Metall. Mater. Trans.* A 29A, (1998) 1955

Zn	Mg	Cu	Si	Fe	Mn	Cr	Ti	Other	Al
5.2 - 6.2	1.9 - 2.6	1.2 - 1.9	0.1	0.12	0.06	0.18 - 0.25	0.06	0.15	Bal

Table 7.1: Composition in wt% of 7475 aluminum alloy.

	0.2 % Yield Strength (MPa)	UTS (MPa)	Ductility
As-received 7475 Al	222.7	372.3	16%
FSP 7475 Al	177.9	341.0	22%

Table 7.2: Mechanical property data of 7475 aluminum.

Sample	Corrosion Rate (micron/yr)
As-received 7475 aluminum	7.4
FSP 7475 aluminum	2.5

Table 7.3: Corrosion rates of 7475 aluminum under various processing conditions.

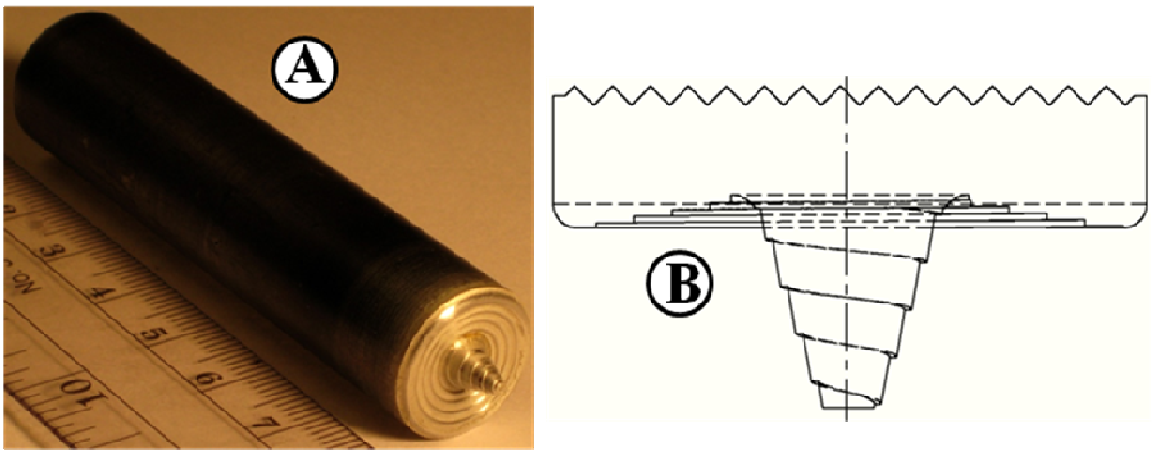

Fig. 7.1 (A) Image of scrolled H13 tool. (B) Schematic of H13 tool showing scroll in shoulder and pin.

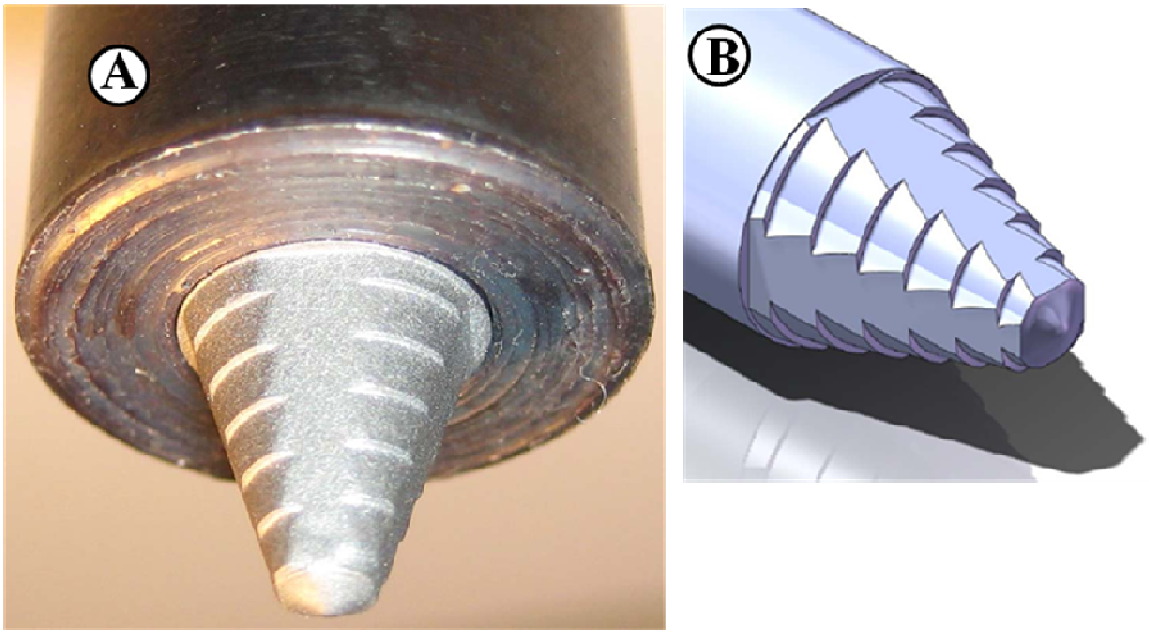

Fig. 7.2 (A) Image of partially scrolled H13 tool. (B) Schematic of partially scrolled H13 tool.

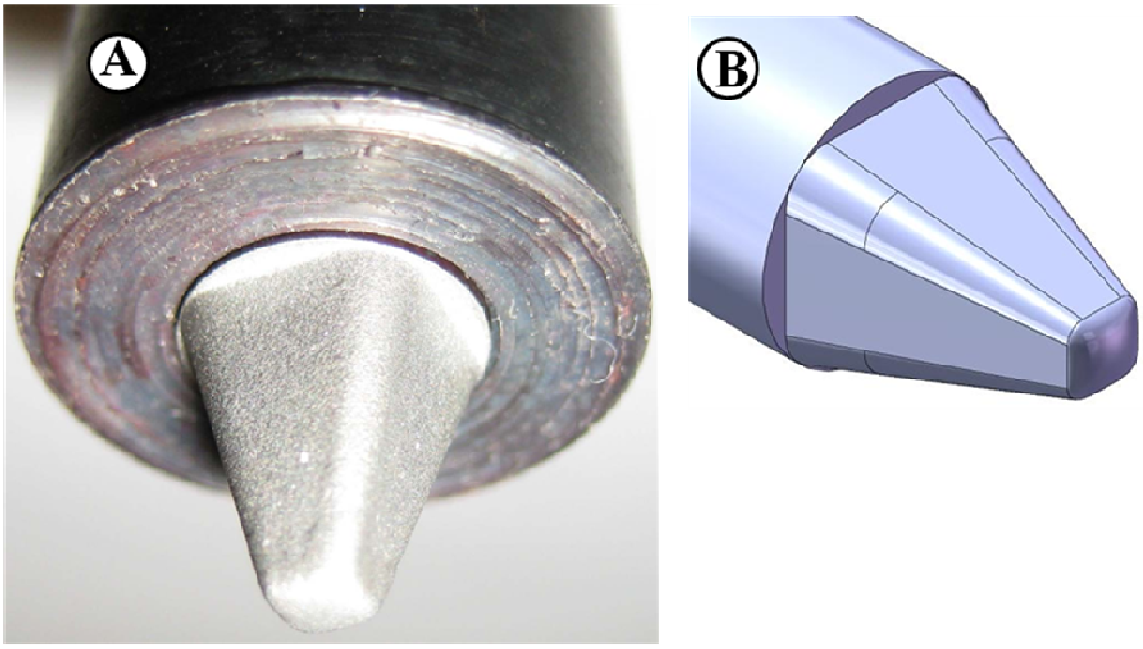

Fig. 7.3 (A) Image of pyramidal H13 tool. (B) Schematic of pyramidal H13 tool.

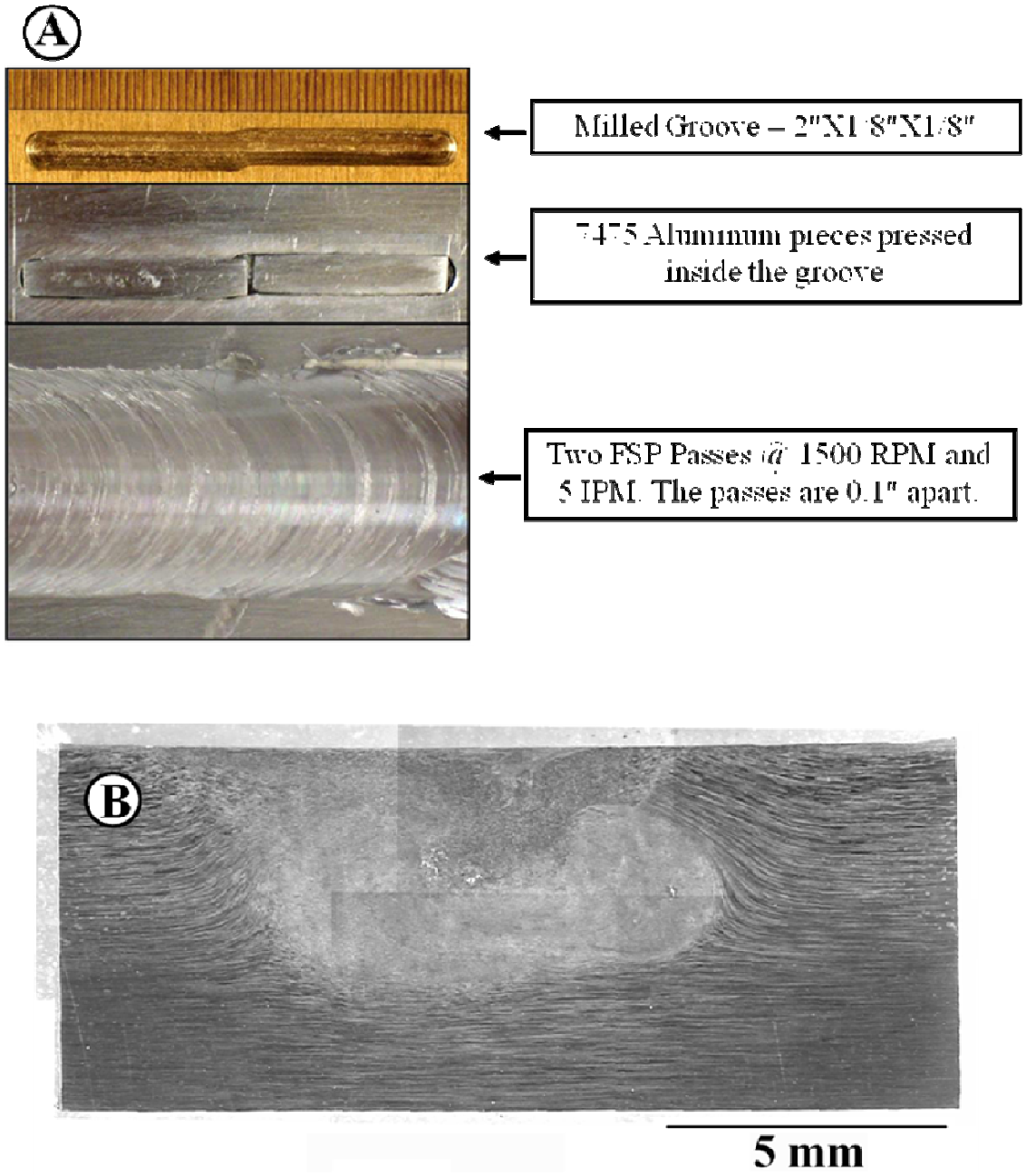

Fig. 7.4 (A) Methodology of repair of a machined groove. (B) Cross-sectional microstructure after FSP repair.

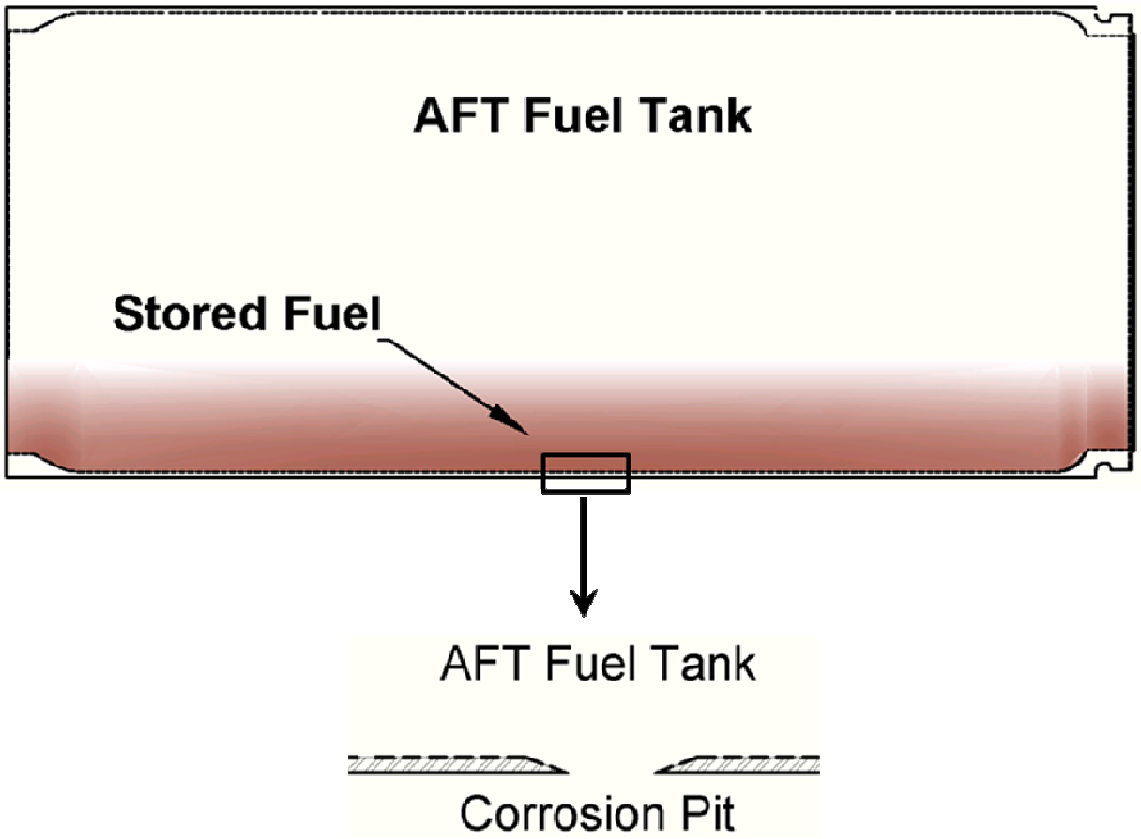

Fig. 7.5 A torpedo fuel tank with stored fuel. The inner surface of the fuel tank develops corrosion pits which can be through-thickness.

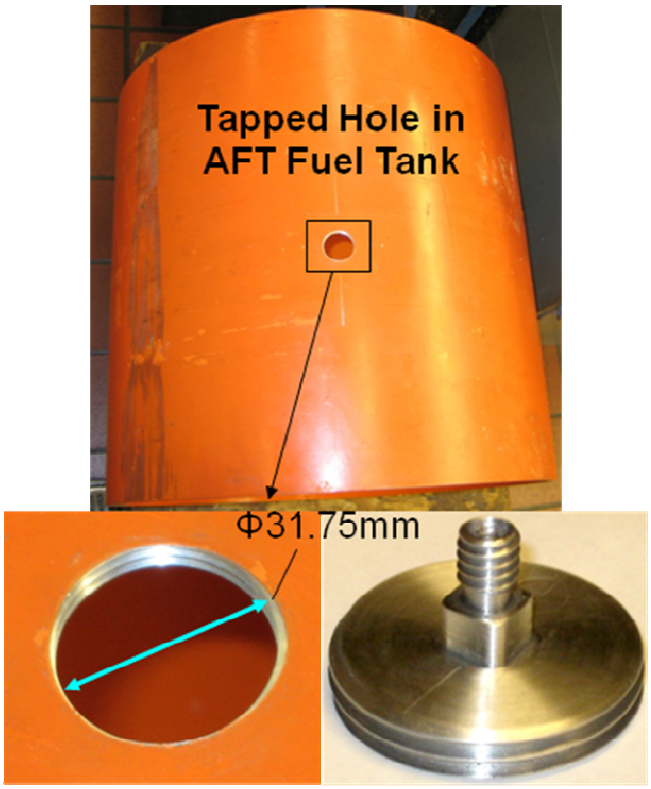

Fig. 7.6 The corrosion pit on tank wall is replaced by a machine and tapped hole of diameter 31.75mm. A plug which threads into the hole is also shown.

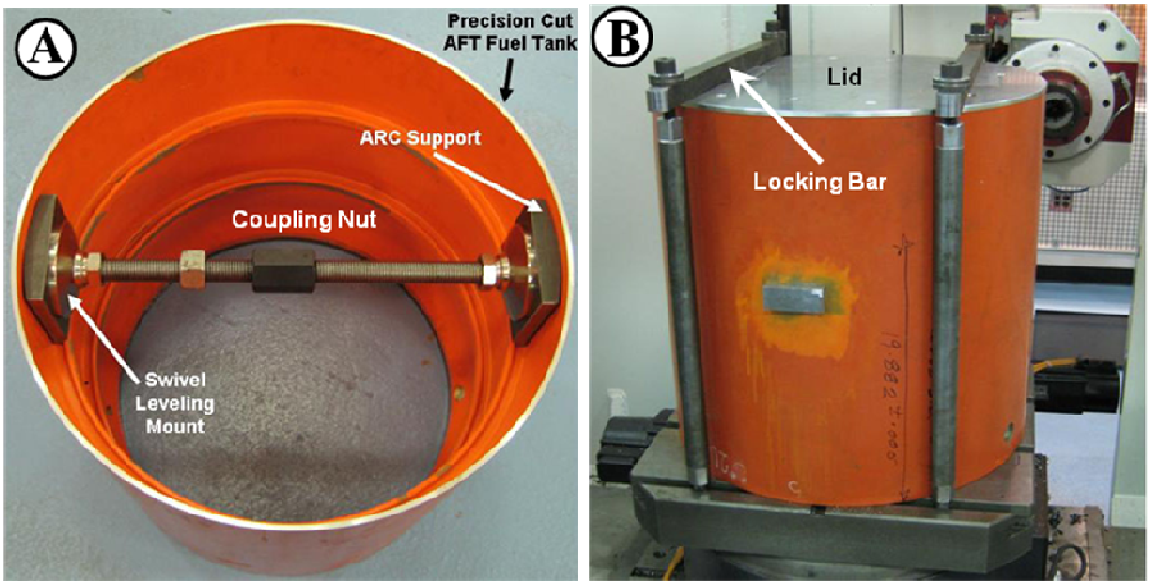

Fig. 7.7 (A) Back-up fixture to support the plug during FSP. Back-up fixture consists of two steel arc-supports, two swivel leveling mounts and a coupling nut. (B) The fuel tank is rigidly clamped to the work-table by a locking bar and screws.

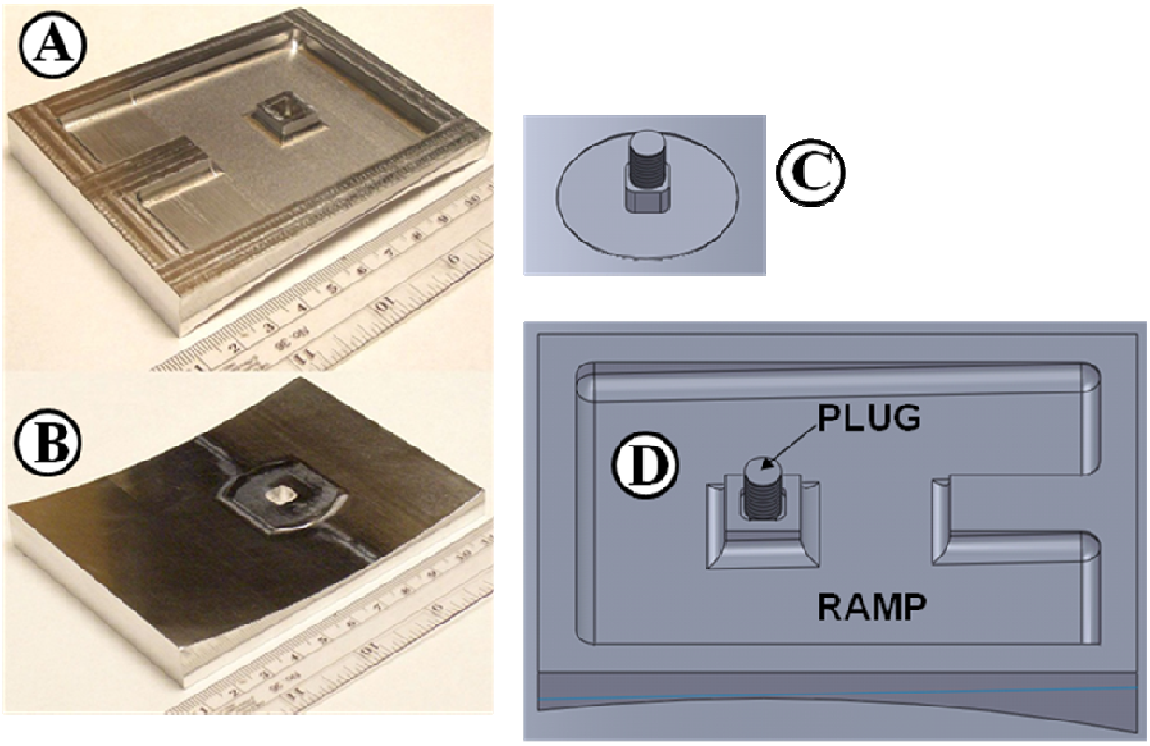

Fig. 7.8 (A) Top view of ramp piece. (B) Bottom view of ramp piece. (C) Schematic of plug threaded inside the hole. (D) Ramp piece installed on tank surface.

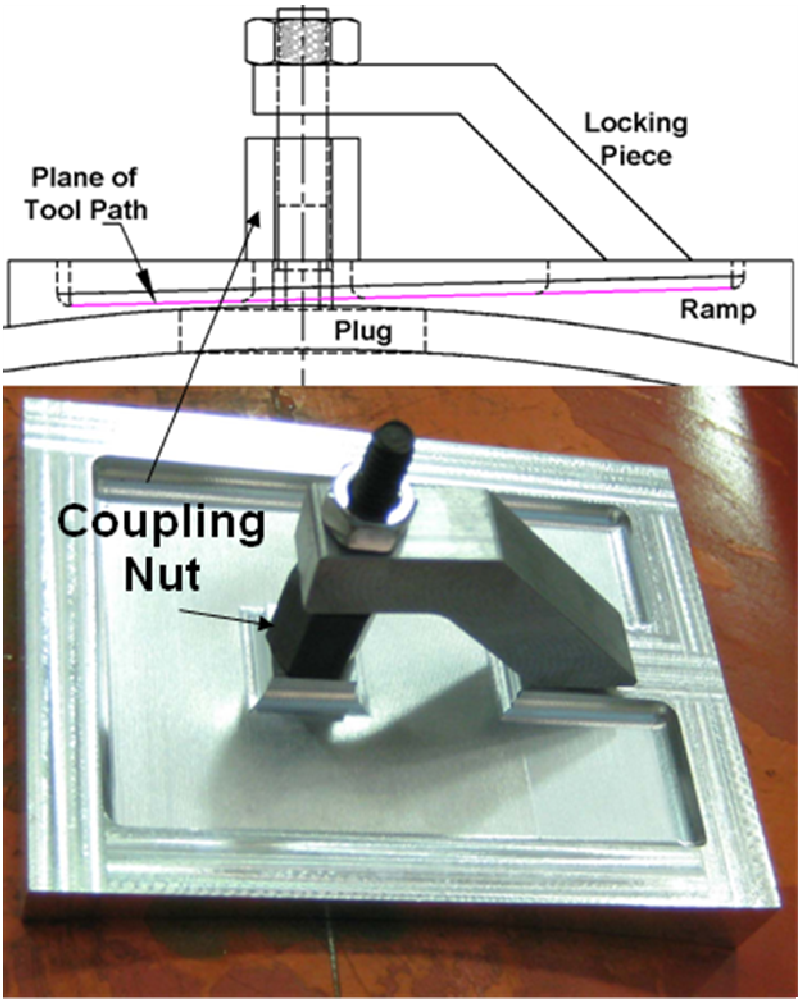

Fig. 7.9 Schematic and actual image of securing the ramp piece.

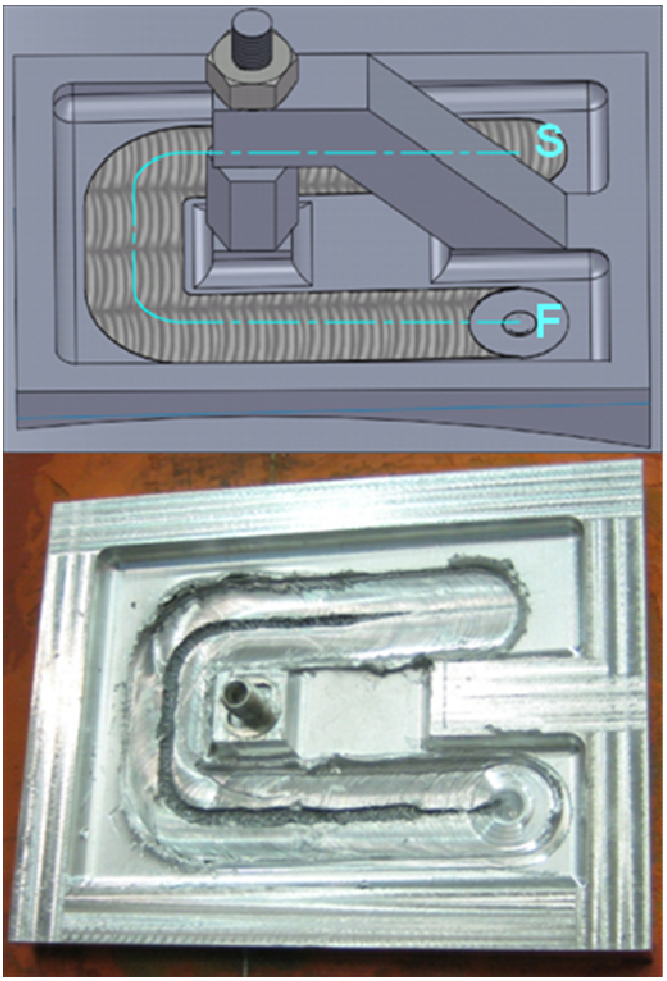

Fig. 7.10 Schematic and actual image of FSP pass to join the ramp piece and plug to the tank wall.

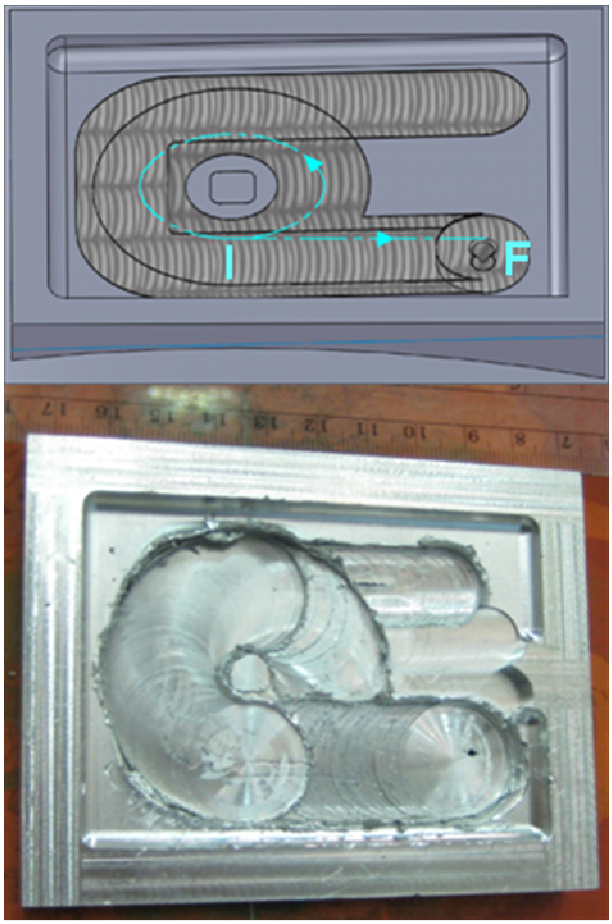

Fig. 7.11 Schematic and actual image of FSP pass along the interface between plug and tank wall.

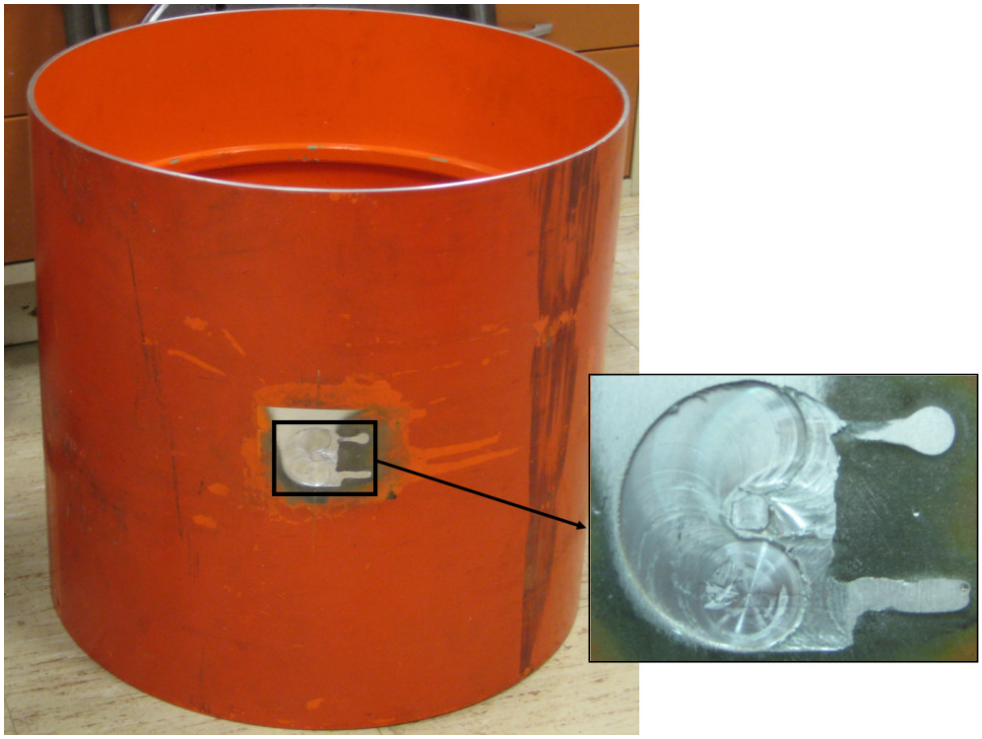

Fig. 7.12 A torpedo fuel tank after simulated repair.

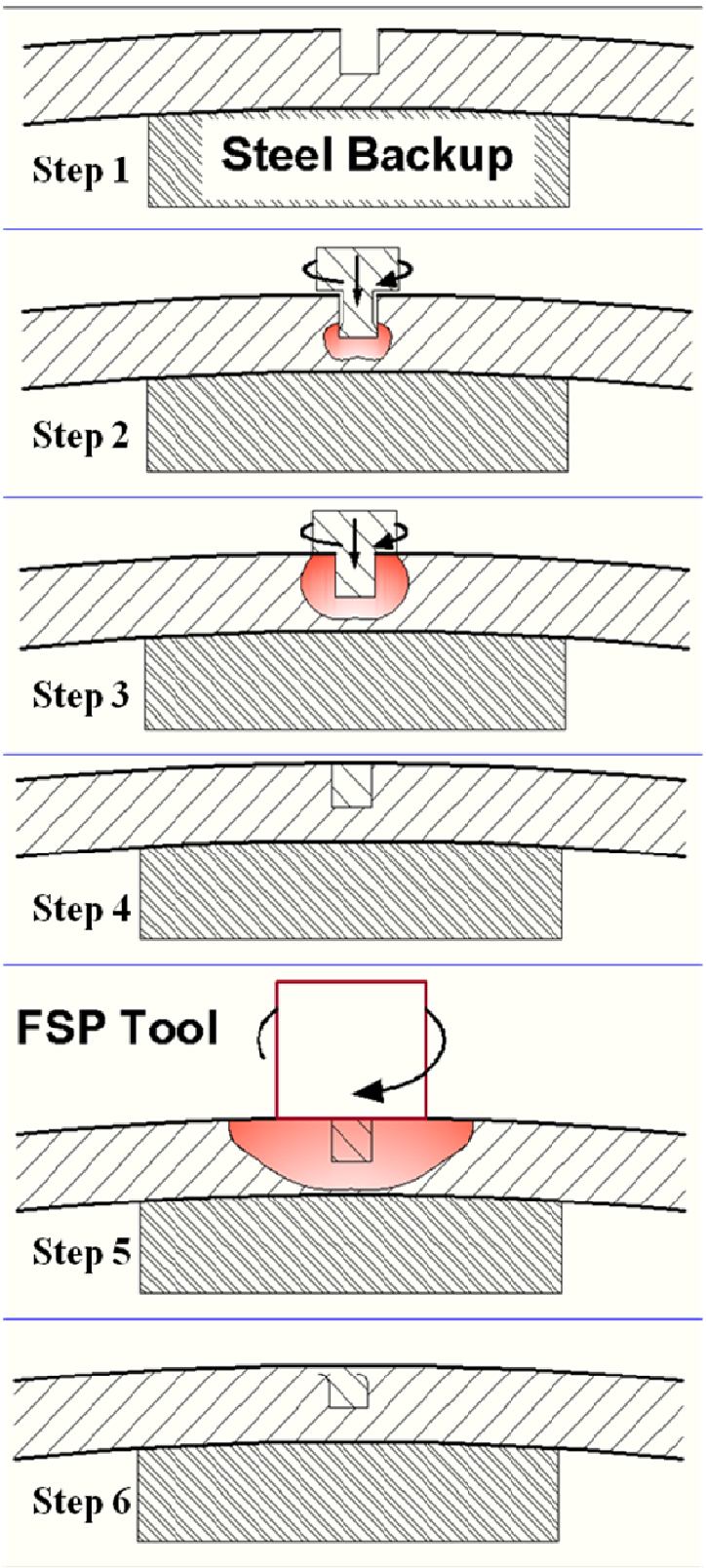

Fig. 7.13 Steps of repair by squashing a rotating plug inside a hole followed by FSP using flat tool.

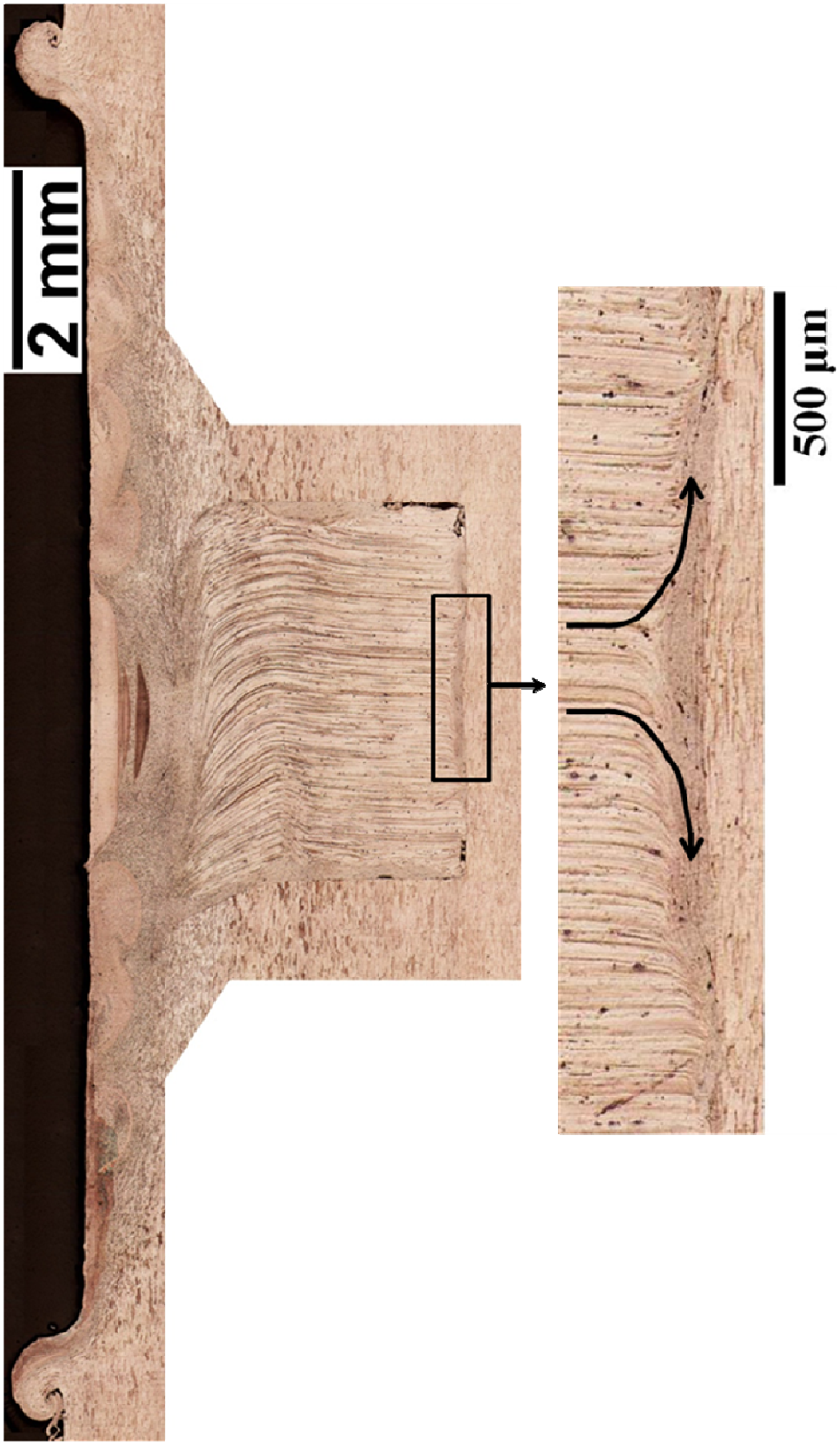

Fig. 7.14 Microstructure after repair described in Fig. 7.13.

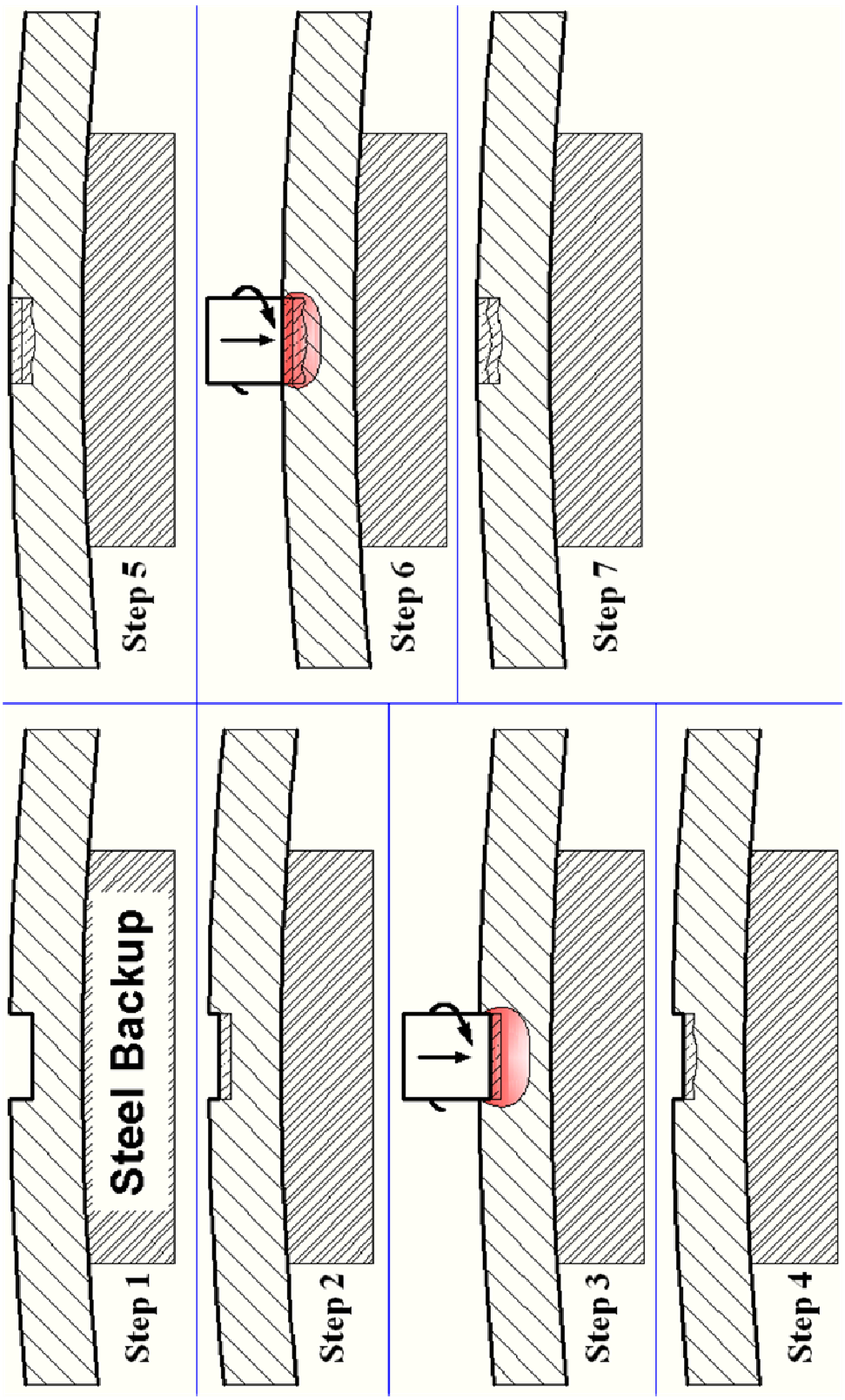

Fig. 7.15 Steps of repair by squashing a series of discs inside a hole.

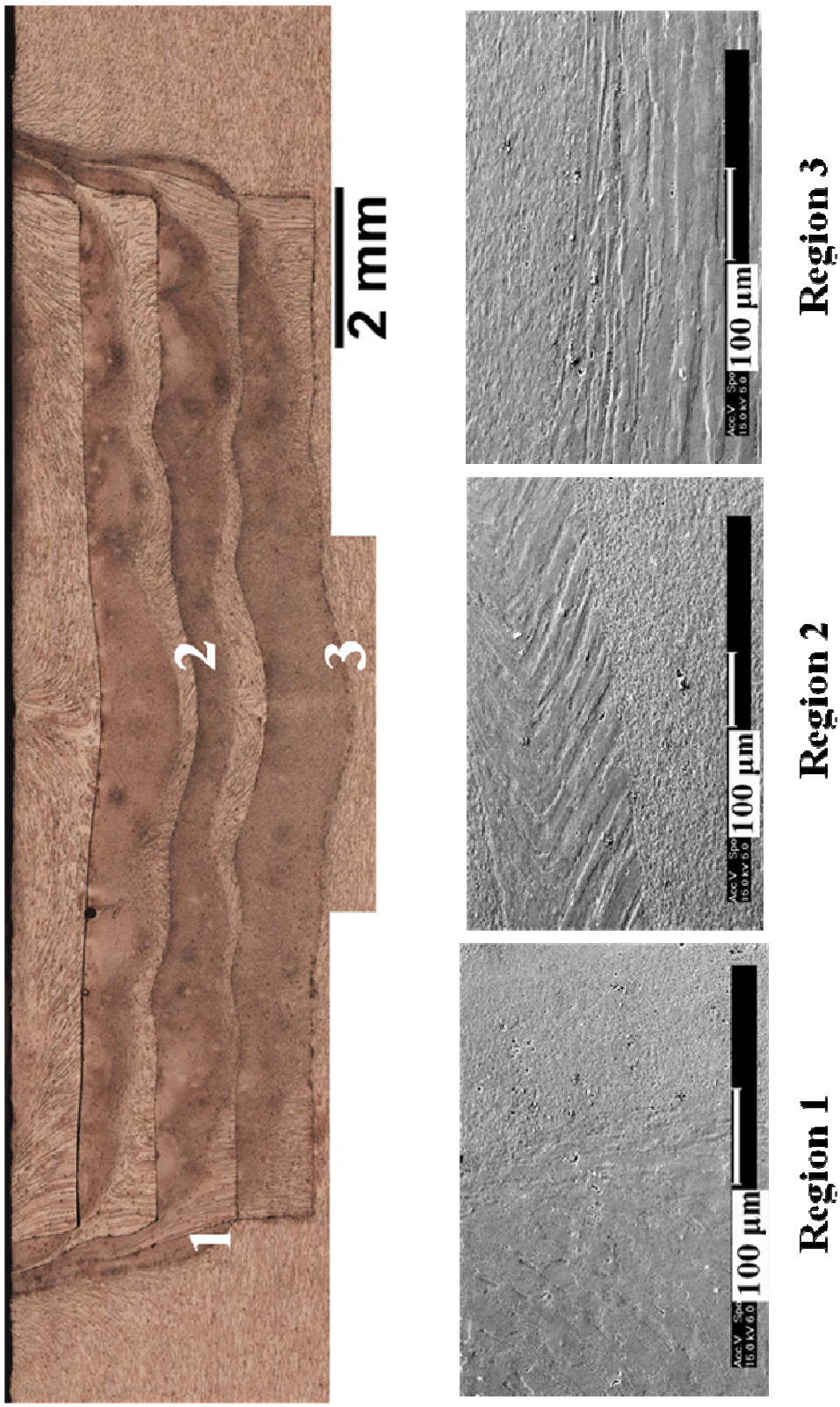

Fig. 7.16 Microstructure after repair described in Fig. 7.15. Magnified microstructures of regions 1, 2 and 3 are shown.

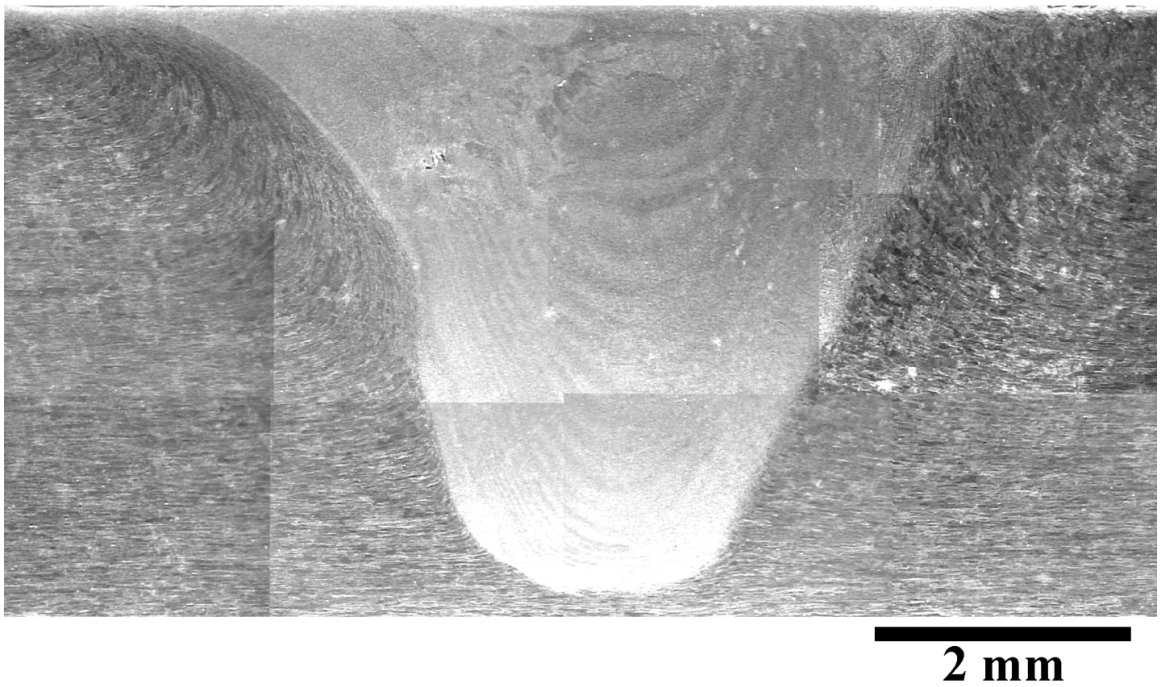

Fig. 7.17 Microstructure of a single FSP pass using scrolled tool.

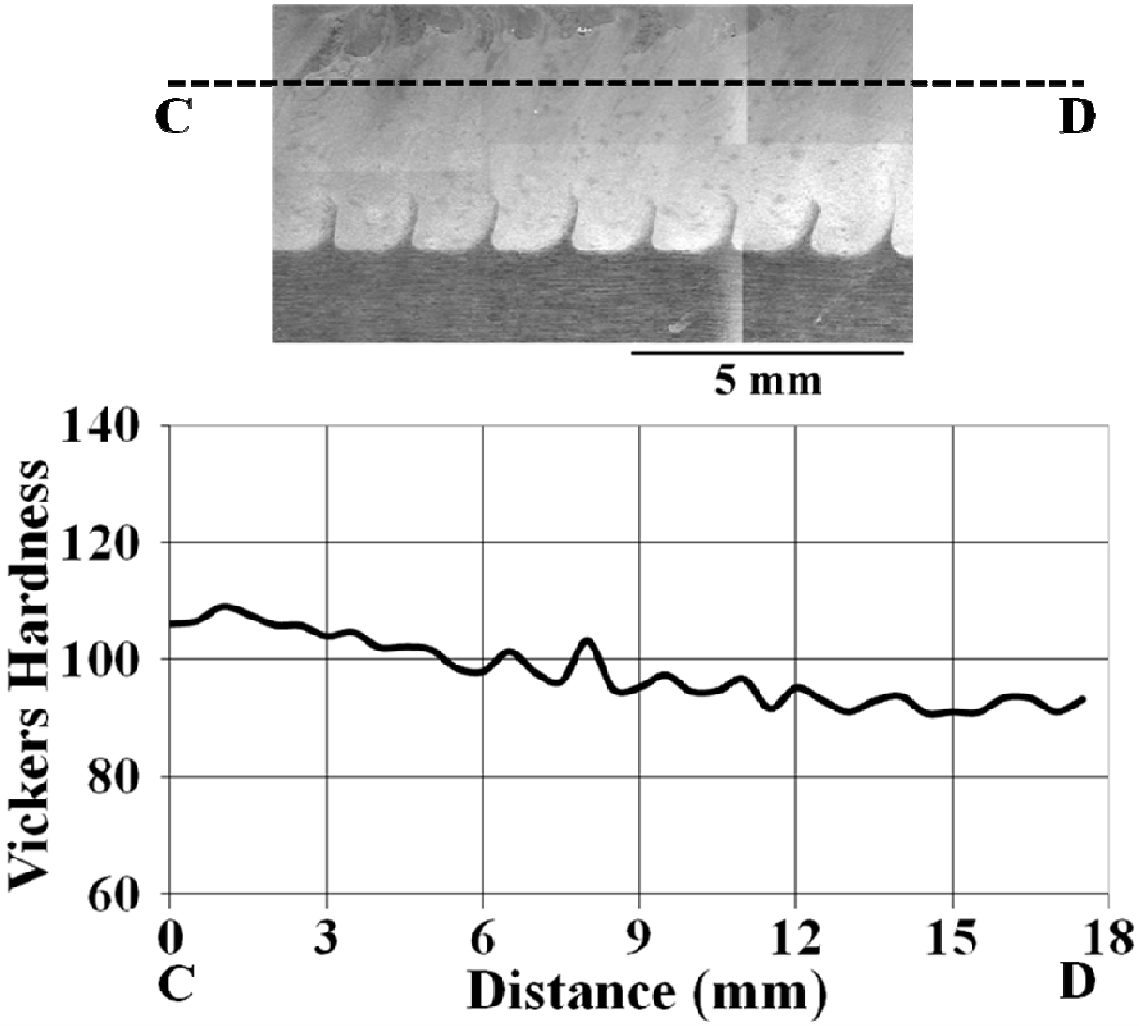

Fig. 7.18 (Top) Microstructure of overlapping FSP passes using scrolled tool. (Bottom) Hardness profile along the line CD in the process zone.

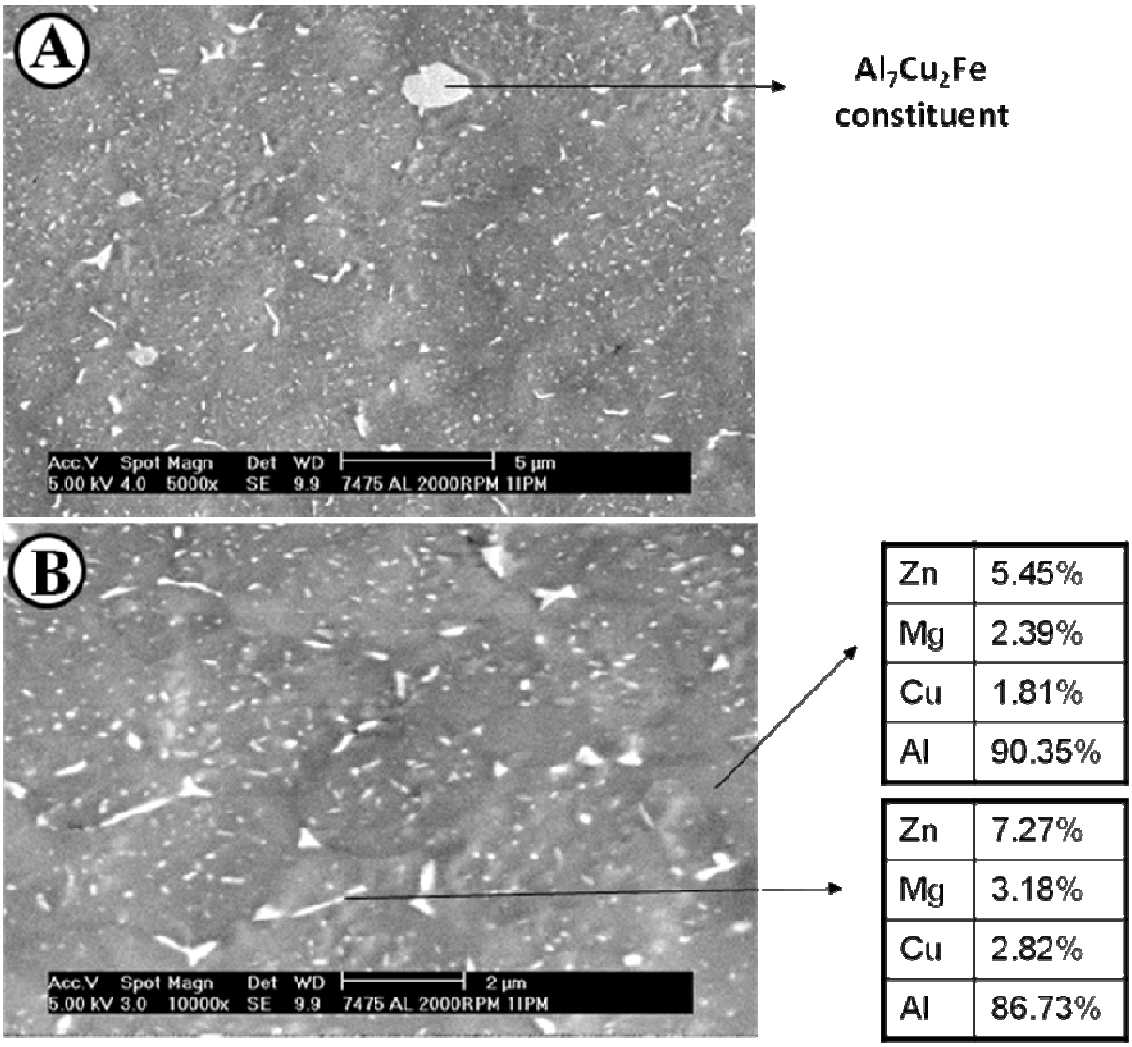

Fig. 7.19 (A) Unetched 7475 aluminum microstructure showing iron bearing constituent. (B) Unetched 7475 aluminum microstructure showing rod shaped precipitates with high concentration of zinc, magnesium and copper.

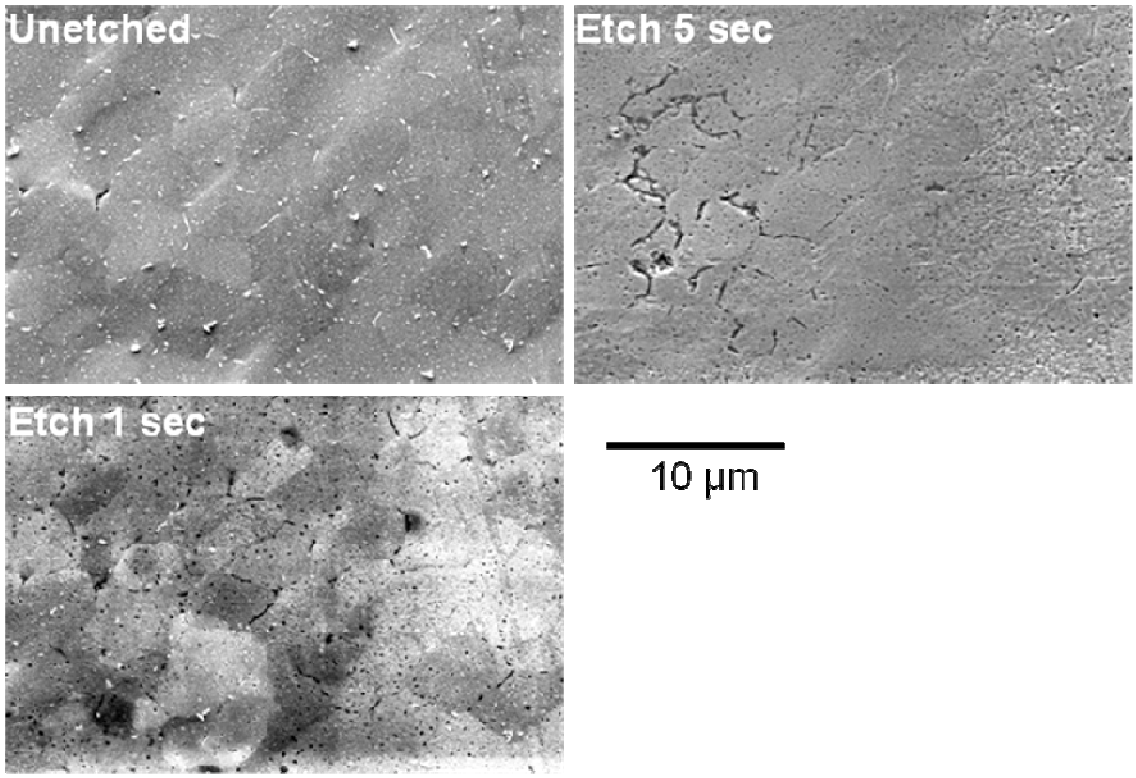

Fig. 7.20 Effect of etching time on microstructure. Etchant used is Keller's reagent. Etchant preferentially attacks the solute-rich grain boundary phases.

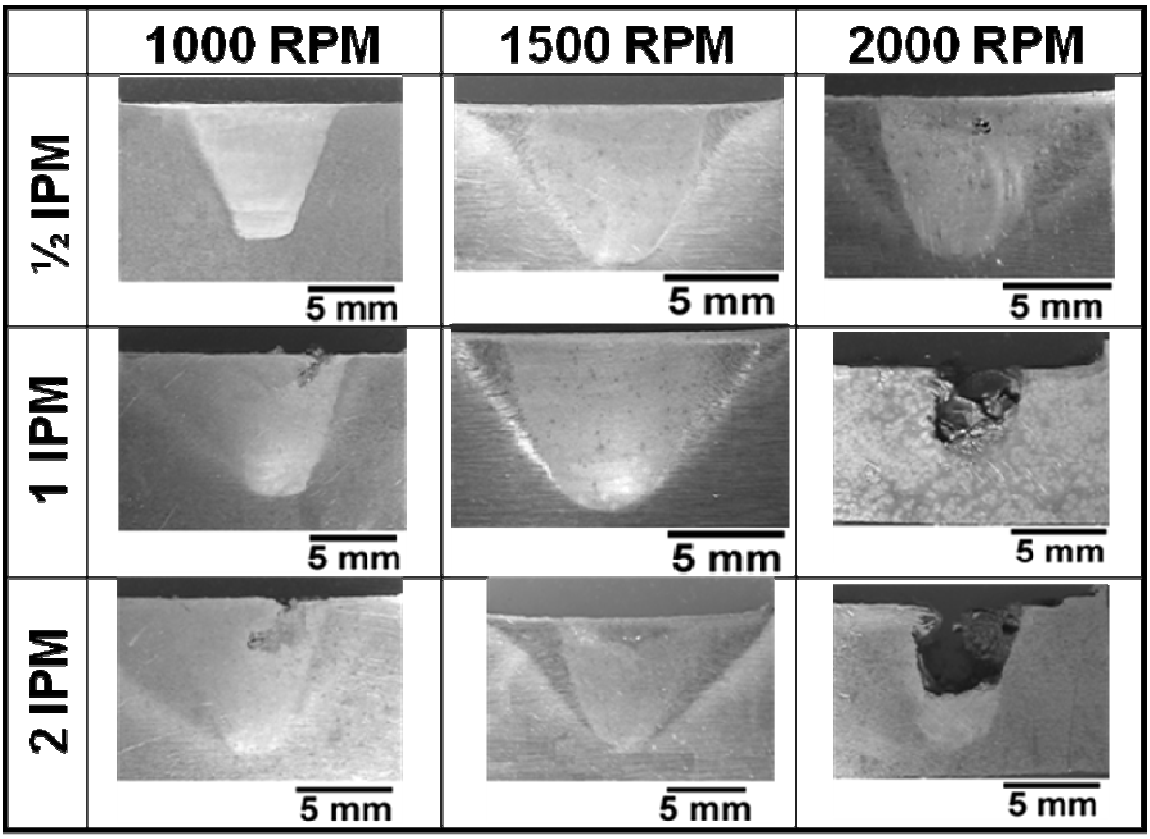

Fig. 7.21 Effect of rate of rotation and feed-rate on FSP microstructure. Partially scrolled pin-geometry is used.

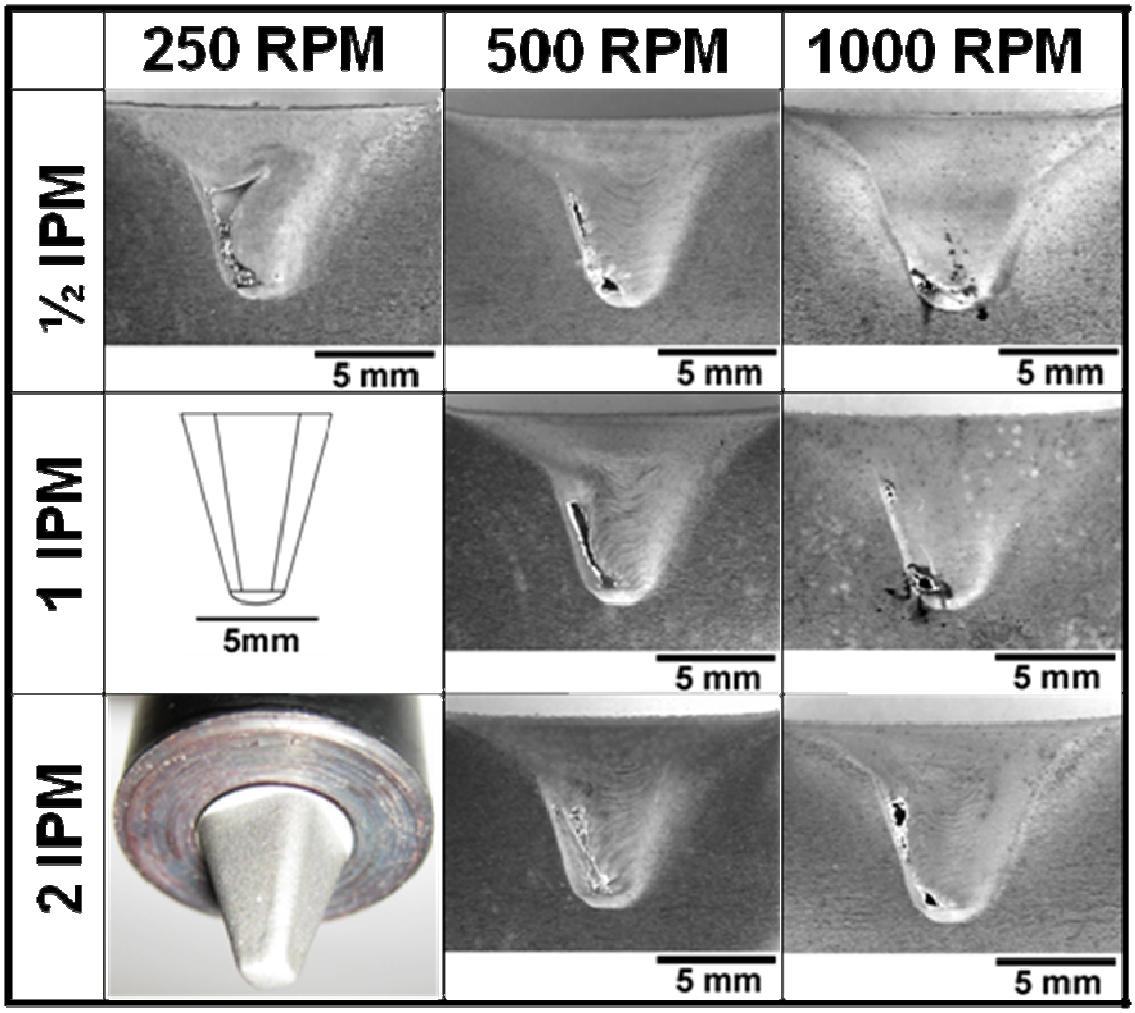

Fig. 7.22 Effect of rate of rotation and feed-rate on FSP microstructure. Pyramidal pin-geometry is used.

Chapter 8

Friction Stir Processing of 4047 Aluminum

Abstract

Friction Stir Processing (FSP) was carried out on Direct Metal Deposited (DMD) 4047 aluminum with the objective of microstructural modification. Microstructural characterization, tensile test and corrosion test were performed before and after FSP. It was observed that FSP led to agglomeration of silicon particles, enhanced ductility without affecting the corrosion rate in DMD 4047 aluminum.

8.1 Introduction

In chapter 7 the repair of a marine component made of 7475 aluminum was discussed. High strength 7475 aluminum was used to make plugs for simulated repair of the shell of a torpedo fuel tank. The shell of the tank is exposed to high pressure of undersea environment, so the structural integrity repair on the tank shell becomes extremely important. However structural integrity is not always a consideration for repair. The wire coil cover of the fuel tank contains O-ring grooves which also undergo corrosion and dimensional change. O-ring grooves do not experience lot of stress, so the repair can be performed by an aluminum alloy which is not necessarily high-strength but which is amenable to laser deposition.

4XXX series aluminum alloys have high fluidity and resistance to shrinkage porosity [1] which makes them ideally suited for laser deposition. A previous study [2] on cast aluminum-silicon A356 alloy has indicated that FSP results in a significant breakup of coarse acicular silicon particles, thus creating a homogeneous distribution of silicon particles in the aluminum matrix. In this chapter the effect of FSP on laser deposited DMD 4047 aluminum alloy is discussed. Microstructural characterization, mechanical property and corrosion behavior was evaluated before and after FSP.

8.2 Experimental

4047 aluminum laser-deposited on 7475 aluminum substrate was supplied by POM Group Inc., Auburn Hills, Michigan, USA. The DMD layer dimension was 280mm × 280mm × 7.5mm. The chemical composition of DMD 4047 aluminum is shown in Table 8.1.

FSP of DMD 4047 aluminum was carried out under three different rpm, e.g., 1500 rpm, 2000 rpm and 3000 rpm and two different feed-rates, e.g., 63.5mm/sec and 127mm/sec. The tool had a conventional threaded pin and was tilted 2° towards the back with respect to the plate normal.

4047 aluminum samples were etched with Keller's reagent (1ml HF + 1.5ml HCl + 2.5ml HNO_3 + 95ml H_2O). Scanning electron microscopy was used to analyze the microstructure before and after FSP. Vickers microhardness was measured in various regions of the process zone and was related to the microstructure.

Friction stir processing of a large area required multiple overlapping FSP passes. Overlapping FSP passes were parallel to each other with an offset of 4mm between

successive passes. The offset was such that the advancing side of one pass was overlapped by the retreating side of the next pass. This was done so because defects generally arise at the advancing side. Using the scheme an area large enough to prepare tensile and corrosion test specimens was processed.

Corrosion test specimens were extracted from substrate, DMD and FSP 4047 aluminum samples and were sent to Corrosion Testing Laboratories Inc., Newark, Delaware, USA. The specimens were rectangular in shape of dimension 50.8mm × 25.4mm × 3.3mm. The specimens had a 3.2mm diameter through-hole at one side to keep it suspended using a string. The corrosion rate was determined by exposing the specimens to synthetic seawater at laboratory ambient temperature (20°C) for 30 days as per ASTM-G31 standard. The test solution was prepared from commercially available synthetic seawater salt (Lake Products, Maryland Heights, Missouri, USA) that met ASTM D1141 standard. The salts were dissolved in de-ionized water to prepare the final test solution which had a pH of 8.2. A polytetrafluoroethylene string was used to keep the test specimens suspended and totally immersed in the test solution. The test vessel was sealed off for the remainder of duration of the test. After 30 days of exposure the test specimens were removed, cleaned, reweighed and visually evaluated.

Tensile test specimens were extracted from DMD and FSP 4047 aluminum samples and were tested in-house. The specimen had a gage length of 15.2mm, a gage width of 6.5mm and a gage thickness of 3.3mm. It also had a shoulder region of radius 6.35mm and a grip section of length 15.5mm on both sides. For the FSP sample the longitudinal axis of the tensile test specimen was perpendicular to the FSP pass direction. Room temperature tensile tests were performed at a constant crosshead speed of 0.5mm/min.

8.3 Results and Discussion

Fig. 8.1 shows the microstructure of as-deposited DMD 4047 alloy at three different magnifications. The white phases are the silicon particles and the dark phase is the aluminum matrix. The arc-shaped features are the boundaries of laser tracks which are characterized by low density of silicon particles. Columnar dendrites which are characteristic of high-rate solidification microstructure are also visible.

Fig. 8.2 shows a macro-image of the FSP nugget processed at 2000rpm and 127mm/min. It also shows the transition of microstructure from FSP nugget to the thermo-mechanically affected zone (TMAZ) and finally to the base metal. The as-deposited DMD has alternate silicon-rich and silicon-depleted regions which gives it the characteristic contrast. FSP largely homogenizes the microstructure thus making the nugget almost featureless as shown in the top part of Fig. 8.3. Pores and voids are visible in both DMD and FSP. FSP nugget microstructure is fairly uniform in distribution of silicon particles. However certain regions show bimodal distribution of silicon particles (Fig. 8.3).

FSP of DMD-4047 was also carried out for various other rpm and feed-rate combinations. The results of these runs are similar to that obtained before. But the size and distribution of silicon particles varies as a function of rpm and feed-rate. Figure 8.4 illustrates this variation along with the as-deposited microstructure. As the rpm increases and feed-rate decreases, the size of silicon particles as well as the inter-particle spacing increases. This can be attributed to higher temperature in the nugget zone due to higher rpm and lower feed-rate. High temperature leads to agglomeration of silicon particles.

Fig. 8.5 shows overlapping FSP passes at 1500 rpm and 127 mm/min. The overlap is 16.6% of the pin diameter between successive passes. A onion ring structure is observed within the nugget. The dark and white bands within the onion ring are due to difference in density and size of silicon particles also shown in Fig. 8.5.

The hardness profile of the specimens stir-processed under various conditions was studied. Figure 8.6 shows the overall hardness profile under various conditions. Note that as-deposited DMD is the hardest (~72 HV). As the rotation rate increases and feed-rate decreases the hardness decreases albeit slightly. Silicon particle spacing controls the hardness via the Orowan looping mechanism. The larger the spacing between particles, the softer the material.

Table 8.2 shows the mechanical property data of 4047 aluminum under various processing conditions. The values show a decrease in yield strength and UTS for FSP-4047 aluminum in comparison to DMD-4047 aluminum. This is because the silicon particle spacing increases in FSP-4047 aluminum, thus softening the material (Orowan effect).

Table 8.3 shows the corrosion rate of DMD and FSP 4047 in artificial seawater. Corrosion behavior of DMD and FSP 4047 aluminum are similar.

8.4 Summary and Conclusions

In this chapter FSP of DMD 4047 aluminum was carried out. As-deposited DMD-4047 aluminum has alternate regions with high and low density of fine silicon particles which give rise to dendritic morphology. FSP homogenizes the silicon distribution within the

nugget. The silicon particle size and spacing are directly related to the rpm and feed-rate of FSP. Higher rpm and lower feed-rate lead to coarser particles with higher inter-particle spacing. This lowers the hardness of FSP alloy over DMD. As-deposited DMD-4047 aluminum has higher yield strength and lower ductility than FSP-4047 aluminum. Corrosion behavior of DMD-4047 and FSP-4047 aluminum alloy is similar.

8.5 References

[1] G. Mathers, *The welding of aluminum and its alloys*, (2002) 41

[2] S.R. Sharma, Z.Y. Ma, R.S. Mishra, *Scripta Mater.* 51 (2004) 237

Si	Fe	O	Cu	Mn	Mg	Zn	Al
11.3	0.18	0.6-0.7	0.03	<0.01	<0.01	<0.01	Bal

Table 8.1 Composition in wt% of 4047 aluminum alloy.

	0.2 % Yield Strength (MPa)	UTS (MPa)	Ductility
DMD 4047 Al	146	212	2.2%
FSP 4047 Al	90	207	19%

Table 8.2 Mechanical property data of 4047 aluminum.

Sample	Corrosion Rate (μm/yr)
DMD 4047 aluminum	7.1
FSP 4047 aluminum	7.1

Table 8.3 Corrosion rates of 4047 aluminum under various processing conditions.

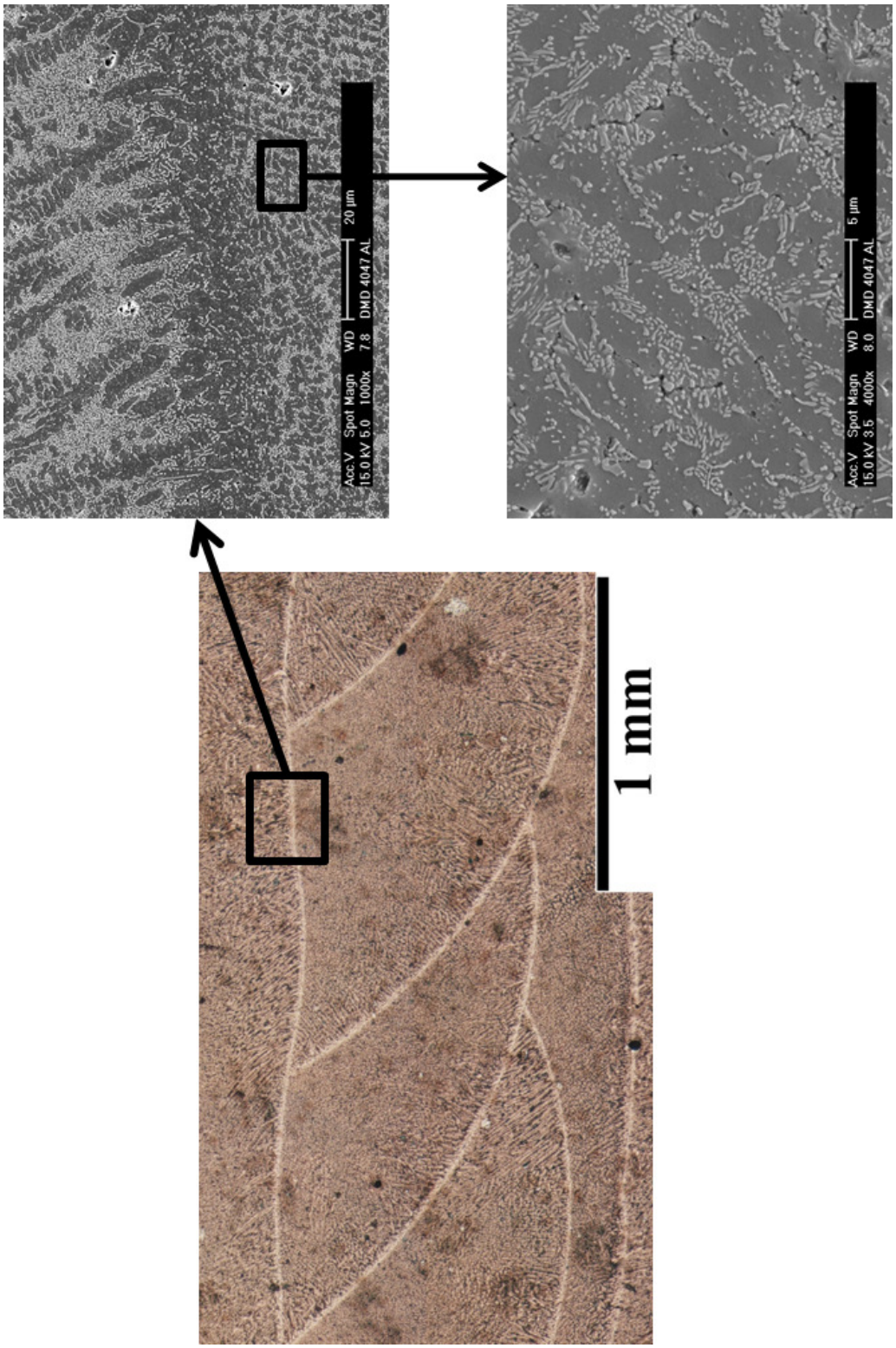

Fig. 8.1 As-deposited DMD 4047 aluminum showing silicon particles dispersed in aluminum.

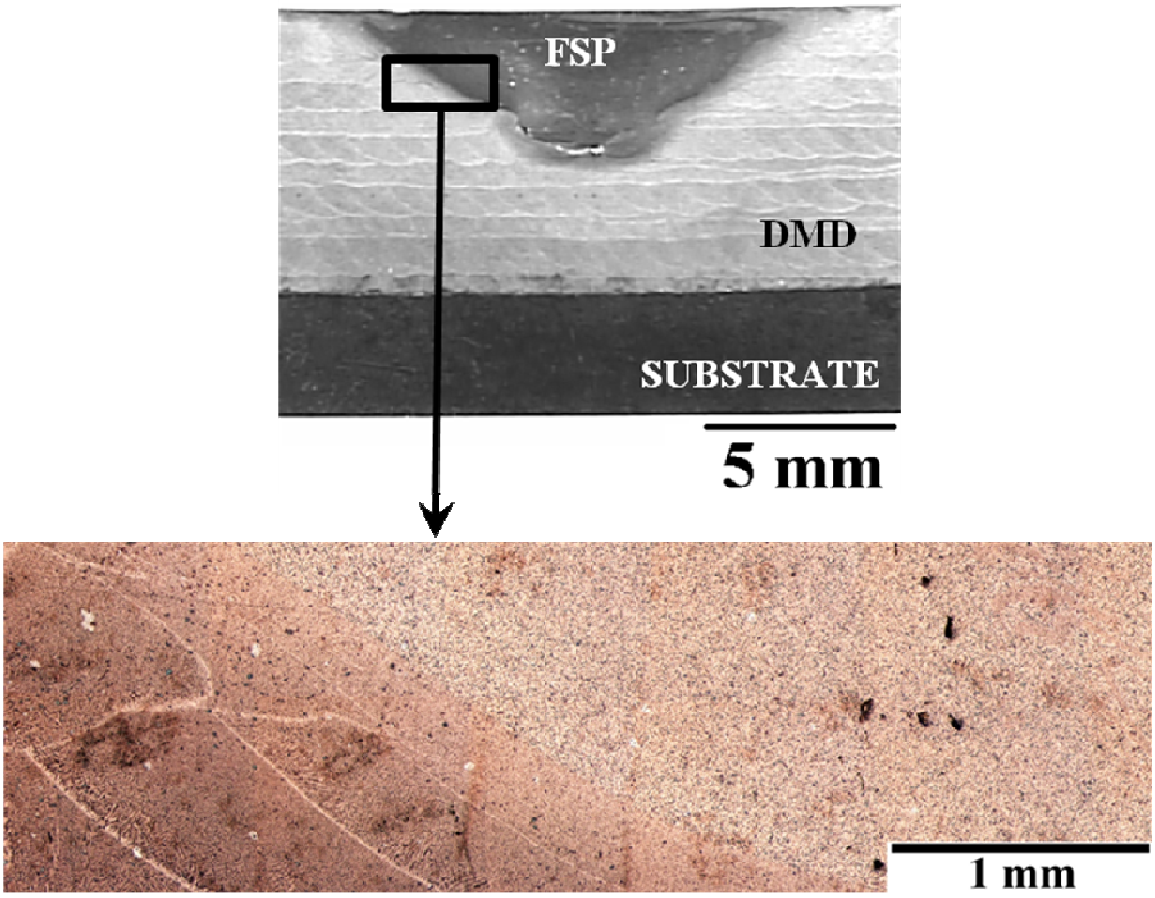

Fig. 8.2 Microstructure of DMD-4047 aluminum nugget and TMAZ. Processing condition was 2000rpm, 127mm/min.

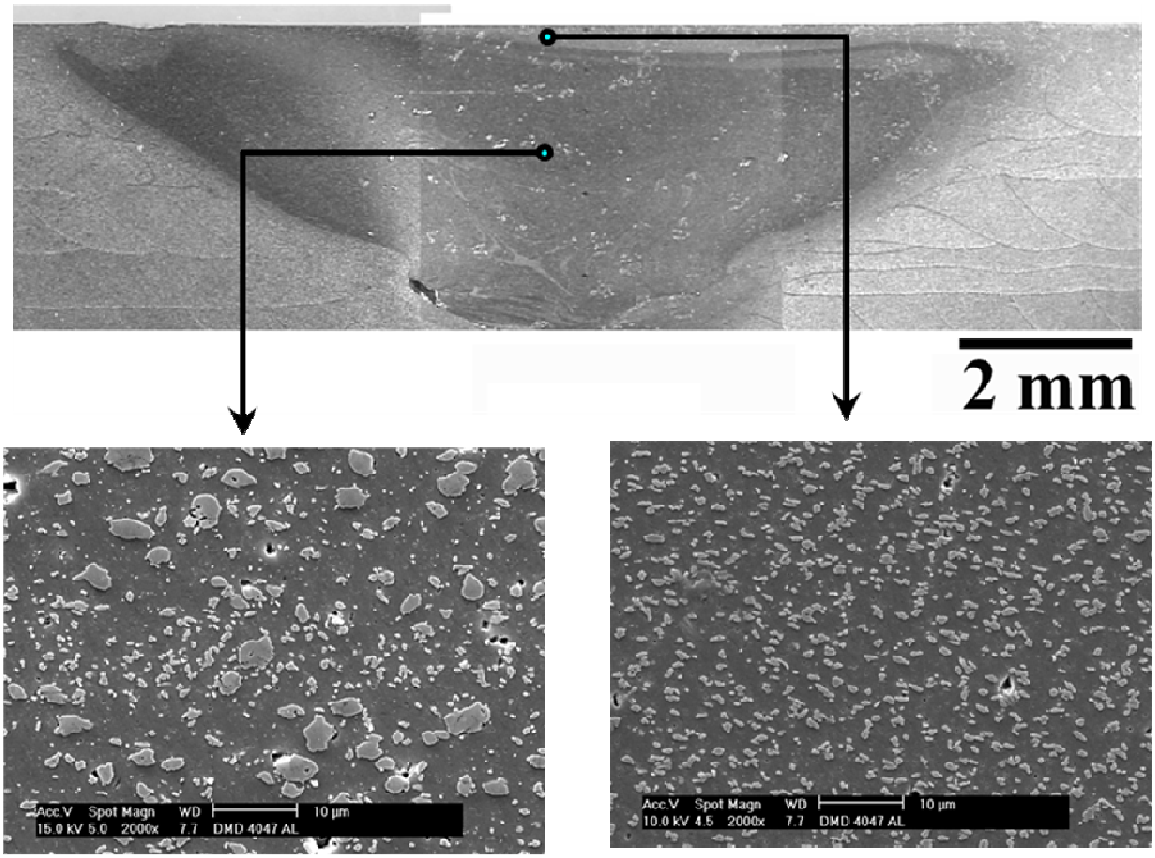

Fig. 8.3 Microstructure of FSP nugget showing silicon particles in aluminum matrix.

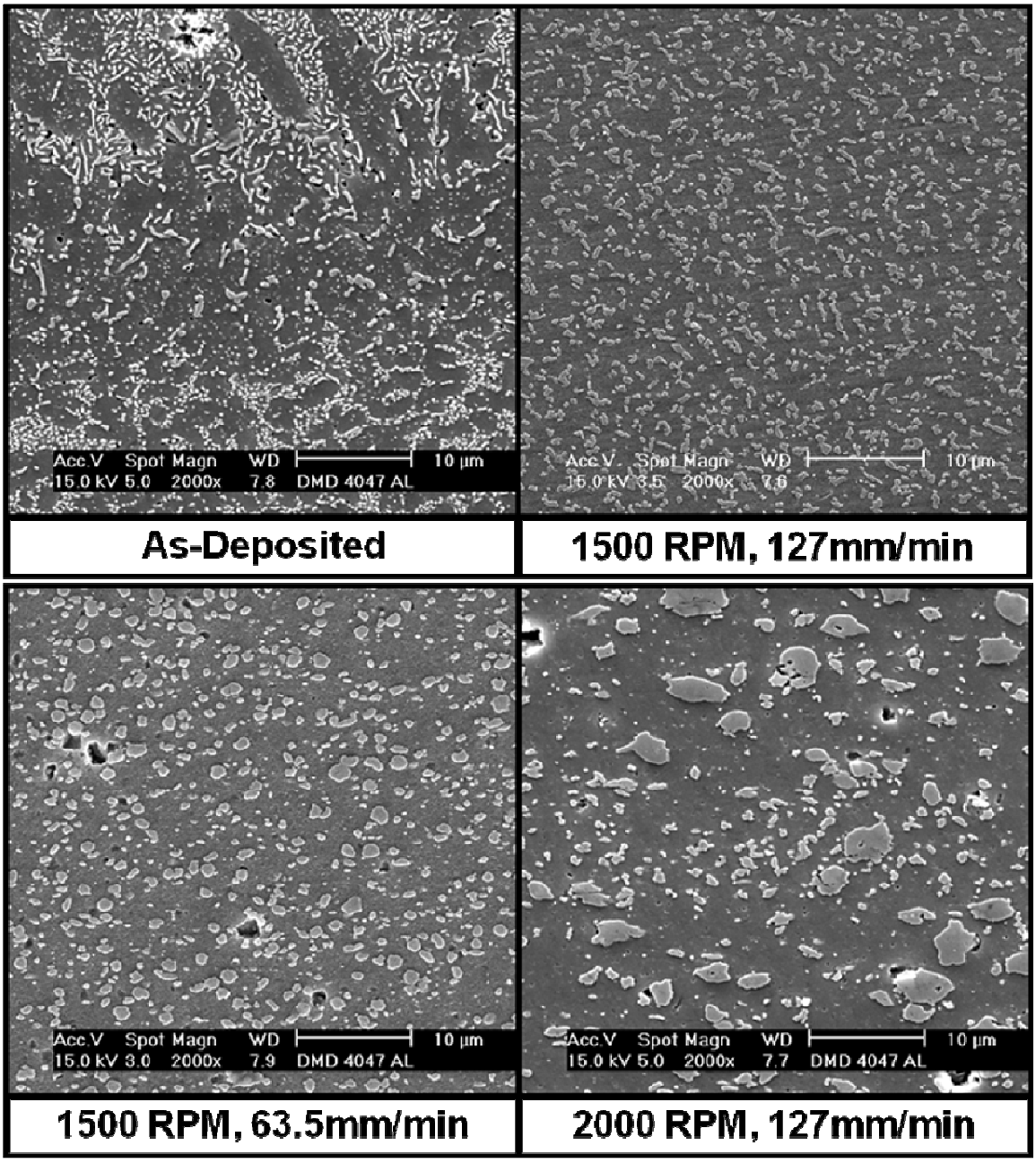

Fig. 8.4 Microstructure of FSP nugget as a function of rpm and feed-rate.

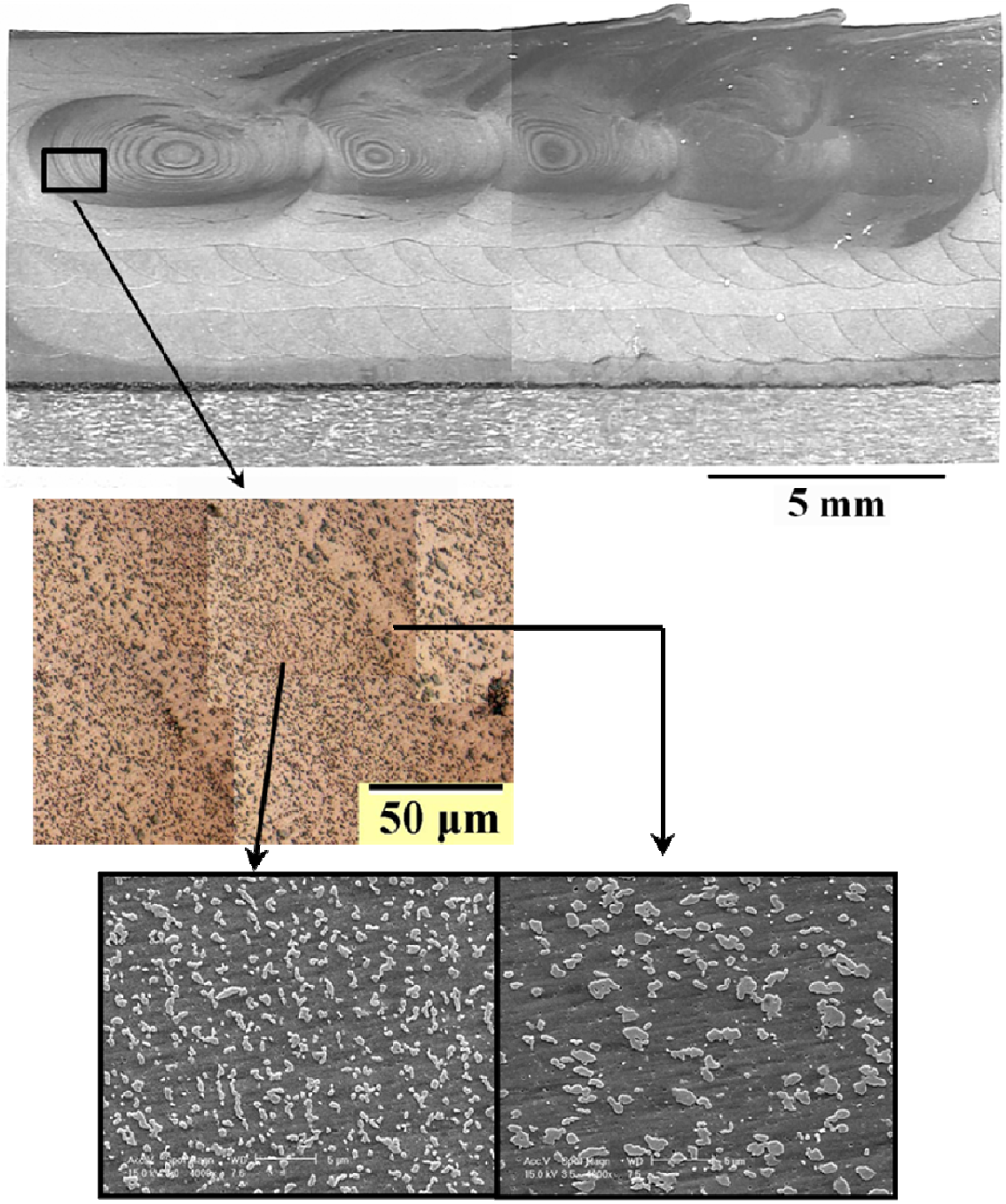

Fig. 8.5 Microstructure of overlapping FSP passes showing onion ring structure.

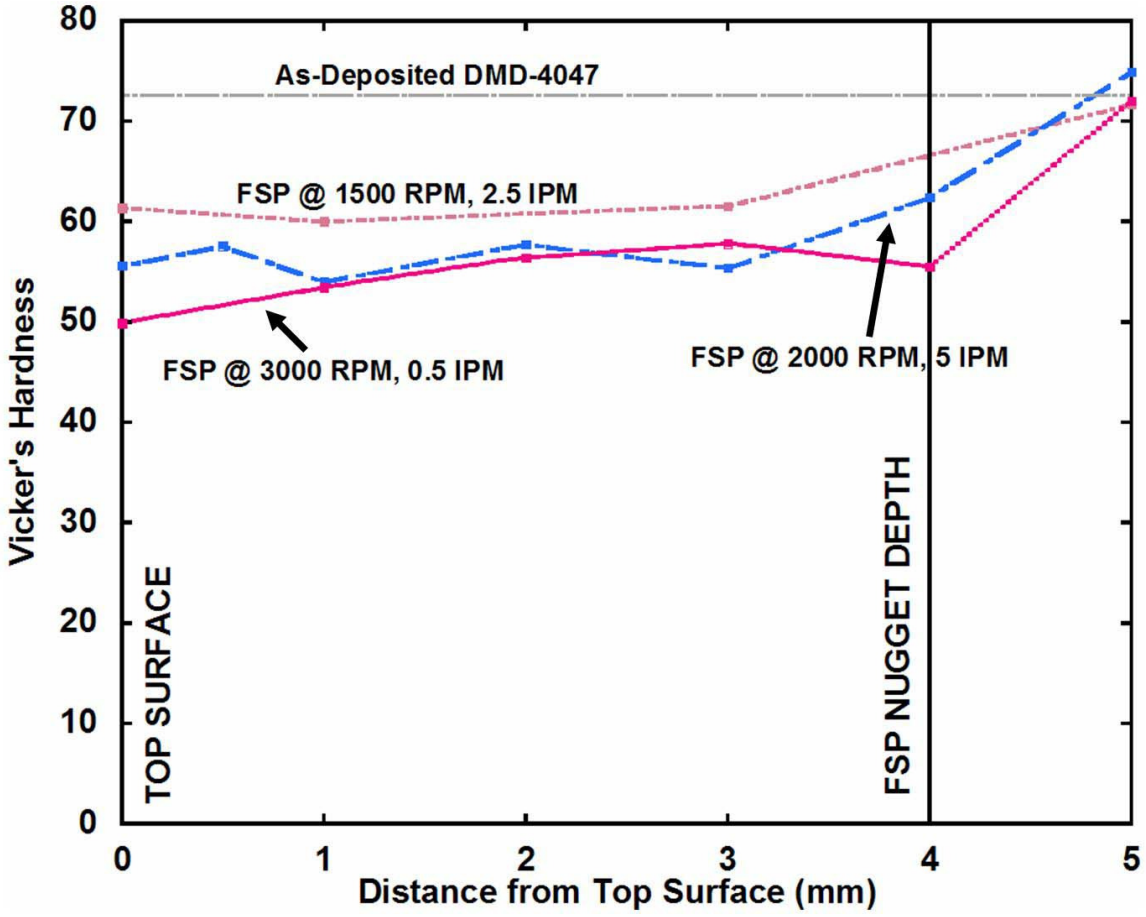

Fig. 8.6 Hardness profile for different FSP rpm and feed-rates.

Chapter 9

Summary

In this thesis, the strain and strain-rate during Friction Stir Processing (FSP) of an aluminum alloy were estimated theoretically and experimentally. The deformation field around the FSP pin was observed by inserting a ductile foil in the path of the pin. Logarithmic thickness strain was measured by observing the change in thickness of the foil. The maximum thickness strain measured was ≈ 4.6. A numerical simulation was carried out under the assumption of a uniform tangential material velocity along the contact interface between the pin and workpiece. Various values of velocity ratio – which is the ratio of material velocity at the interface and pin surface velocity – were assigned to numerically calculate the deformed foil geometry. It was found that a velocity ratio of 0.1 best characterized the experimentally observed deformed foil geometry. Under this contact condition the maximum shear strain rate numerically estimated was ~ $87sec^{-1}$.

A fundamentally different approach towards FSP tool design and indeed a fundamentally different approach towards FSP itself were presented. By using multiple closely-spaced pins rotating in the same direction, the numerically calculated strain-rate and temperature in the stir zone increase during the welding process. The resistance force on the pins reduces and along with it the tool-wear. A prototype two-pin welding tool was designed,

fabricated and tested using a milling machine and a separate power supply in the form of a Bosch grinder motor. Sufficient torque couldn't be obtained using these motors. A new design involving a brushless torque motor is proposed to lend functionality to the multi-pin apparatus.

One of the main objectives of this thesis is to show that FSP can be used to repair and restore marine components which suffer degradation due to corrosion. Traditionally repair work is performed using laser assisted Direct Metal Deposition (DMD). It was observed that DMD followed by FSP is an efficient way of performing excellent repair. The materials studied in this thesis were 4340 steel, copper-nickel 70/30, 7475 aluminum and 4047 aluminum. As-deposited DMD 4340 steel had martesite-bainite microstructure, which was tempered by flame treatment followed by FSP. Upon flame treatment a gradient in microstructure developed within the DMD deposit with the top layer consisting of bainite, ferrite and ferrite-carbide aggregate and the layers below it consisting of martensite-bainite albeit with varying degrees of tempering. After FSP, the top layer of the process zone reverted back to the martensite microstructure. FSP improved the ductility of DMD 4340 steel at the expense of reduced strength.

As-deposited DMD Cu-Ni 70/30 had dendritic solidification microstructure with the length of the dendrites between 30-60μm and the width between 4-15μm. After FSP, extensive recrystallization in the nugget region led to finer and equiaxed grains of size 1-2.5μm. Porosity was observed in the as-deposited and FSP Cu-Ni 70/30 alloy. In the as-deposited DMD layer adjacent to the substrate, porosity was ≈ 3.3%, in the next layer the porosity was ≈ 1.3%. Porosity in the FSP nugget was significantly reduced to ≈ 0.35%. Energy dispersive spectroscopy suggested a higher copper concentration along as-

deposited DMD dendrite boundaries. FSP homogenized the elemental composition across grain boundaries and grain interiors. Tensile and corrosion tests were carried out on DMD and FSP Cu-Ni 70/30 alloy. FSP Cu-Ni 70/30 had higher yield-strength, lower ductility and higher corrosion rate than DMD Cu-Ni 70/30.

The as-received 7475 aluminum had a rolled and elongated grain structure. After FSP the grain structure became equiaxed and recrystallized. FSP of 7475 aluminum led to a reduction in strength, increase in ductility and lowering of corrosion rate. The feasibility of 7475 aluminum plug-based repair of a torpedo fuel tank was demonstrated. Simulated repair of the fuel tank for large corrosion hole was successfully carried out using a plug held by screw-thread. Plug-based repair without using the ramp piece was attempted with two different techniques. In the repair technique by stacking thin discs, the interface between discs and the hole became hot and severely deformed thus creating conditions for an effective repair.

As-deposited DMD-4047 aluminum had alternate regions with high and low density of fine silicon particles which gave rise to the dendritic morphology. FSP homogenized the silicon distribution within the nugget. The silicon particle size and spacing was directly related to the rpm and feed-rate of FSP. Higher rpm and lower feed-rate led to coarser particles with higher inter-particle spacing. This lowered the hardness of FSP alloy over DMD. As-deposited DMD-4047 aluminum had higher yield strength and lower ductility than FSP-4047 aluminum. Corrosion behavior of DMD-4047 and FSP-4047 aluminum was found to be similar.